Automatic Cell Viability Determination In Bright-Field Microscope Images

Masters Thesis in Computer Science

submitted
by

Elmarie van Heerden

born 20.02.1987 in Pretoria

Written at

Lehrstuhl für Mustererkennung (Informatik 5)
Department Informatik
Friedrich-Alexander-Universität Erlangen-Nürnberg.

Advisor: M. Sc. Firas Mualla, Dipl.-Inf. Simon Schöll , Prof. Dr.-Ing. Joachim Hornegger

Started: 1.03.2013

Finished: 2.09.2013

Ich versichere, dass ich die Arbeit ohne fremde Hilfe und ohne Benutzung anderer als der angegebenen Quellen angefertigt habe und dass die Arbeit in gleicher oder ähnlicher Form noch keiner anderen Prüfungsbehörde vorgelegen hat und von dieser als Teil einer Prüfungsleistung angenommen wurde. Alle Ausführungen, die wörtlich oder sinngemäß übernommen wurden, sind als solche gekennzeichnet.

Die Richtlinien des Lehrstuhls für Studien- und Diplomarbeiten habe ich gelesen und anerkannt, insbesondere die Regelung des Nutzungsrechts.

Erlangen, den 28. August 2013

Abstract

Quantification of non-viable cells in bright-field microscope images allows for an *in vitro* assessment of the viability of cultured cells. The identification and quantification of non-viable cells in a cell culture is conventionally achieved with viability stains. A disadvantage of viability stains is that they might be invasive and even toxic to a cell culture. For this purpose, a non-invasive keypoint-based cell viability determination method without the use of viability stains, has been developed. This method formulates unstained non-viable cell detection as a supervised, binary pattern recognition problem and presents a set of features that are suitable for distinguishing between unstained viable and non-viable cells in bright-field micrographs. Experimental results for a representative sample of micrographs are compared with the ground truth non-viable cell count obtained from fluorescent micrographs. Despite the low contrast and high variability in appearance of cells in bright-field images, the method yield a classification rate in excess of 88% for non-viable versus viable-suspended cells and of more than 65% for non-viable versus viable-adherent cells . Thus, the developed method has been proven to be a feasible alternative for cell viability determination in bright-field micrographs.

Contents

Chapter 1

Introduction

1.1 Preamble

Cell culture studies have been instrumental in the advances made in the fields of biotechnology, biology, medicine, tissue engineering and stem cell research. Studying cell cultures has the advantage that it decreases the reliance on animals for experimental purposes and in addition offers the possibility to study subtle mechanisms *in vitro*, which is not always possible *in vivo* [vO94]). Possibilities exist to improve the methodology of cell culture studies. In this study, such possibilities will be explored.

1.2 Problem statement

Cell viability and the rate of cell death are important parameters in many experiments involving cell cultures. The physiological and morphological state of a cell are directly related to its viability.

Although an experienced observer may sometimes recognise the subtle differences between viable and non-viable cells, viability stains are commonly used for the reliable determination of viability [Cod01].

A disadvantage of viability stains is that the cells are exposed to chemical agents, which might affect the natural life cycle of the cells being studied and ultimately compromise the validity of the experimental results [Lup08].

Cell death kinetics can be quantified by counting the number of non-viable cells on a culture dish at different intervals of the cell culture's evolution. This procedure is laborious and demands time in order to obtain reliable statistics from counting a large number of cells manually at regular

intervals.

The identification and localisation of non-viable cells in a cell culture is conventionally achieved with the use of fluorescent probes. A drawback of fluorescent probes is that they might be invasive and even toxic to the cell culture not to mention the possibility of causing cell culture contamination [Fog71]. Furthermore, considering the fact that the number of fluorescent channels is limited, it is highly desirable to accomplish non-viable cell recognition with transmitted light microscopy, for example bright-field illumination. Freeing up the fluorescence channels allows for other cellular and sub-cellular analysis [Wei08].

In summary, the problem identified in this study is that the current methodologies used for biological cell culture studies are not conductive towards the expected benefits that may be derived from them.

1.3 Objective of the study

Manual counting, viability stains, estimates of cell statistics, limited fluorescent channels, and cell culture contamination all prompt the development of non-invasive, high throughput robotic systems that are able to automatically recognise and track viable cells in culture [Lon06]. This may be done through effective algorithms.

The challenge of developing effective algorithms lies in finding mathematical discernible features that are able to recognise the subtle differences in appearance that distinguish viable from non-viable cells in bright-field and phase contrast micrographs. Selected apt features may lead to an increase in system performance, because feature selection allows for the exclusion of redundant or misleading information that may be contained in raw data.

The main objective of this study is therefore to develop efficient and effective algorithms to replace outdated ineffective manual and stained based cell culture study methodology. More detailed objectives of this study are also given in the latter part of the section on literature review.

1.4 Research methodology

The research methodology followed in this thesis includes a literature review of studies already undertaken to address cell viability determination without the aid of viability assays, the logical inductive design of a mathematical pipeline to solve viability determination of unstained cells in bright-field micrographs, and the empirical testing of the effectiveness of the results produced by the pipeline by means of a comparison with ground truth cell viability statistics.

1.5 Outline of the study

The idea of the automatic detection of unstained cells in bright-field images has previously been investigated, resulting in a number of techniques designed for that purpose [Mal03][Lon06] [Wei07][Wei08]. These techniques are investigated in chapter two of this thesis. In chapter three, the scope and context of the study is delineated.

Chapter four is devoted to the materials and experimental conditions required to prepare the cell cultures for this study, the types of micrographs acquired, and to the technical requirements of the hardware and software needed for implementing the cell viability determination pipeline. The overall framework for automatic cell viability determination is outlined in chapter five.

The features considered to discern between viable and non-viable cells are introduced in chapter six. The underlying structures in a multidimensional feature space is difficult to interpret and even more so to visualise. Dimension reduction algorithms allows for multidimensional data structures to be more efficiently described by searching for linear or non-linear mappings that contain the most relevant information on underlying structures. Therefore, in chapter seven, the use of linear and non-linear unsupervised dimensionality reduction methods, which are used to investigate the underlying structures of the features, are described.

In chapter eight, various classifiers are proposed for the automatic classification of unstained cells. These classifiers are compared with one another based on their mathematical foundation.

In chapter nine, the newly designed cell viability classification methodology is evaluated. Finally, the conclusions and possible extended research possibilities are given in chapter ten.

1.6 Scope and limitations of the study

This proof-of-concept study focuses on automatic cell viability determination in bright-field and phase contrast micrographs as an alternative to viability stains. The study is limited to animal cells, more specifically Chinese hamster ovary (CHO) cells. Cell death is induced by a single toxin to facilitate the study of the differences between viable and non-viable cells.

Bright-field and phase contrast micrographs are taken at a single instance in the cell culture evolution. Hence, the study does not take into account that the physical and metabolic activity of cells change over the course of the cell culture evolution.

The study neither addresses the effect which different toxins might have on cell viability, nor does it investigate the characteristics associated with the different mechanisms of cell death.

Chapter 2

Related Work

2.1 Literature review

Producing automated systems based on optical microscopy of cell cultures, requires the replacement of the human observer with effective algorithms. Such algorithms should be able to identify and localise individual cells and perform additional studies on these cells in relation to biochemical parameters [Hua03].

Limited depth of field, uneven illumination, optical aberrations, presence of ”trash” (electronic noise and debris in the culture medium) and high variability in the cells' appearance over the cell's cycle are a few of the aspects that make the automated identification of unstained viable cells in bright-field images a challenging task [Lup08]. Even more difficult is the recognition of the subtle differences in appearance that distinguish unstained viable from non-viable cells in bright-field images [Lon06].

Existing approaches to the automatic analysis of cell viability without staining, are either dominated by methods that use information from light microscopy other than bright-field or which use fixed sized pixel patch extraction to generate feature vectors that are used to represent cells. Furthermore, these methods have formulated the determination of unstained cell viability as a supervised pattern recognition problem by accommodating the variations in illumination, cell size and morphology through training. Among the machine learning techniques, discriminant analysis [Mal03] and support vector machine (SVM) [Lon06, Wei07, Wei08] classifiers have been used to accomplish, with reasonable accuracy, the automated identification of unstained viable and non-viable cells in light microscopy images captured, using low magnification (10x) lenses. The related methods are summarised in Table2.1.

Year	Publication	Light Microscopy	Features	Classifier
2002	Malpica et al.	Phase contrast	Texture	Discriminant analysis
2006	Long et al.	Bright-field	Pixel patch	SVM with an improved training procedure
2007	Wei et al.	Dark-field	Pixel patch	SVM
2008	Wei et al.	Dark-field	Wavelets	SVM

Table 2.1: Summary of related work

Malpica et al. [Mal03] were the first to perform automatic quantification of viability in unstained cell cultures by extracting texture features from phase contrast images and using discriminant analysis for classification. Based on a texture analysis, the phase contrast images were classified by means of a segmentation algorithm into three regions, namely viable cells, non-viable cells and background. Three discriminant functions, built from parameters derived from the histogram and the co-occurrence matrix of the regions of interest, were used for classification. The authors observed that initially the growing cell colonies yield high contrast images where the edges of the individual cell are rather conspicuous. In the later stages of the cell culture's life cycle, cell death leads to condensation and fragmentation of cell bodies, which produces regions populated with unstructured smaller objects as non-viable cells loose their shape and size. Their method was compared to the quantitative results obtained by an expert observer and achieved a relative mean difference of 18.06% and a standard deviation of 19.11%.

Long et al. [Lon06] achieved automatic detection of unstained viable cells in bright-field images by using a SVM with an improved training procedure. The feature vectors used to represent the cells were derived from fixed sized pixel patches that were extracted from the bright-field images. The iterative training procedure selected the most representative of the aforementioned feature vectors for calculating the decision boundary of the SVM. Thus, the focus of the Long et al. research was not to investigate features that support the best classification of cell viability, but rather that the classifier improvement focused on the imbalance dataset.

Fermentation industries have a great need for the on-line monitoring of important parameters describing cell growth such as cell density and viability during fermentation processes. For this purpose, Wei et al. 2007 [Wei07] developed an *in situ* probe which utilises a dark-field illumination unit to obtain high contrast images of yeast cells with an integrated CCD camera. Two SVM classifiers were trained, one to separate the cells from the background, and one to distinguish viable from non-viable cells. Pixel patches around the cells were taken as feature vectors to represent the cells and to train the classifiers. The evaluation of the *in situ* experiments

showed strong correlation between results obtained by the probe and those by widely accepted standard methods [Wei07]. Thus, the system proved feasible for the on-line monitoring of both cell density and viability, with high accuracy and stability.

Wei et al. 2008 [Wei08], developed a machine vision system for the automated non-invasive assessment of cell viability from dark-field microscope images . The system performs wavelet decomposition on the dark-field microscope cell images and then computes the energy and entropy for each wavelet sub-image as features. They found that wavelet features are very successful in describing the discriminative properties of viable and non-viable cells. According to their analysis, viable cells exhibit morphologically more detail and are intra-cellularly more organised than non-viable cells, which display more homogeneous and diffuse gray values throughout the cells. Furthermore, viable cells have a higher mean energy value which means that on average viable cells look brighter and contain more details than dead ones. It is also clear from the study that when considering any entropy feature, viable cells have a lower mean value which implies that viable cells contain more inhomogeneous fine structures than dead cells. The authors conclude that the correlation between the results from their machine vision system and the stained ground truth images became stronger if wavelet features are utilised.

Long et al. [Lon06] and Wei et al. 2007 [Wei07] did not actually investigate the various types of features to distinguish between viable and non-viable cells but they rather extracted fixed sized pixel patches from the images and used these as feature vectors to train SVMs. On the other hand, Malpica et al. [Mal03] and Wei et al. [Wei08] addressed the question of which features are best able to distinguish between viable and non-viable cells. However, the drawbacks of these methods are the fixed sized masks used to extract features and the lack of a universal feature subset that is able to distinguish between unstained viable and non-viable cells regardless of the light microscopy technique, type of cells or size of cells. The latter is not as a result of their methods but of the inherent difficulty of the problem at hand. A further disadvantage of the aforementioned methods is that their systems need to be retrained each time it is exposed to new data.

Resulting from the study of work already done on the automatic detection and classification of unstained viable cells, the aim of this thesis is to improve on the methods described, by replacing the fixed sized pixel patches with dynamically changing pixel patches that are able to adjust their size. The second goal is to introduce and evaluate additional features which are able to discern between unstained viable and non-viable cells in bright-field microscope images. Besides exploiting image intensity information, the incorporation of colour information into the system to discern between viable and non-viable cells is also investigated.

2.2 Patent research

An extensive patent search on the topic of unstained cell viability determination from microscope images produced no matching results. However, three patents related to viable cell counting were found. One of the patents is a method and the other two are devices developed for counting viable cells in cultivation.

The first patent pertains to a method developed by Long et al. [Lon10] who produced a journal publication in which this method was used for multiclass cell detection in composite images without staining. The method includes deriving vectors for objects belonging to one of three or more classes and training binary classifiers with a CISS algorithm which uses an ECOC technique. The methods calculates the probability that a vector associated with an object belongs to a particular class, using an ECOC probability estimation technique. The method additionally employs a non-linear dimensionality reduction technique, Kernel PCA, to extract features from the multi-contrast composite images.

The second patent, invented by Straus, is for a device which enables the rapid counting of living cells by detecting microscopic colonies derived from *in situ* cell division using large area imaging. This invention addresses the problem of the long time that is needed in conventional tests to quantify microbial enumeration. The invention is able to detect cellular micro-colonies without the use of labelling probes. The fact that the invention is non-invasive allows for the generation of pure cultures which can be used for microbial identification and determination of antimicrobial resistance.

The third patent, invented by Haruyuki and Kouichi, is for a system that is able to quickly calculate the number of viable cells in a culture by taking a photograph of a viable cell specimen through an inverted phase contrast microscope with a TV camera. Whereafter, the image signal is scanned and a viable cell count is calculated by means of an image analyser.

The patent documents with detailed abstracts can be found in appendix A.

Chapter 3

The Biological Cell

3.1 Types of biological cells

Life exhibits varying degrees of organisation. Atoms are organised into molecules, molecules into cells and cells into organisms. According to the cell theory, biological cells are the structural units of life and the functioning of a multicellular organism is a consequence of the type of cells of which it is made up. Biological cells may be classified as either being prokaryotic or eukaryotic (see figure 3.1 for detail). All biological cells have certain structures and elements in common, such as a cell membrane, cytoplasm, ribosomes and nucleic acids, the so called deoxyribonucleic acid (DNA) and ribonucleic acid (RNA) which contains the organism's genetic code.

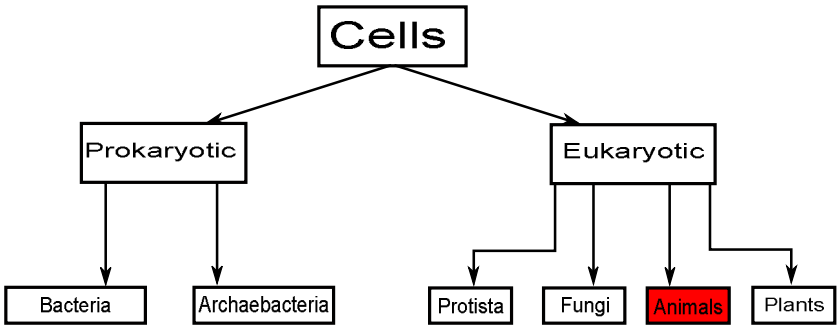

Figure 3.1: The phylogenetic tree of life showing that biological cells are divided into two fundamental classes: prokaryotic and eukaryotic.

3.2 Prokaryotic cells

Prokaryotic cells neither have a membrane-bound nucleus nor any membrane bound organelles. Hence, these cells' DNA is not confined to the nucleus but distributed throughout the cytoplasm of the cell (Fig. 3.2). Prokaryotic cellular life is broken up into two kingdoms: bacteria and archaebacteria (Fig. 3.1). Bacteria exist as single prokaryotic cells. Archaebacteria are multiple prokaryotic cell organisms known as ancient life forms which live in extreme environments.

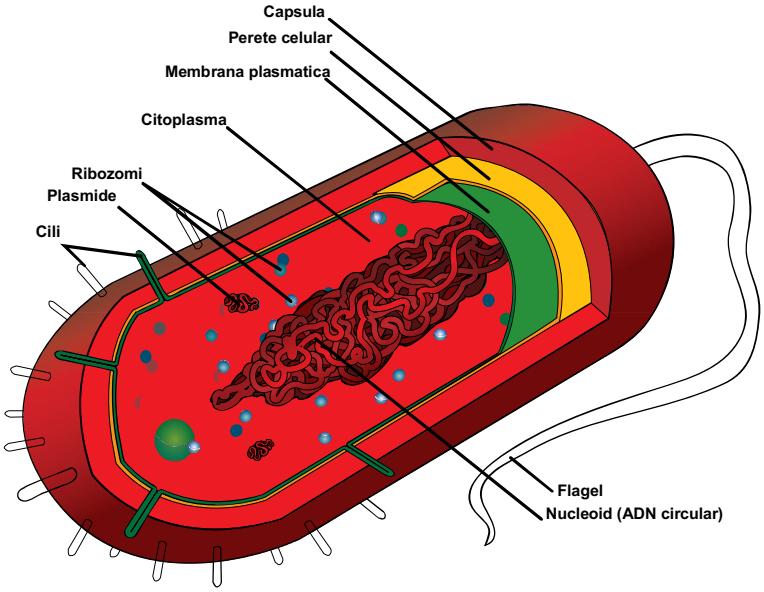

Figure 3.2: Structure of a prokaryotic cell [Pro].

3.3 Eukaryotic cells

3.3.1 Introduction

Eukaryotic cells are characterised by membrane-bound nuclei, which contains the DNA, and multiple internal organelles that carry out specific tasks (Fig. 3.3). Eukaryotic cellular life is broken up into four kingdoms: protista and fungi (the single cell organisms) and plants and animals (the multiple cell organisms) (Fig. 3.1). Eukaryotic cells from the animal kingdom are used in this thesis.

Cells are made-up of many specialised sub-structures as is evident in Figure 3.3. However, in this thesis only three of these sub-structures and their functions are of importance, namely the nucleus, the mitochondria and the plasma membrane.

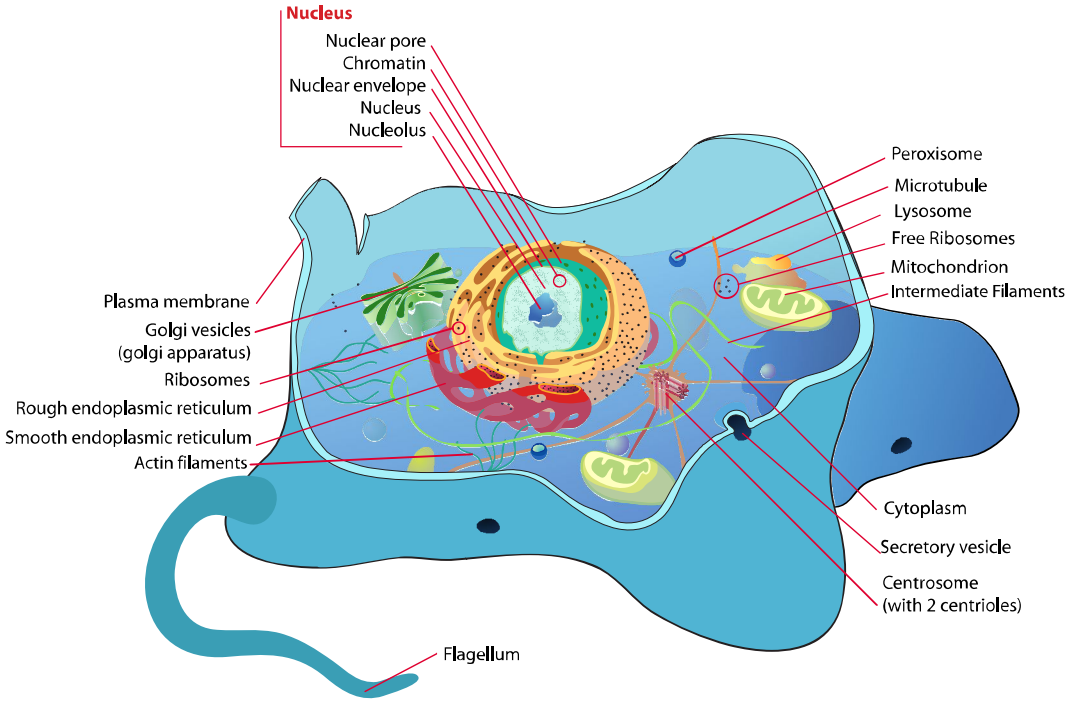

Figure 3.3: Structure of an eukaryotic cell [Euk].

The nucleus contains genes, which are responsible for cell differentiation. The mitochondria regulate cellular activity, and the plasma membrane consists of a fluid lipid bilayer which holds together all organelles internal to the cell [Hic95].

3.3.2 The nucleus

The nucleus of an eukaryotic cell, shown in Figure 3.3, is the location of most of the nucleic acids in a cell, such as DNA and RNA.

DNA is the physical carrier of inheritance and is restricted to the nucleus. The DNA contains the information necessary for constructing the cell and directing the multitude of tasks performed by the cell during the cell's life cycle.

RNA is formed in the nucleus using the DNA base sequence as a template. RNA moves outwards into the cytoplasm where it assists in the production of proteins.

The nucleus is enclosed by a nuclear envelope, which regulates the passage of macromolecules like proteins and RNA. Macromolecules are inter alia responsible for the information flow in the cell.

Histones are a family of basic proteins most commonly found in association with the DNA in the nucleus of eukaryotes. These proteins help to condense the DNA into a smaller volume (see

Fig. 3.4). Without histones, the unwound DNA in chromosomes would be very long.

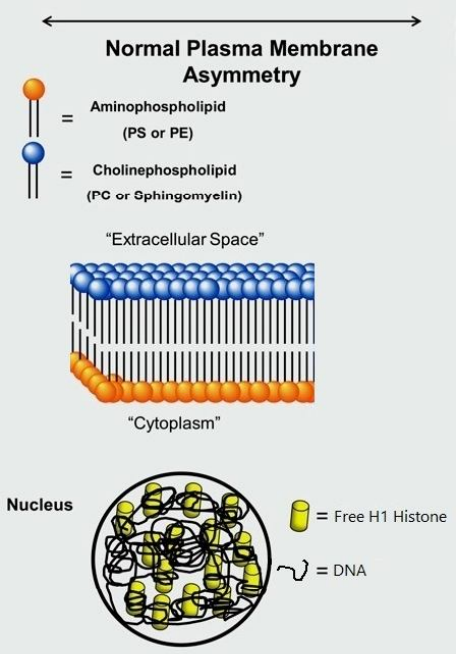

Figure 3.4: Typical nucleus and plasma membrane of a viable cell [Tai08].

3.3.3 The mitochondria

Cytoplasm refers to the colloidal fluid portion of the cell in which numerous organelles of the eukaryotic cell are suspended. Arguably, the most important organelles found in the cytoplasm are the mitochondria. Mitochondria are know as the power generators of the cell; they are responsible for the production of adenosine triphosphate (ATP), the major source of cellular energy. Other important roles of mitochondria include cell signalling, cellular differentiation as well as the control of the cell life cycle and cell growth.

In a healthy mitochondria both the outer mitochondrial membrane and inner mitochondrial membrane (IMM) are intact. The mitochondrial permeability transition pore (MPTP), in an open state, transports ATP. Anti-apoptotic proteins from the B-cell lymphoma protein 2 (Bcl-2) bind to Bc L-2-associated X protein (Bax), avoiding its oligomerisation and thus cell death (see Fig. 3.5).

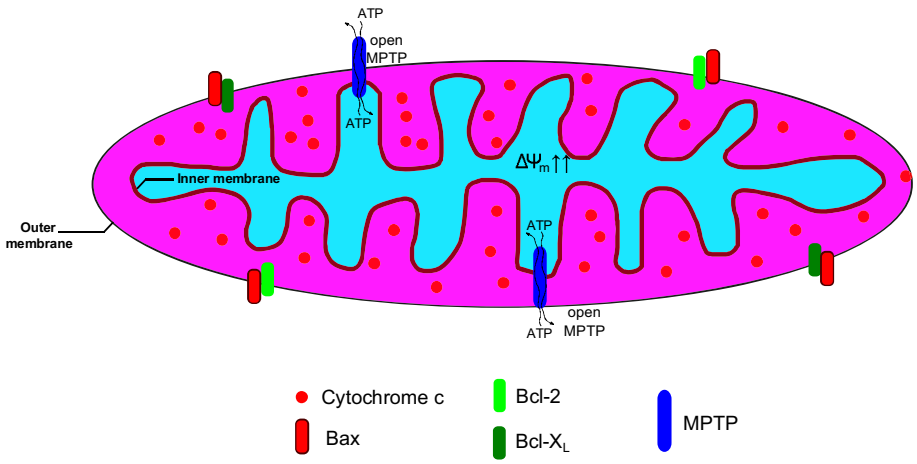

Figure 3.5: Structure of a mitochondria in a viable cell.

3.3.4 The plasma membrane

The organelles internal to cells are ring fenced by a thin membrane referred to as the plasma membrane or cell membrane. The plasma membrane, consists primarily of phospholipids and proteins; functions as a semi-permeable barrier which allows essential nutrients as well as cellular waste to pass through, while fencing-in the majority of internally produced chemicals. The proteins within the cell membrane function as gateways that will allow certain molecules to cross into and out of the cell by moving through channels within the protein membrane molecules. Cholesterol is another important element of cell membranes and aids in the flexibility of the cell membrane.

In healthy cells, phospholipids are asymmetrically distributed. The anionic phospholipid, phosphatidylserine (PS),is normally confined to the cytoplasmic face of the plasma membrane and the cationic phospholipid, phosphatidylcholine (PC), to the external surface of the plasma membrane (see Fig. 3.4) [Tai08].

3.3.5 The effect of cytotoxic agents on biological cell structures

Upon cellular stress conditions that are induced by exposure to cytotoxic agents, damage to DNA in the nucleus and changes to the mitochondrial membrane are common initial events [Ful10]. Furthermore, the permeability of the plasma membrane is an indication of cell viability [Tai08] [Fin05] [Maj95]. Knowledge of the functioning of these structures are of paramount importance in order to understand the morphological changes associated with cell death and the specific biochemical changes in providing potential targets for viability stains to assess cultured cells.

3.4 The cell's life cycle

The life cycle provides insight in cell division and thus tissue growth. The cell's nucleus contains genetic information in the form of chromatin, which consists of highly folded ribbon-like complexes of DNA. During cell division, chromatin fibres are folded and become visible under a light microscope as chromosomes. The cell's life cycle is fundamentally the duplication of the DNA in the chromosomes of a single cell such that the aforementioned cell can be divided into two genetically identical daughter cells. The eukaryotic cell's life cycle is divided into four sequential phases: G_1, S, G_2 and M (Fig. 3.6).

The two major phases of the cell life cycle are the synthesis phase (S-phase) and the mitosis phase (M-phase). DNA duplication occurs during the S-phase, which occupies about half of the cell-cycle time in a typical mammalian cell . Chromosome segregation and cell division occur in the M-phase, which requires less time than the S-phase. The M-phase involves a series of dramatic events that begin with nuclear division and ends with two genetically identical daughter cells each with a complete set of genes, a pair of centrioles and organelles [AB02].

Cells require much more time to grow and double their mass of proteins and organelles than they require to replicate their DNA and divide. Therefore, two gap phases are present in most cell cycles to afford cells time to grow and mature: a gap 1 phase (G_1-phase) between the M-phase and the S-phase, and a gap 2 phase (G_2-phase) between the S-phase and mitosis. Moreover, the two gap phases provide time for the cell to monitor the internal as well as the external environment to ensure that conditions are favourable and preparations are complete before the cell commits itself to the major upheavals of the S-phase and M-phase. The G_1-phase is especially important in this regard. If the extracellular conditions are inauspicious, cells delay progress through the G_1-phase indefinitely. Under certain conditions a cell enters a hibernating state known as G_0 in which they may remain for days, weeks or even years before resuming proliferation. Indeed, many cells remain in G_0 permanently until they die or the organism dies. If the extracellular conditions are favourable and signals to grow and divide are present, cells in early G_1 or G_0 progress through a commitment point near the end of G_1 known as the restriction point. After passing this point, cells are committed to DNA replication, even if the extracellular signals that stimulate cell growth and division are removed [AB02].

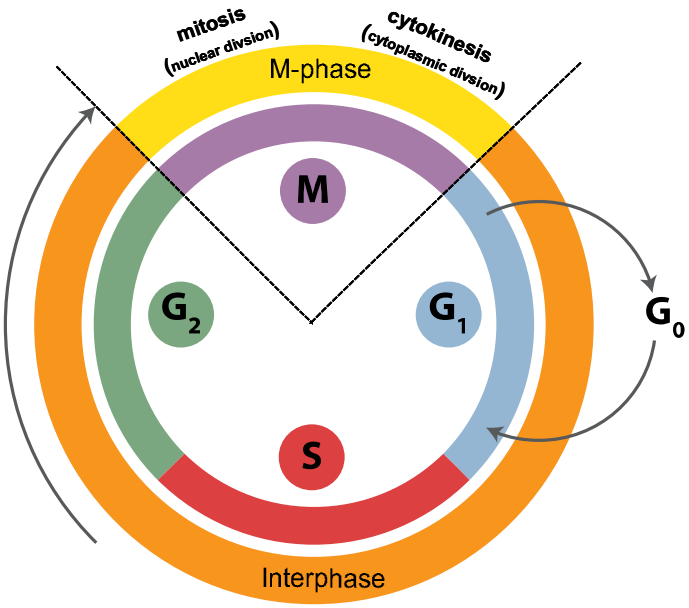

Figure 3.6: The phases constituting the cell cycle.

3.5 Types of cell death

3.5.1 Introduction

It is appropriate to start this section by stating that the determination of whether a cell is viable is not always straightforward [Sha05]. Cells can respond to stress in various ways ranging from the activation of survival pathways to the initiation of cell death that eventually eliminates damaged cells. Whether cells mount a protective or destructive stress response depends to a large extent on the nature and duration of the stress as well as the cell type [Bla12]. Also, there is often the interplay between these responses that ultimately determines the fate of the stressed cell. The mechanism by which a cell dies (i.e., apoptosis, oncosis or autophagic cell death) depends heavily on various exogenous factors as well as the cell's ability to handle the stress to which it is exposed. [Ful10].

The cell's initial response to a stressful stimulus is geared towards a defence against and recovery from the insult. However, if the noxious stimulus is unresolved, the cells then activate death signalling pathways. Cell death has many forms and shapes. Cell death research encompasses not only the study of programmed forms of cell death (both apoptosis and autophagic cell death), necrosis and other modes of cellular demise, but also the role these phenomena play in physiological and pathological processes including development, aging, and disease [Ful10].

The concept of cellular demise and terminology associated with that, has been evolving since

the 19th century. The term programmed cell death refers to controlled or regulated forms of death associated with a series of biochemical and morphological changes [Ful10].

Nowadays, programmed cell death is synonymous with apoptosis. The term apoptosis was first used to describe a particular morphology of cell death ([Ker72]) common to the vast majority of physiological cell deaths. The morphology of cells undergoing apoptosis appeared dissimilar and distinct from the morphology associated with necrosis [Ker72].

It is important to note that the processes of cell death and necrosis are not the same. Quite simply, necrosis is a final stage of cell injury that culminates in cell death.

3.5.2 Apoptosis

Apoptosis is the primary mechanism by which unneeded or senescent cells are physiologically absorbed by healthy adjacent cells and tissues [Bla11]. Apoptosis is a series of genetically pre-programmed biochemical and morphologic energy-requiring events that, after a specific external stimuli or internal cellular signal, result in the physiologic disappearance of a cell via its self-disintegration and packaging of its contents into membrane vesicles called apoptotic bodies. Apoptotic bodies are subsequently ingested by adjacent cells and phagocytes without provoking an inflammatory response or tissue damage [Bla12].

The series of morphologic energy-requiring events associated with apoptosis include: a change in the refractive index of the cell, cytoplasmic shrinkage, overall decrease in cell volume, nuclear condensation and cleavage of DNA into regularly sized fragments and the exposure of the protein H1 (see Fig. 3.7). The apoptotic cell divides into many parts by ‘blebbing’ and ‘budding’ to form what is known as ’apoptotic bodies’, containing cell organelles and nuclear materials surrounded by an intact plasma membrane. Additionally, there is little to no mitochondrial or organelle swelling [Fin05].

It is important to note that apoptosis includes both cell death and necrosis. Necrosis is simply a common endpoint for cell destruction and clean-up after any specific form of cell death [Lep03].

3.5.3 Oncosis

Oncosis is a form of cell death associated with cellular and organelle swelling, blebbing, and increased cell membrane permeability . The critical factor in this sequence of cellular events is ionic pump failure of the plasma membrane. The cause is primarily a decrease in cellular ATP due to ischemia or toxic agents that block ATP generation or markedly increase the plasma

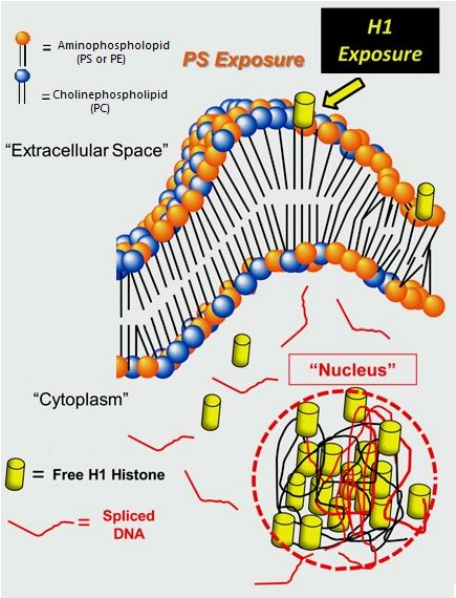

Figure 3.7: Typical plasma membrane of a non-viable cell.

membrane permeability [Maj95]. This process demonstrates typical cellular necrosis over the ensuing 24 hours. The breakdown of DNA is in a non-specific fashion, which is in contrast to the process of apoptosis [Lep03].

The morphological and biochemical features associated with the two types of cell death, apoptosis and oncosis are summarised in Table 3.1.

Apoptosis	Oncosis
Cell shrinks	Cell swells
Organelles remain intact	Organelles render non-functional
Controlled DNA degradation	Random DNA degradation
Chromatin condensation	General chromatin precipitation
Plasma membrane remains intact	Plasma membrane becomes permeable
Apoptotic body formation	Cell ruptures
Phagocytosis	Inflammatory response
Occurs in individual cells	Occurs in large groups of cells

Table 3.1: A comparison of the morphological and biochemical changes associated with apoptosis and oncosis

3.5.4 Necrosis

Necrosis is an advanced stage of cell death and can easily be recognised by the human eye without any need for microscopic detail. Necrosis is characterized by the primary loss of plasma membrane integrity and the uncontrolled release of cellular contents into surrounding tissues, triggering an inflammatory response, tissue damage, and scarring. Necrosis can occur either after apoptosis or after oncosis.

3.5.5 Autophagy

Autophagy ('self-eating') has considerable overlap with apoptosis [Lev08]. However, as opposed to apoptosis, autophagy normally serves a housekeeping function by recycling senescent or damaged cytoplasmic contents or organelles (as opposed to the cell itself). The hallmark of autophagy is the formation of isolation membranes that engulf targeted cytoplasmic material (or organelles), resulting in double-membraned vesicles called autophagosomes (autophagic vacuoles). Autophagosomes then undergo maturation by fusion with lysosomes to create autolysosomes. It is within the autolysosomes that auto-digestion occurs.

Autophagy permits a cell to survive periods of cellular famine through the auto-digestion and reuse of intracellular DNA/RNA, proteins, and lipids into free nucleotides, amino acids, and fatty acids, respectively. However, autophagy can be an alternative to apoptosis if the classic apoptotic mechanisms are damaged or are inhibited.

3.6 Assessment of cell viability

3.6.1 Introduction

Viable cells refer to healthy cells in a cellular culture, which have the capability to live, grow and develop [Pal78]. Cell viability is determined by the number of cells that are viable, based on a total cell sample. Cell viability is assessed by cell viability assays [Fin05]. Assays are specialised chemical stains used to indicate whether or not a cell population that has been exposed to an experimental stimulus is healthy.

Cell viability measurements are used to assess the stage of cancerous cells, the rejection or not of implanted organs as well as the effectiveness of a drug. Cell viability assays are also useful to determine optimal growth conditions for cell populations maintained in culture [May10]. There are various assays available to assess a variety of different markers that indicate the number

of non-viable cells (cytotoxicity assays), the number of viable cells (viability assays), the total number of cells or the mechanisms of cell death (e.g. apoptosis). Measurement of DNA content and metabolic activity are correlates that can offer more information about the physical condition of cells and cell cycle stage. Furthermore, the information derived from these assays can indicate whether or not a cell population that has been exposed to an experimental stimulus, is healthy or dying, actively dividing or in stasis, or has committed to an apoptotic pathway [May10]. It is important to note that the biological nature of the phenomenon under investigation determines which assay is appropriate, and at what stage in the life cycle of the cell culture it should be applied.

Assessments of viability depend on one or both of two cellular properties: (1) the intactness of the cell membrane, and (2) the physiological state of the cell [Cod01]. Most methods used to monitor cell viability are based on physical rather than metabolic properties of the cell, since the physical damage is less likely to be reversible. Measuring the metabolic processes of the cell, such as the reduction of 2,3-5 triphenyltetrazolium chloride (TTC), are not reliable, since enzymatic pathways may be temporarily non-functioning or some enzymes may still be present after cell death [Bak94].

Dye exclusion methods are based on the fact that only intact membranes are impermeable to large or charged molecules. Furthermore, intact membranes also maintain cytoplasmic gradients with the surrounding medium, thus retaining intracellular concentrations of ions and small molecules. This fact also reflects the physiological state of the cells in that energy is required to maintain gradients. Thus, methods that assay physiological properties of the cell are also dependent upon and indicative of an intact membrane [Cod01].

Non-viable cells with compromised cell membranes are easily detected by their inability to exclude dyes such as propidium iodide or trypan blue. These dyes leak through ruptured membranes and stain the contents of non-viable cells.

Since cells treated with apoptosis-inducing agents (e.g., cytotoxic drugs) maintain plasma membrane integrity until late in the process of cell destruction, the assays listed in this section are not suitable for the detection of the early stage of apoptosis, or for distinguishing apoptosis from necrosis. These assays are described in the paper by Vermes et al. [Ver00].

3.6.2 Methods based on membrane integrity

Assessing cell membrane integrity is one of the most common and straightforward ways to measure cell viability and asses cytotoxic consequences. Compounds that have cytotoxic effects often compromise cell membrane integrity and induce cell death. The reagents most often used

for assessing membrane integrity are dyes such as trypan blue or a variety of fluorescent probes that will penetrate only damaged, permeable membranes of non-viable cells. These are then easily identified visually by the presence of blue colour (with trypan blue) in a simple bright-field microscope, or by bright fluorescence seen by fluorescence microscopy.

The most widely used group of fluorescent probes are those that label nucleic acids . The most straightforward labelling methods use propidium iodide (PI) or 7-amino actinomycin D (7-AAD) to identify non-viable cells. These fluorescent dyes are normally excluded from the inside of viable cells. However, if the cell membrane has been compromised, they freely cross the membrane and stain the exposed nucleic acid in the cytoplasm (see Fig. 3.7). This method distinguishes viable cells with membranes that are still intact (not stained) from non-viable cells (stained). Staining of non-viable cells with PI has been performed on most cell types [Cod01]. Its broad application is most likely due to ease of use: the procedure is very simple, and the stained cells are bright red and easy to identify. 7-AAD is a useful alternative to PI. Like PI, 7-AAD penetrates only dead cells, but 7- AAD fluorescence is both less intense and at a longer wavelength (670 nm, versus 610 nm for PI).

Normally, eukaryotic cells maintain a specific asymmetry of phospholipids in the inner and outer leaflets of the cell membrane Figure 3.4. During cell death PS becomes abundant on the outer leaflet (see Fig. 3.7). Detecting this change in phospholipid asymmetry is one way to detect cell death. Alternatively, membrane integrity can be assessed by monitoring the passage of substances that are normally sequestered inside cells to the extracellular environment. One commonly measured molecule is lactate dehydrogenase (LDH), a soluble cytosolic enzyme that is released into the culture medium following loss of membrane integrity.

Healthy, intact cells can also be fixed (can be made permeable by a detergent), and similarly labelled as above to study cell cycle progression. Propidium iodide, used in cell cycle phase determination assays, labels DNA in cells undergoing various phases of the cell cycle. The PI dye directly intercalates with the base pairs on a DNA strand, its fluorescent intensity is directly proportional to the DNA content of the cell. Based on chromosome distribution, it can reliably indicate G_0/G_1 versus S versus G_2/M.

3.6.3 Methods based on physiological state

Introduction

Another property of viable cells is the maintenance of electrochemical gradients across the plasma membrane. Functional subsets of this general phenomenon include the maintenance

of pH and other ion gradients as well as the capacity for energy-yielding metabolism in mitochondria. These physiological processes can be exploited to distinguish viable from non-viable cells. The physiological state of a cell is assayed by probes that require the presence of metabolic processes in addition to an intact membrane.

Esterase activity

Cell viability can be assessed directly through the presence of cytoplasmic esterases that cleave moieties from a lipid-soluble non-fluorescent probe to yield a fluorescent product. The product is charged and thus retained within the cell, if membrane function is intact. Hence, viable cells are bright and non-viable cells are dim or non-fluorescent. Typical probes include fluorescein diacetate (FDA), carboxyfluorescein, and calcein [Cod01]. Variations in uptake or retention of the dye among individual cells or under different conditions affect the efficacy of particular probes.

Mitochondrial membrane potential

While the most prominent role for mitochondria is the production of ATP, the major source of cellular energy, these power generators have been linked to a multitude of cellular activity. Other important roles of mitochondria include cell signalling, cellular differentiation, cell death as well as the control of the cell cycle and cell growth. Given these collective functions, assessing mitochondrial activity gives a fair indication of cell viability [May10].

The permeabilisation of the mitochondrial membrane is the crucial irreversible event that leads to cell death. In Figure 3.8, the MPTP is in a closed state, which favours a decrease in ATP transport, parallel oligomerisation of Bax and a decrease in the mitochondrial transmembrane potential ($\Delta\Psi m$), which leads to the release of cytochrome c (see Fig. 3.8) from the intermembrane into the cytoplasm, thereby triggering cell death[Maz11].

One of the most commonly used probes for identifying viable cells through mitochondrial membrane potential assessment, is rhodamine 123, a cationic lipophilic dye that partitions into the low electrochemical potential of mitochondrial membranes. Active mitochondria in viable cells are stained bright green, because a loss of gradients within non-viable cells, results in loss of the dye [Cod01].

Another probe, JC-1, is a carbocyanine, a liquid crystal-forming dye used to analyse mitochondrial membrane potential. JC-1 Mitochondrial Membrane Potential Assay reliably probes mitochondrial membrane potential changes, occurring specifically in the early stages of apoptosis. On the other hand, Caspase-3 Fluorescence Assay detects mitochondrial-triggered apoptosis

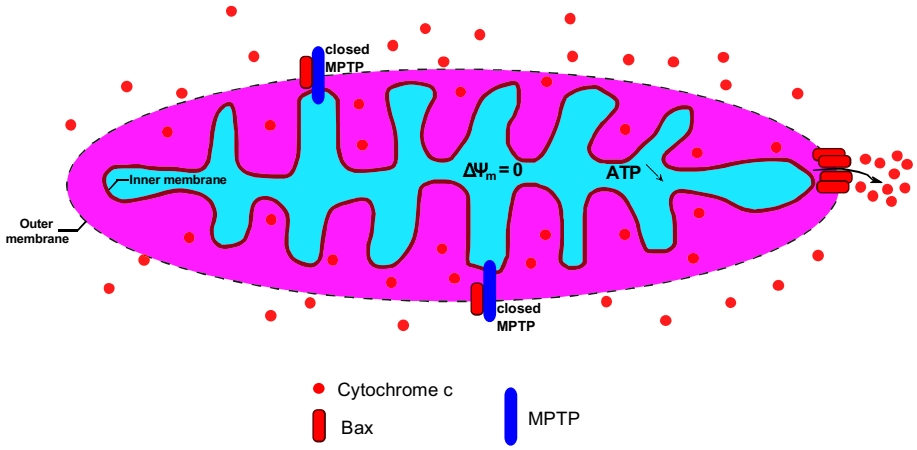

Figure 3.8: Structure of a mitochondria in a dying cell.

by identifying activation of the specific apoptotic marker, caspase-3 [May10].

Metabolic activity

Metabolic activity is commonly accepted as an alternative for measuring viability. A classic approach for assessing metabolic activity involves the use to tetrazolium salts that are cleaved in the mitochondria of metabolically active cell to from coloured, water-insoluble (MTT) or water-soluble (XTT, WST-1,WST-8) formazan salts that can be measured by absorbance. The MTT (methods of transcriptional and translational) assay has a long-held reputation as the conventional cell viability assay and carries with it a strong body of literature support. However, the very nature of the tetrazolium dye interferes with cell metabolism and the changes that result, may indicate whether or not the cell is viable and proliferating. Since the basis of this assay is the inherent dehydrogenase activity of viable cells, treatments that affect dehydrogenase activity may result in a discrepancy between actual viable cell number and that determined using formazan dye.

3.7 Tools for studying cell biology

3.7.1 Introduction

The light microscope is one of the most basic tools of a cell biologist. It allows for the non-invasive examination of viable cell cultures. Several different types of light microscopy are routinely used to study various aspects of cell structure. Three types of microscope modalities

are of specific interest in this study: bright-field, phase contrast and fluorescent microscopy. The three types of transmitted light microscopy techniques are described in the subsequent sections.

3.7.2 Bright-field microscope

Bright-field microscopy, in other words the direct observation of illuminated objects through a lens, is the most simplest and widely used method for cell observation. In bright-field microscopy the light passes directly through the cell and the ability to distinguish different parts of the cell depends on contrast resulting from the absorption of visible light by cell components (see Fig. 3.9a). It is usually available without any special devices, but the resulting contrast is rather low, which necessitates more complex recognition techniques ([Lon06],[Tsc08], [AB02]). On the other hand, bright-field microscopy is compatible with fluorescence microscopy, thus making it a popular and frequently applied microscopy technique. Hence, the decision to use bright-field images as a basis for cell recognition in this study.

In Figure 3.9, images of the same cell culture obtained by three kinds of light microscopy are compared.

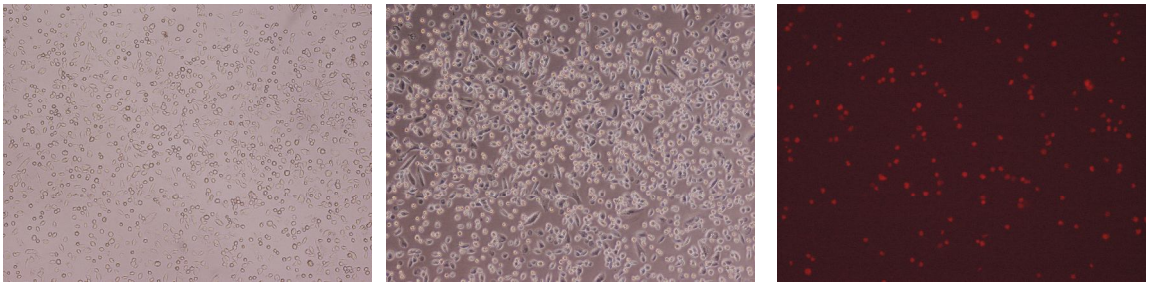

(a) Bright-field (b) Phase contrast (c) Fluorescent

Figure 3.9: Different types of transmitted light microscopy.

3.7.3 Phase contrast microscope

Phase contrast microscopy visualises the phase shift induced by the interaction of rays of light with objects varying in thickness or refractive index. When light passes through a living cell, the phase of the light wave is changed according to the difference of the refractive index of the cell and the refractive index of the surrounding medium. Thus, a relatively thick or dense part of the cell, such as the nucleus, retards light passing through it. The phase of light, consequently, is shifted relative to the light that has passed through an adjacent thinner region of the cytoplasm.

The phase contrast microscope exploit the interference effects produced when these two sets of waves recombine, thereby creating an image of the cell's structure [AB02].

Biologists and bioprocess engineers most often prefer phase contrast to bright-field micrographs. They claim that phase contrast micrographs (see Fig. 3.9b) enables them so see more cellular detail and that the visible contrast in phase contrast micrographs are much higher than in bright-field micrographs.

A drawback of phase contrast microscopy is that it requires special objectives that reduce the amplitude of incident light which also attenuated the light from fluorescent objects. Thus, making it more difficult to see fluorescent objects in fluorescence micrographs.

3.7.4 Fluorescent microscope

Fluorescent molecules absorb light at one wavelength and emit it at another, longer wavelength. If such a compound is illuminated at its absorption wavelength and then viewed through a filter that allows only light of the emitted wavelength to pass, it will glow against a dark background. Due to the dark background, even a minute amount of glowing fluorescent dye can be detected.

Fluorescent dyes used for staining cells are visible under a fluorescent microscope. This type of microscope is similar to an ordinary light microscope except that illumination light, from a very powerful source, is passed through two sets of filters: one to filter the light before it reaches the specimen and another to filter the light obtained from the specimen. The first filter passes only the wavelengths that excite the particular fluorescent dye, while the second filter blocks out the light that passes only those wavelengths emitted when the dye fluoresces (see Fig. 3.9c) [AB02].

Fluorescence microscopy is most often used to detect proteins or other molecules in cells and tissues. A very powerful and widely used technique is to couple fluorescent dyes to antibody molecules, which then serve as highly specific and versatile staining reagents that bind selectively to the particular macromolecules they recognise in cells [AB02].

3.8 Summary

Cell viability is not easily defined in terms of a single physiological or morphological parameter. Non-viable cells are characterised by permeable plasma membranes, the disruption of the mitochondria, DNA fragmentation and chromatin condensation.

The diversity of biological cells and their environments make it impossible to devise a single viability or enumeration assay applicable to all cell types. Each assay method has inherent

advantages and limitations and may introduce specific biases into the experiment; thus, different applications often call for different approaches.

Coupling viability assays to fluorescent probes enables the detection and visualisation of viable as well as non-viable cells in the same image by switching between the bright-field or phase contrast micrograph and the corresponding fluorescent micrograph.

The rapid progress in machine learning and pattern recognition makes it possible that more and more biological research can be carried out via imaged-based techniques. These techniques, if applied effectively, may enable the automatic non-invasive assessment of cell viability by exploiting the limitations of conventional tools used for studying cell biology.

Chapter 4

Materials And Experimental Conditions

4.1 Preparing a cell culture

There exist two basic ways for growing cells in culture namely as monolayers on an artificial substrate, the so called adherent culture, or as free-floating cells in the culture medium, the so called suspension culture. The adherent cell-line used for testing material in this work, were CHO (Chinese Hamster Ovary) cells. The cells were grown at 37.0° C in a Gibco® DMEM / F-12 (1:1) medium supplemented with 10% fetal calf serum (FCS) and 2mMol glutamine to produce an adherent culture. For microscope observation, the cells in the culture medium were dispensed into a polystyrene 24-well microplate (Fig. 4.1).

Figure 4.1: 24-Well microplate used for preparing the cell cultures.

A toxicity test was performed on the cell culture to induce cell death. An amount of 0.1Mol of the toxin called sodium azide (10-2M) was added to the culture of the CHO cells to enable the measurement of cell death kinetics. To obtain an accurate and objective training and testing standard, propidium iodide (PI) was added to the cell-lines to detect non-viable cells. PI emits

a deep red fluorescence (emission: 590nm) when excited with a green-yellow laser light (Fig. 4.2).

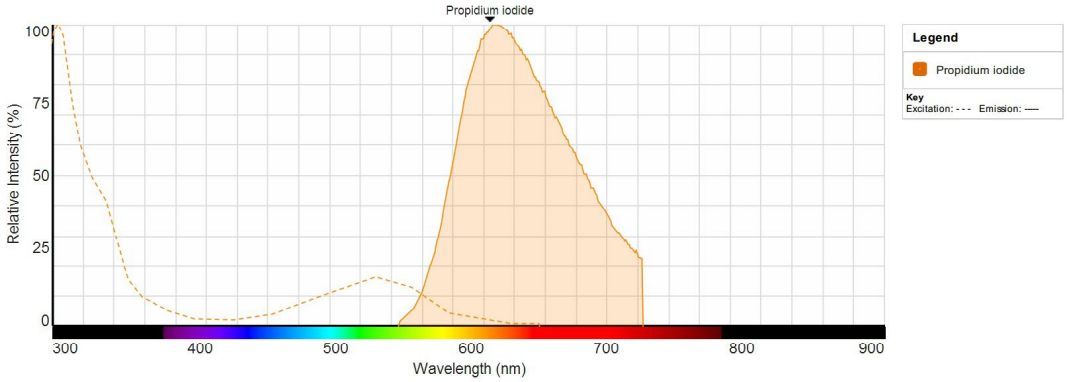

Figure 4.2: Excitation and emission spectra of propidium iodide [Tec].

Coupling an antibody to PI makes it possible to visualise non-viable and viable cells in the same image by switching between the bright-field micrograph and a filter specific to red fluorescence. Therefore, the viability of the cell cultures can easily be determined by manual counting of the cells in the micrographs. This viability value is taken as the gold standard for evaluating the system's performance.

4.2 Micrograph acquisition of cell cultures

Images of the 24-well microplate (Fig. 4.1) were captured with an inverted Nikon Eclipse TE 2000-U light microscope with fluorescence (Fig.4.3). A 10× Nikon phase contrast objective with a numerical aperture of 0.3 together with a Nikon DS-5Mc camera was used to obtain digitised images. For each microscope field, five micrographs were acquired: an in-focus bright-field (Fig. 4.4a), a phase contrast (Fig. 4.4a), a positive-defocus bright-field (Fig. 4.4c), a negative-defocus bright-field (Fig. 4.4d), and a fluorescence micrograph (Fig. 4.4e).

To obtain the positive- and negative-focused bright-field micrograph, the region of interest of the microscope field was imaged at two different focus planes f (perpendicular to the optical axis of the cell culture). More specifically, the microscope field was optically sectioned by moving the objective along the optical axis and imaging at ten microns above (f_1) and below (f_2) the in-focus level f_0. The incremental changes to the microscope focus was manually done.

Biologists and bioprocess engineers prefer phase contrast, positive- and negative-focused bright-field micrographs, because according to them visually, these micrographs , have a greater

Figure 4.3: Nikon Eclipse TE microscope used for the acquisition of micrographs.

depth of field, more contrast and allows them to see sub-cellular boundaries and organelles in finer detail. Hence, these micrographs were acquired in addition to in-focus bright-field micrographs, to serve as a comparison and to investigate if these claims made by the experts have any mathematical significance.

4.3 Dataset description

In total, seven sets of micrographs of CHO cell cultures were acquired to be used in the cell viability determination experiments. The micrographs were taken at a time stamp where approximately a quarter of the cells were non-viable. The rationale behind this procedure is that cell cultures with more than 25% non-viable cells are of no interest to biologists. Each set consist of five micrographs captured by five different microscopy techniques as described in section 4.2.

The behaviour of an adherent cell-line depends on the natural environment. If the environmental conditions are favourable, then healthy cells will adhere to the surface of a well and grow, otherwise the cells will stay in suspension. All the cells that are clearly visible in the bright-field micrograph at focus (see figure 4.5) are cells in suspension. Adherent cells exhibit very low contrast and as a result are barely visible in the bright-field at focus micrograph. However, both adherent and suspended cells are visible in the phase contrast (Fig. 4.5), the positive- , and the negative-focused bright-field micrographs. In genera, a phase contrast micrograph (see Fig. 4.5) has much better contrast as a result of phase information as opposed to intensity information.

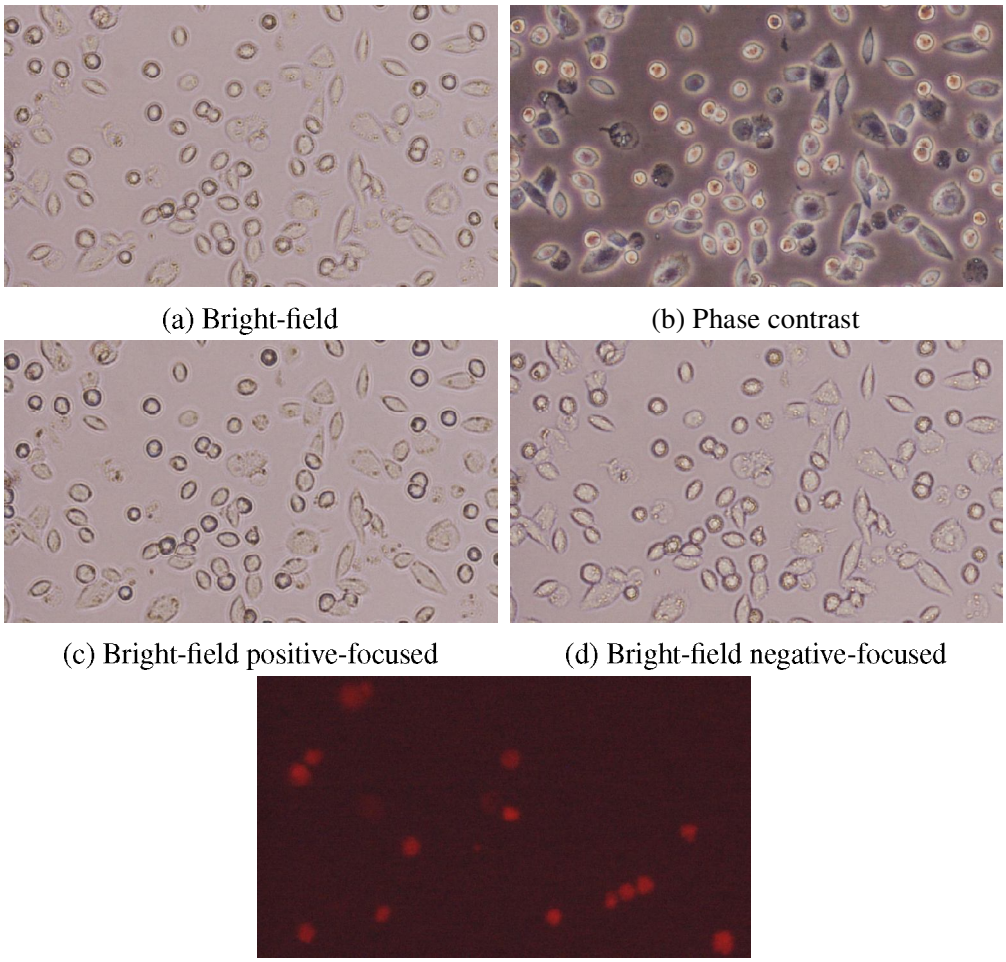

(a) Bright-field (b) Phase contrast

(c) Bright-field positive-focused (d) Bright-field negative-focused

(e) Fluorescence

Figure 4.4: A typical sample image set.

Cells in culture exhibit a great diversity of shape and size, which is also visible from the micrographs in Figure 4.5. In general, adherent cells have a more irregular appearance, whereas cells in suspension appear smaller in size and more round in shape.

In the fluorescence micrograph, the non-viable cells appear bright red (see Fig.4.5), whereas the surrounding viable cells are invisible.

The fluorescence micrographs were used to identify and label the non-viable cells, whereafter the phase contrast micrographs were used to label the adherent and suspended cells.

After visual inspection of the acquired micrographs it is apparent why biologists and bioprocess engineers prefer phase contrast and defocused bright-field micrographs. In these micrographs both adherent and suspended cells are clearly visible. Furthermore, micrographs acquired by these microscopy techniques exhibit much more cellular detail, in other words the shape and

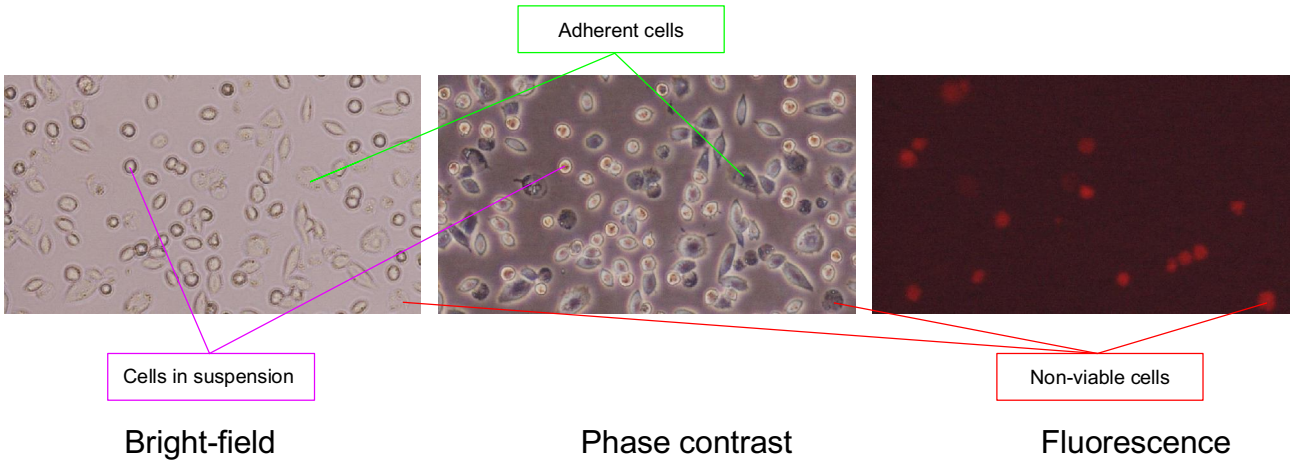

Figure 4.5: Illustration of the appearance of adherent, suspended and non-viable cells.

size of the cells are more defined and cellular sub-structures like the nucleus of suspended cells are clearly visible in the phase contrast micrograph.

4.4 Technical specifications

In this section the technical specifications of the hardware, software and programming languages used to perform the experiments, are briefly summarised. The details pertaining to the implementation of individual units in the cell viability determination pipeline are thoroughly described under the "Implementation" sections in subsequent chapters.

- Hardware:
  - A laptop equipped with an Intel(R) Core(TM) i5-3317U/1.7GHz processor and 4-GB RAM.
- Software:
  - MATLAB version 7.11.0.584 (R2010b) supplemented with a Image Processing Toolbox Version 4.0 [MAT10].
  - LIBSVM ([Cha11]) compiled as a dynamic link library for MATLAB.
  - KNIME version 2.8.0 [Ber07].
- Programming languages:

- MATLAB
- C++

4.5 Summary

In order to understand the eventual objectives of this study, it is important to first obtain sufficient knowledge of the processes that precedes the study. In this chapter, it was described how cell cultures are prepared in order to obtain micrographs from it for the sake of preparing data sets. Moreover, the technical specifications of the equipment to perform the study were also stated.

Chapter 5

Keypoint-Based Viability Determination Framework

In this chapter, a keypoint-based unstained cell viability determination framework is presented. Micrographs are obtained from transmitted light microscopy of cultured cells. The main idea of the framework is to train several classifiers with cell samples, the viability of which are known, such that the classifiers learn from the example micrographs some criteria for distinguishing viable from non-viable cells based merely on their visual appearance. In this learning process, different types of features are extracted, investigated and evaluated based on how well they support classification.

The essential building blocks of this keypoint-based unstained cell viability determination framework are illustrated in Figure 5.1. The framework is composed of three modules: an acquisition (Figure 5.1 - (a)), a training (Figure 5.1 - (b)) and a test module (Fig. 5.1 - (c)).

In the acquisition module, micrographs of cell cultures which have been exposed to a toxin are captured with a laboratory microscope (Fig. 5.1 - (1)). More often than not, a cell is expressed in a micrograph as one or more blobs in intensity. A blob is a maximum of the normalised Laplacian in scale space ([Lin98]). It is also called an interest point or a keypoint. The cells in the acquired micrographs are manually detected and labelled, whereafter scale invariant feature transform (SIFT) keypoints [Low99] are extracted (Fig. 5.1 - (2)). Only the keypoints which are arbitrarily close to the manually selected points in the micrographs are kept, the remainder are discarded. Henceforth, the keypoints are classified into viable-adherent, viable-suspended, and non-viable cell keypoints. It is important to realise that there may be multiple keypoints associated with a single cell.

After the keypoint detection stage, an image patch of each keypoint is collected within a

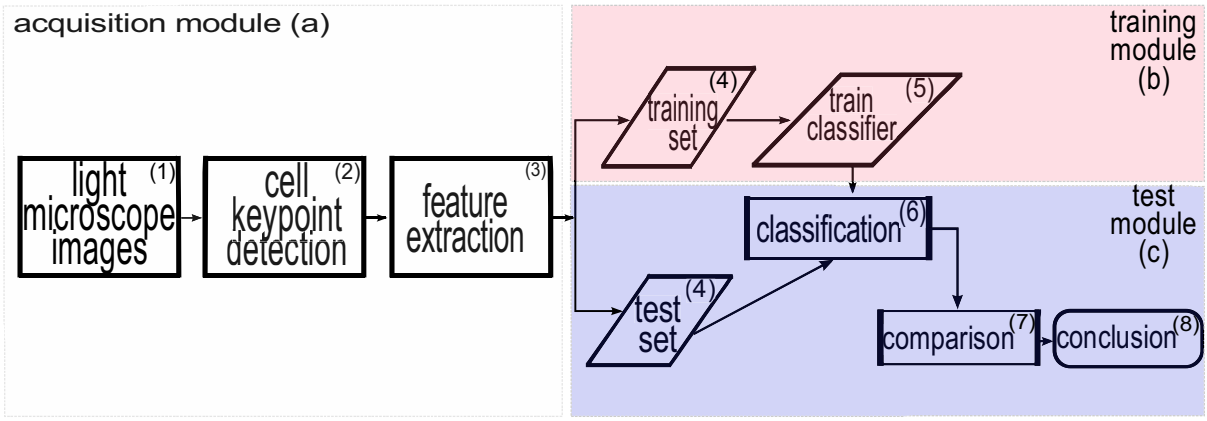

Figure 5.1: Illustration of the overall cell viability determination process from bright-field micrographs.

square window W around the cell keypoint centre. The size of the patch is proportional to the scale parameter of that particular SIFT cell keypoint ($keypoint_{scale}$). Thus, a different patch is extracted for each cell keypoint in the micrograph [Mua13]. These scale dependent patches are then used to compute various features (Fig. 5.1 - (3)).

In the training module, only the extracted feature vectors from one micrograph is considered for the training set (Fig. 5.1 - (4)). This one micrograph is used for training various classifiers (Fig. 5.1-(5)). Essentially, the classifiers are trained to classify the extracted feature vectors into two different classes: viable or non-viable.

In the test module, the trained classifiers are used for classifying the extracted feature vectors that belong to the micrographs in the test set (Fig. 5.1-(4)). To evaluate the framework's performance, the resulting classification label of each keypoint is compared to the known class label associated with that particular keypoint. The classification step is repeated for each micrograph in the test set in order to get a cross-validation estimate of the classification performance associated with each classifier/feature combination.

In this thesis, the framework described above is repeated for the four different transmitted light microscope modalities. Thus, a cross-validated classification performance for each of the microscope modalities are produced, which allows for a comparison between modalities, features and classifiers.

Chapter 6

Features Considered For Cell Viability Determination

6.1 Introduction

Selecting the most informative set of features, given a specific problem, to apply in training of any classifier is crucial for obtaining proper classifications results. The field of machine learning has produced a multitude of features to serve as inputs for learning algorithms. These features may include simple local and non-local properties, including the pixel value, the mean, the gradient magnitude, the standard deviation, and entropy ([Jur10]).

Training a classifier, with a large number of features, is challenging due to the "curse of dimensionality" which, if not done carefully, can complicate the decision space and make it difficult to find an optimal solution. Therefore, it is necessary to find the features that are most descriptive of the problem at hand.

In this section the multitude of features that are considered to be the best to distinguish between viable and non-viable cell keypoints are introduced and mathematically described.

6.2 Scale invariant feature transform

6.2.1 Introduction

The scale invariant feature transform (SIFT) is a method by which distinctive features can be extracted from images to be used for image matching [Low99]. SIFT features associated with SIFT keypoint have been successfully used for object recognition. These features are invariant

to image scale and rotation, and are shown to provide robust object recognition despite change in illumination. These are all attributes, which make these features ideal for the use in this unstained cell viability determination framework. In the subsequent sections, the steps that need to be followed to obtain these SIFT descriptors and other features associated with SIFT keypoints are described.

6.2.2 SIFT descriptors

SIFT descriptors are the features associated with SIFT keypoints [Low99]. SIFT descriptors are a class of local image features, which characterise the neighbourhood of each SIFT keypoint in a scale- and orientation-independent way.

The SIFT descriptors are created by first computing the gradient magnitude and orientation at each image sample point in a region around the cell keypoint, as shown on the left part of Figure 6.1. These values are weighted by a Gaussian window, indicated by the overlaid blue circle. Thus, the weight of a sample point depends on its distance from the keypoint; the farther away from the cell keypoint, the smaller the weight of the sample magnitude. These samples are then accumulated into orientation histograms summing the contents over 4×4 subregions, as shown on the right part of Figure 6.1, with the length of each arrow corresponding to the sum of the gradient magnitudes near that direction within the region. Figure 6.1 shows a 4×4 descriptor array computed from a 16×16 set of samples. The total number of descriptor features describing the region around a cell keypoint is $4 \times 4 \times 8 = 128$. These 128 values form the feature vector, which uniquely defines a cell keypoint.

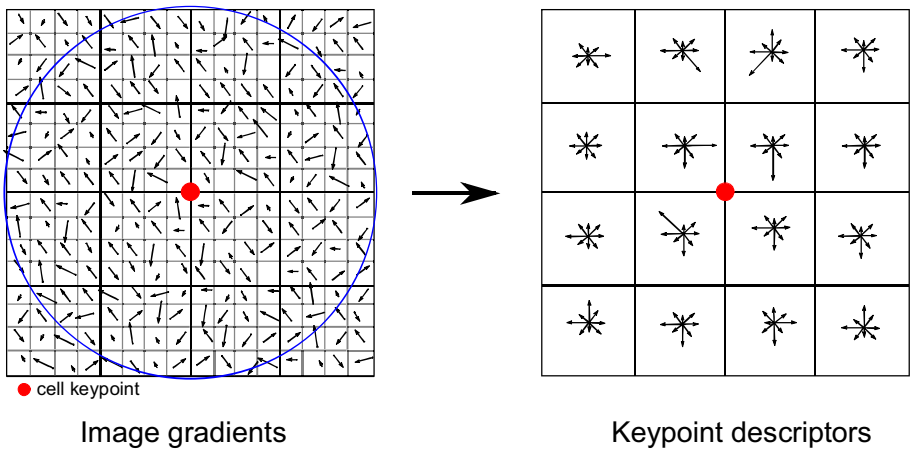

Figure 6.1: SIFT descriptors associated with a SIFT keypoint.

6.2.3 Difference-of-Gaussian value and principal curvatures ratio

Two additional features for each cell keypoint were obtained from the SIFT algorithm: the difference-of-Gaussian (DOG) value and the principle curvatures ratio (PCR). For information regarding the computation of these values please refer to the original publication [Low99].

6.3 Ray features

6.3.1 Introduction

Ray features consider image characteristics at distant contour points, capturing information which is difficult to represent with standard features [Smi09]. Ray features have been successful in recognising irregular shapes, such as cells in micrographs [Smi09] [Mua13]. The ray features adapted by [Mua13] was used in this thesis.

6.3.2 Mathematical description of ray features

In order to compute the Ray features at a cell keypoint $\mathbf{r}$ (see Fig. 6.2 for details) in an image $\mathbf{I}$, the closest edge point $\mathbf{r}'$ along a direction θ_w needs to be found. Ray features are four sets of features [Smi09]. The first three are:

(i) the distance $R_d(\mathbf{r}, \theta_w)$ between $\mathbf{r}$ and $\mathbf{r}'$:

$$R_d(\mathbf{r}, \theta_w) = \|(\mathbf{r}' - \mathbf{r})\|, \tag{6.1}$$

(ii) the gradient norm $R_n(\mathbf{r}, \theta_w)$ at $\mathbf{r}'$:

$$R_n(\mathbf{r}, \theta_w) = \|\nabla \mathbf{I}(\mathbf{r}')\|, \tag{6.2}$$

(iii) the gradient angle $\alpha = R_\alpha(\mathbf{r}, \theta_w)$ at $\mathbf{r}'$:

$$R_\alpha(\mathbf{r}, \theta_w) = \frac{\nabla \mathbf{I}(\mathbf{r}')}{\|\nabla \mathbf{I}(\mathbf{r}')\|} \cdot \theta_w. \tag{6.3}$$

Eight values for the angle $\theta_k, k = 1, 2, 3, ...8$ were used to obtain 24 features.

The fourth set of the Ray features is the distance difference $R_{dd}(\mathbf{r}, \theta_w, \theta_{w'})$ defined as follow:

$$R_{dd}(\mathbf{r}, \theta_w, \theta_{w'}) = R_d(\mathbf{r}, \theta_w) - R_d(\mathbf{r}, \theta_{w'}). \tag{6.4}$$

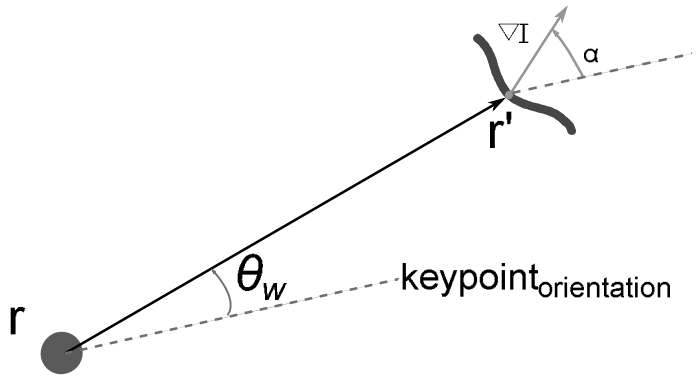

Figure 6.2: Ray feature adjusted to cell keypoints. This figure after [Mua13] is an adapted version of the pixel-based ray features in [Smi09]

Ray features are sensitive to scale and orientation. In order to make them orientation-invariant, all angles, i.e. the eight θ_w angles and the gradient angle feature $R_\alpha(\mathbf{r}, \theta_w)$, were defined with respect to the $keypoint_{orientation}(\mathbf{r})$.

The Ray features were made scale-invariant by measuring the distances $R_{dd}(\mathbf{r}, \theta_w, \theta_{w'})$ in units of $keypoint_{scale}(\mathbf{r})$. Furthermore, the gradient was computed by using the following equation for its x component:

$$\frac{\partial \mathbf{I}(\mathbf{r}')}{\partial x} = \mathbf{I}({r_x}' + \tau \cdot \text{keypoint}_{scale}(\mathbf{r}), {r_y}') - \mathbf{I}({r_x}', {r_y}') \tag{6.5}$$

where τ is a constant that was set equal to 1. A similar equation was used for the y component. Before applying equation 6.5, the micrograph was smoothed by a Gaussian filter with a standard deviation of 1 [Mua13] and the edges were obtained by applying the Canny edge detection algorithm [Can86].

6.4 Intensity stencil

6.4.1 Introduction

Direct sampling of intensity values in an image neighbourhood is actually a simple approach that allows a classifier to learn directly from the input data [Jur10][Lon06][Wei07]. Two image neighbourhood sampling techniques are available: one approach samples the image pixels using a patch and the other approach using a stencil. In the subsequent sections these two sampling techniques will be described.

6.4.2 Intensity stencil

An intensity stencil contains the same number of samples as a patch, yet covers a larger area of the data. Therefore, an intensity stencil is a more efficient representation for sampling the intensity values in a neighbourhood around a cell keypoint.

The idea of sampling an image by means of a stencil instead of a patch has been used for neuron detection in electron microscopy [Jur10], for sampling 3D vessels [Mit10] and for detecting cells in bright-field micrographs [Mua13].

In this thesis, the approach by Mualla et al. [Mua13] was followed to sample the intensities surrounding a cell keypoint. The $keypoint_{scale}$ and $keypoint_{orientation}$ associated with a SIFT keypoint were used respectively, to align a radial stencil and to sample the neighbourhood surrounding a cell keypoint in units of $keypoint_{scale}$ as demonstrated in Figure 6.3. The result is a scale and orientation-invariant approach to sampling the intensity values surrounding a cell keypoint. In order to make it invariant to the linear shift of intensity, the mean intensity of the stencil was subtracted from all stencil nodes.

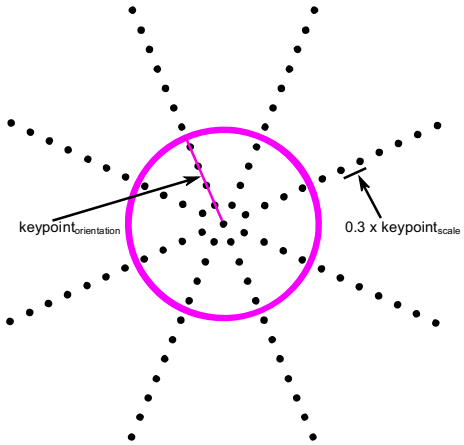

Figure 6.3: Radial intensity stencil. The stencil is aligned with the keypoint orientation. The distance between two successive nodes is $0.3 \times keypoint_{scale}$. This figure is extracted from [Mua13].

6.4.3 Pixel patch

The idea of sampling an image by means of a pixel patch has been used for automatic detection of unstained viable cells in bright-field images [Lon06] and multi-class detection of cells in multi-contrast composite images [Lon10].

In this thesis the intensity values surrounding a cell keypoint, were sampled by means of a static square pixel patch as demonstrated in Figure 6.4. The size of the square pixel patch was set equal to twice the average $keypoint_{scale}$ of all the cell keypoints in the micrograph.

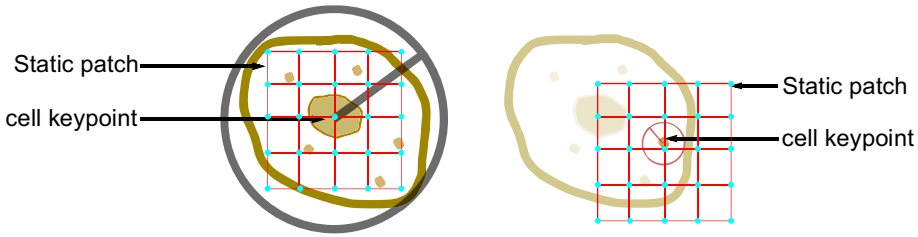

Figure 6.4: Static square pixel patch used for sampling the raw intensity values surrounding a cell keypoint. The side length of the patch is equal to twice the mean $keypoint_{scale}$ value.

6.5 Variance map features

The local variation of intensity in an image, the so called variance map, has been successfully used for identifying regions of an image that contain cells [Wu95]. The variance map value at a pixel is simply the variance of intensities in a neighbourhood centred at this pixel.

In this thesis, the variance map for a cell keypoint was computed, after [Mua13], over a square neighbourhood centred at the given cell keypoint. The size of the square neighbourhood was proportional to the $keypoint_{scale}$. For each cell keypoint $\mathbf{r}$, three variance map features were computed:

$$\text{Vmap}(r_x, r_y, G(\mathbf{r}, c)) = \frac{1}{G^2(\mathbf{r}, c)} \cdot \sum_{g=r_x-M}^{r_x+M} \sum_{h=r_y-M}^{r_y+M} [I(g,h) - \mu(r_x, r_y, G(\mathbf{r}, c))]^2 \tag{6.6}$$

where $I(g,h)$ is the grey level intensity of a cell keypoint $\mathbf{r}$ in an image $\mathbf{I}$ centred at (g,h), $G(\mathbf{r}, c) = c \times keypoint_{scale}(\mathbf{r}), c \in \{2,4,6\}$ is a value denoting the width of the considered square neighbourhood, $M = (G(\mathbf{r}, c) - 1)/2$ and $\mu(r_x, r_y, G(\mathbf{r}, c))$ is the mean intensity within the square neighbourhood, computed by

$$\mu(r_x, r_y, G(\mathbf{r}, c)) = \frac{1}{G^2(\mathbf{r}, c)} \cdot \sum_{g=r_x-M}^{r_x+M} \sum_{h=r_y-M}^{r_y+M} I(g,h) \tag{6.7}$$

6.6 Texture features

6.6.1 Introduction

Everyday texture terms like rough, silky and bumpy refer to the touch sensation. A texture that is rough to touch has a large difference between high and low points and the space between the highs and lows is approximately the size of a finger. A texture that is silky has little difference between the low and high points, and the spacing between points is close together relative to the size of a finger. Image texture can be described in the same way, except that the highs and lows are brightness values (also called grey levels) instead of elevation changes. A window of a specific $V \times V$ size is used for probing the image to determine the spacing between these high and low brightness values [HB07]. It has been demonstrated that spatial statistics computed on the grey levels of an image, are able to provide proper descriptors of the perceptual feeling of texture [Har79]. Methods based on texture analysis have been used successfully to identify neoplastic nuclei by characterising chromatin structures in breasts ([Wey98][DW00]) as well as in prostate tumours ([Yog96]) and to segment chromatin regions ([Bei95]).

The texture features used in this thesis are classified as second-order statistics, computed using the Grey Level Co-occurrence Matrix (GLCM) [Har73].

A GLCM considers the relation between two pixels in a patch, called the reference and the neighbour pixel. The neighbour pixel can be horizontally ($\theta = 0°$), vertically ($\theta = 90°$) or diagonally ($\theta = 45°$ or $\theta = 135°$) relative to the reference pixel (see Fig. 6.5 for details). A GLCM is created by calculating how often a reference pixel with grey-level intensity value $i*$ occurs relative to a neighbouring pixel with the intensity value $j*$, where the neighbouring and reference pixels are separated by the distance $dist$. Each element at position ($i*$,$j*$) in the co-occurrence matrix specifies the number of times that a reference pixel with value $i*$ occurred relative to a neighbouring pixel with value $j*$ in a patch, separated by the distance $dist$. The final step for constructing a GLCM is to normalisation, such that the sum of its elements is equal to 1. Each element at position ($i*$,$j*$) in the normalised GLCM is the joint probability occurrence of pixel pairs having grey level values $i*$ and $j*$ in the patch. Therefore, any GLCM element $P_{dist,\theta}(i^*, j^*)$ reflects the distribution of the probability of occurrence of a pair of grey levels (i^*, j^*) separated by a given distance $dist$ in the angular direction θ.

An example of how a horizontal co-occurrence matrix is calculated from an image is shown in Figure 6.6. In this illustration the horizontal relationship between pixels were used to construct the GLCM, where $dist = 1$. Element (1,1) in the GLCM contains the value 2, because there are two instances in the image where two horizontally adjacent pixels have the respective values of 1

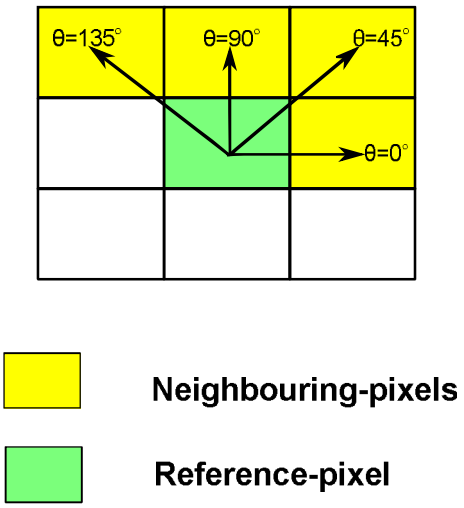

Figure 6.5: Example of relationship between reference pixel and neighbouring pixels.

and 1 (one to the right and one is to the left of the reference pixel). Elements (1,2) and (2,1) in the GLCM contain the value 2, because there are two instances in the image where two horizontally adjacent pixels have the values 1 and 2 considering the neighbour to the right and then again considering the neighbour to the left. A GLCM matrix is typically symmetric [Har73][Har79].

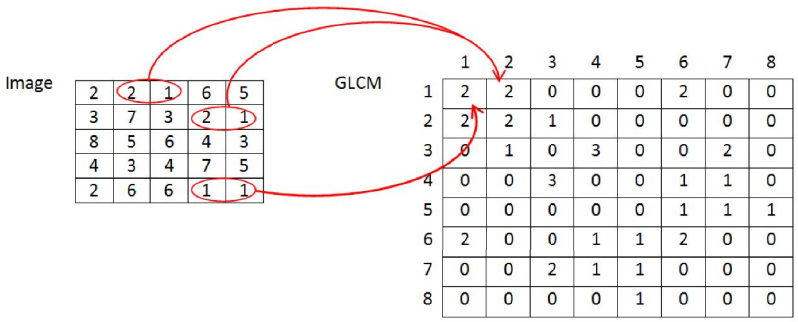

Image				
2	2	1	6	5
3	7	3	2	1
8	5	6	4	3
4	3	4	7	5
2	6	6	1	1

GLCM	1	2	3	4	5	6	7	8
1	2	2	0	0	0	2	0	0
2	2	2	1	0	0	0	0	0
3	0	1	0	3	0	0	2	0
4	0	0	3	0	0	1	1	0
5	0	0	0	0	0	1	1	1
6	2	0	0	1	1	2	0	0
7	0	0	2	1	1	0	0	0
8	0	0	0	0	1	0	0	0

Figure 6.6: Example of how a co-occurrence matrix for an image is constructed.

In this thesis, the patches extracted around each cell keypoint were quantised to 16, 32, 64, 128 and 256 grey-levels/pixel before a GLCM was calculated for each quantisation level. Henceforth, five symmetric GLCMs were calculated for each cell keypoint, by tabulating the grey-level co-occurrence probabilities based on the spatial relations of pixels, separated by a distance $dist = 1$ in all four of the angular directions ($\theta = 0°, 45°, 90°, 135°$). The summation of the four symmetric GLCMs' results in a rotation-invariant matrix [Arv04], defining a cell keypoint. The relative position vector was selected in the same manner as was done by Haralick [Har73].

6.6.2 Mathematical description of grey texture features

The grey texture features, computed for each cell keypoint, are based on the GLCM and Haralick features [Har73]. Haralick assumed that the texture information is contained in the GLCM, thus calculating the texture features from it. Although he extracted fourteen features from the GLCM, only five are commonly used because it was demonstrated that the fourteen features are highly correlated and that only five of them are more than sufficient to obtain satisfactory classification rates [Con80]. The five features commonly used are energy, homogeneity, contrast, correlation and entropy.

From the GLCM, the five features were calculated as follows[Mal03]:

$$Energy = \sum_{i^*=1}^{F} \sum_{j^*=1}^{F} P_{dist,\theta}^2(i^*, j^*) \tag{6.8}$$

$$Contrast = \sum_{i^*=1}^{F} \sum_{j^*=1}^{F} (i^* - j^*)^2 P_{dist,\theta}(i^*, j^*) \tag{6.9}$$

$$Correlation = \sum_{i^*=1}^{F} \sum_{j^*=1}^{F} \frac{(i^* - \mu_{i^*})(j^* - \mu_{j^*}) P_{dist,\theta}(i^*, j^*)}{\sigma_{i^*}\sigma_{j^*}} \tag{6.10}$$

$$Homogeneity = \sum_{i^*=1}^{F} \sum_{j^*=1}^{F} \frac{P_{dist,\theta}(i^*, j^*)}{1 + |i^* - j^*|} \tag{6.11}$$

$$Entropy = -\sum_{i^*=1}^{F} \sum_{j^*=1}^{F} P_{dist,\theta}(i^*, j^*) \log P_{dist,\theta}(i^*, j^*) \tag{6.12}$$

In these formulas, $F \in (16, 32, 64, 128, 256)$ is the number of grey levels, i^* and j^* are the different grey levels and $P_{dist,\theta}(i^*, j^*)$ is the value of the GLCM at grey level pair (i^*, j^*).

6.6.3 Mathematical description of colour texture features

In the last two decades, the study of texture has been extended to the study of texture in colour images [Arv04]. These novel colour texture study approaches are based on existing grey level methods that are adapted to take into account the colour information.

In the literature, three different families of approaches to colour texture analysis can be found. The first approach is a multispectral extension of the co-occurrence method since co-occurrence matrices are computed both between and within the colour bands. The second approach uses

joint colour-texture features: colour features are added to grey scale texture features as inputs for a classifier. The third approach uses grey scale texture features computed on a quantised colour image. A comparison study [Arv04] concluded that the multispectral colour texture approach outperformed the other two approaches by having the highest classification rate. Therefore, the multispectral colour texture approach was used in this thesis to exploit the colour information embedded in the micrographs.

The multispectral colour texture approach takes into account the correlations between the colour bands while computing the texture features as illustrated in Figure 6.7. Statistical descriptors are computed both within and between channels to give information on the whole colour texture [Ros80],[Arv04]. This method is an extension of the method based on the co-occurrence matrix of an image [Har73].

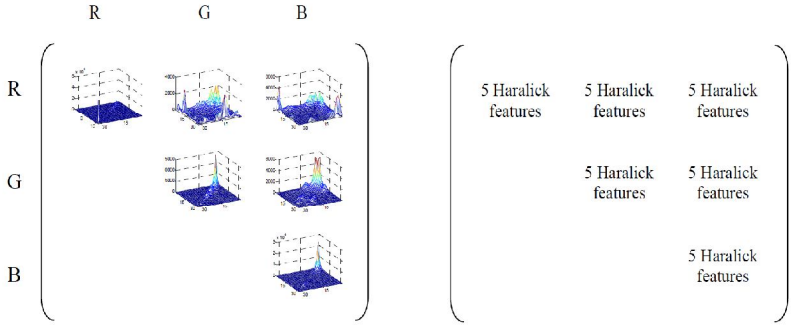

Figure 6.7: Construction of a six co-occurrence matrices to capture colour texture information and calculate texture features. This figure is extracted from [Arv04]

In this thesis, colour micrographs are coded on three channels, leading to six different co-occurrence matrices:(R,R), (G,G), (B,B) that are the same as the GLCMs computed on one channel and (R,G), (R,B), (G,B) that take into account the correlations between the channels. For each of the six co-occurrence matrices, the five Haralick features described above were calculated, which resulted in a total of 30 colour texture features per cell keypoint (see Fig. 6.7 for details).

Chapter 7

Multidimensional Scaling

7.1 Introduction

High-dimensional datasets can be very difficult to visualise. While data in two dimensions can be plotted to show the inherent structure, equivalent high-dimensional plots are much less intuitive. To aid visualisation of the structure of a dataset, the dimension needs to be reduced in some way.

The simplest why to accomplish dimension reduction is by taking a random mapping of the data [Kas98]. Though this allows some degree of visualisation of the data structure, the randomness of the choice leaves much to be desired. In a random mapping the more interesting structures within the data may be lost.

To address this concern, a number of supervised and unsupervised linear and non-linear dimensionality reduction algorithms have been developed. Examples of algorithms developed are isometric mapping [Ten00], locally linear embedding [Row00], [Kru64] to name but a few. The linear dimensionality reduction algorithms often miss important non-linear structures in the data. Non-linear projection algorithms can be thought of as an attempt to generalise linear algorithms to be sensitive to the non-linear structures in the data [Has01]. Typical non-linear projection problems are unsupervised i.e., it learns the high-dimensional structure of the data from the data itself, without the use of predetermined classification [Dud12].

One such non-linear projection algorithm is called multidimensional scaling (MDS). MDS seeks a low-dimensional representation of the data in which the distances respect well the distances in the original high-dimensional space [Bor05].

7.2 Description of multidimensional scaling

Beginning with observations $\mathbf{x}_1, \mathbf{x}_2, ..., \mathbf{x}_N \in \mathbb{R}^p$, and let $d_{aa'}$ be the distance between two observations a and a'. Most often the Euclidean distance $d_{aa'} = \|\mathbf{x}_a - \mathbf{x}_{a'}\|_2$ is selected, but other metrics may also be considered. MDS algorithms only require the dissimilarities $d_{aa'}$ between the observations and not the original data points $\mathbf{x}_a, a = 1, 2, ..., N$.

Multidimensional scaling seeks values $\mathbf{z}_1, \mathbf{z}_2, ..., \mathbf{z}_N \in \mathbb{R}^n$ $(n < p)$ to minimize the so-called *stress function* [Has01]:

$$S_M(\mathbf{z}_1, \mathbf{z}_2, ..., \mathbf{z}_N) = \sum_{a \neq a'} (d_{aa'} - \|\mathbf{z}_a - \mathbf{z}_{a'}\|_2)^2. \tag{7.1}$$

Equation 7.1 is known as *Kruskal-Shepard scaling*. A mapping of the data to a low-dimensional subspace is achieved by minimising S_M. A gradient descent algorithm minimizes S_M in a manner that preserves the pairwise distances of the high-dimensional space as best as possible [Has01].

A variation on least squares scaling is the so-called *Sammon mapping* which minimizes:

$$S_{S_m}(\mathbf{z}_1, \mathbf{z}_2, ..., \mathbf{z}_N) = \sum_{a \neq a'} \frac{(d_{aa'} - \|\mathbf{z}_a - \mathbf{z}_{a'}\|_2)^2}{d_{aa'}}. \tag{7.2}$$

In this instance more emphasis is placed on preserving smaller pairwise distances. A gradient descent algorithm is also used to minimize S_{S_m}. Least squares and Sammon mapping are referred to as *metric* scaling methods, in that the actual dissimilarities are approximated.

As described above, various methods exist that represent high-dimensional data in a low-dimensional coordinate system. However, MDS is one such method that explicitly tries to preserve all pairwise distances [Has01]. Hence, the reason for selecting *Sammon mapping* to visualise the low-dimensional mapping of the high-dimensional feature vectors.

7.3 Software implementation methodology

The professional open-source software platform called KNIME ([Ber07]) was used to inspect the various features extracted. The pipeline which was constructed in KNIME to perform the mapping and visualisation is depicted in Figure 7.1.

The MDS node in Figure 7.1 employs the *Sammon mapping* algorithm. This procedure is repeated a specified number of epochs. The scatter plot node is used to visualise the projected

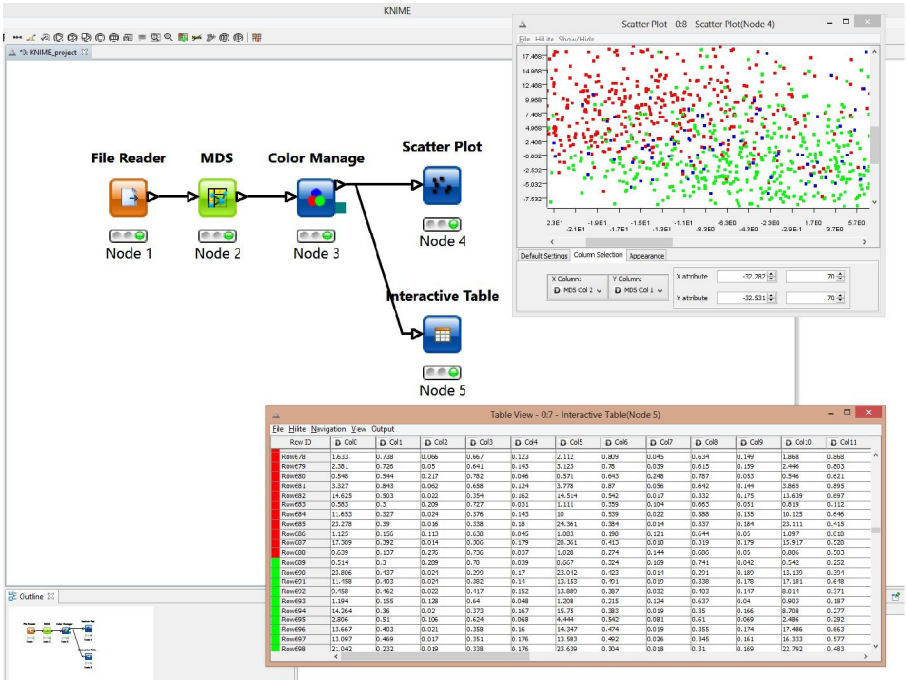

Figure 7.1: MDS pipeline build in KNIME

data points and the interactive table node displays the data in a table view.

The configuration of the MDS node is summarised in Table 7.1.

Property	MDS node
Epochs:	50 (default)
Output dimensions:	2
Learning rate:	1 (default)
Distance metric:	Euclidean

Table 7.1: Configuration of MDS the node

Chapter 8

Classifiers Used For Viability Determination

8.1 Support vector machine

8.1.1 Introduction

The fundamental idea with SVMs is to calculate the optimal separating hyperplane which separates two classes and maximizes the distance to the closest point from either class [Vap98]. Not only does this provide a unique solution to the separating hyperplane problem, but by maximizing the margin between the two classes on the training data leads to better classification performance on test data.

This section only briefly describes some of the fundamental aspects of SVMs. SVMs were first introduced by Vapnik et al. to solve pattern recognition and regression estimation problems [Vap98]. A detailed introduction to SVMs can be found in [Vap98].

8.1.2 Mathematical description of support vector machines

In what follows, we denote the N training samples as

$$Set = \{(\mathbf{x}_1, y_1 = f(\mathbf{x}_1)), (\mathbf{x}_2, y_2 = f(\mathbf{x}_2)), ..., (\mathbf{x}_N, y_N = f(\mathbf{x}_N))\}, \tag{8.1}$$

where $\mathbf{x}_i \in \mathbb{R}^p, i = 1, 2, ..., N$ denotes the $p-$dim feature vector and $y_i \in \{-1, +1\}, i = 1, 2, ..., N$ denotes the class number.

In the linearly separable case shown in Figure 8.1a (hard margin case), the SVM classifier

follows the intuitive choice and selects the hyperplane (among many that can separate the two classes) that maximizes the margin, where the margin is defined as the sum of the distances of the hyperplane to the closest points of the two classes.

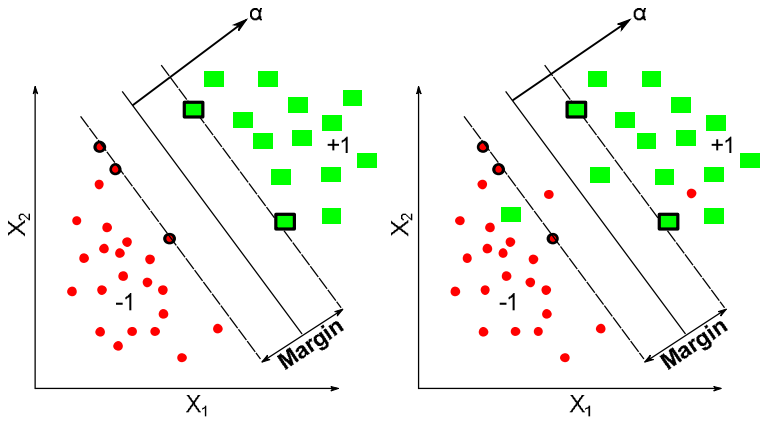

(a) Hard Margin Case (b) Soft Margin Case

Figure 8.1: Illustration of SVM classification. The support vectors are encircled.

In the case where the two classes are non-separable shown in Figure 8.1b (soft margin case), positive slack variables are introduced to allow some training samples to fall on the wrong side of the separating hyperplane. The SVM then finds the hyperplane that maximizes the margin and, at the same time, minimizes a quantity proportional to the number of classification errors. The trade-off between maximizing the margin and minimizing the error is controlled by a user-adjusted regularization parameter $C > 0$. A large C corresponds to a high penalty for classification errors.

Linear decision boundaries, like the ones in Figure 8.1 in its most basic form have serious limitations: non-linearly separable data cannot be classified and noisy data causes problems in finding unique hyperplanes. However, in many practical cases, non-linear decision surfaces are needed. Non-linear SVMs can be generalised from linear SVMs by selecting a feature transform $\varphi : \mathbb{R}^p \rightarrow \mathbb{R}^D$ to map the original feature vector $\mathbf{x}_i$ into a higher dimensional Euclidean space such that the resulting features $\varphi(\mathbf{x}_i), i = 1, 2, ..., N$ are linearly separable. These feature transforms can be easily incorporated into SVMs and the decision boundary has the form:

$$f(\mathbf{x}) = \boldsymbol{\alpha}^T \varphi(\mathbf{x}) + \alpha_0. \tag{8.2}$$

Mathematically it can be shown that the solution of the decision boundary in the non-linear case is:

$$f(\mathbf{x}) = \sum_i \lambda_i y_i \cdot \langle \varphi(\mathbf{x}_i), \varphi(\mathbf{x}) \rangle + \alpha_0 = \sum_i \lambda_i y_i \cdot ker(\mathbf{x}_i, \mathbf{x}) + \alpha_0, \tag{8.3}$$

where the coefficients λ_i are the solution of the following convex QP problem:

$$\text{maximize} \qquad -\frac{1}{2} \sum_i \sum_j \lambda_i \lambda_j y_i y_j \cdot \langle \varphi(\mathbf{x}_i), \varphi(\mathbf{x}) \rangle + \sum_i \lambda_i \tag{8.4}$$

$$\text{subject to} \qquad 0 \leqslant \lambda_i \leqslant C, \qquad \text{and} \qquad \sum_i \lambda_i y_i = 0, \tag{8.5}$$

where the function $ker(\cdot, \cdot)$ is called a kernel function and defined as:

$$ker(\mathbf{x}, \mathbf{x}') = \langle \varphi(\mathbf{x}), \varphi(\mathbf{x}') \rangle \tag{8.6}$$

for any feature mapping φ. Usually the evaluation of the kernel function is much simpler than the computation of transformed features followed by the inner product.

Typical kernel functions are:

$$\text{Linear} \qquad ker(\mathbf{x}, \mathbf{x}') = \langle \mathbf{x}, \mathbf{x}' \rangle \tag{8.7}$$

$$\text{Polynimial} \qquad ker(\mathbf{x}, \mathbf{x}') = \left(\langle \mathbf{x}, \mathbf{x}' \rangle + 1 \right)^k \tag{8.8}$$

$$\text{Radial basis function} \qquad ker(\mathbf{x}, \mathbf{x}') = e^{-\gamma \|\mathbf{x} - \mathbf{x}'\|_2^2} \tag{8.9}$$

$$\text{Sigmoid kernel} \qquad ker(\mathbf{x}, \mathbf{x}') = \tanh\left(\alpha \langle \mathbf{x}, \mathbf{x}' \rangle + \beta \right) \tag{8.10}$$

In a typical problem, the λ_i coefficients of only a few training samples will be non-zero. Thus, all $\mathbf{x_i}$'s with $\lambda_i > 0$ are elements on the boundary of the margin. These samples are referred to as the support vectors. Let $\mathbf{v_j}$ denote the aforementioned support vectors and λ_j^*, $j = 1, 2, ..., l$ $(l < N)$ their corresponding non-zero coefficients. The decision function in (8.3) can be rewritten in the s̈parseẗform of the support vectors as:

$$f(\mathbf{x}) = \sum_j \lambda_j^* y_j \cdot \langle \varphi(\mathbf{v}_j), \varphi(\mathbf{x}) \rangle + \alpha_0 = \sum_j \lambda_j^* y_j \cdot ker(\mathbf{v}_j, \mathbf{x}) + \alpha_0. \tag{8.11}$$

This equation shows that the decision boundary is a linear combination of the support vectors, which is typically a small fraction of the whole training set.

8.1.3 Software implementation

Two SVM classifiers were trained with the freely available library for SVMs called LIBSVM [Cha11], which was compiled as a dynamic link library for MATLAB.

The two SVM classifiers were configures as follow:

Property	SVM 1	SVM 2
Type of SVM:	C-SVC	C-SVC
Kernel type:	Linear	Radial basis function
Cost (C):	$weight_1 \times 50$	$weight_2 \times 50$
Other:	—	$\gamma = 1/Total\ number\ of\ features$ (default)

Table 8.1: Configuration of the SVM classifiers in LIBSVM

The variables $weight_1$ and $weight_2$ in Table 8.1 are the weights associated with each class of the data. These variables are used to set the cost parameter C_i of class i to $weight_i \times C$. Thus, the cost associated with a misclassification is adjusted to take into account unbalanced classes, that is in the case where $class_1$ and $class_2$ have an uneven number of observations. The weights are calculated as follow:

$$weight_i = \frac{\text{Total number of observations}}{\text{Number of observations in class } i} \tag{8.12}$$

By calculating and applying $weight_1$ and $weight_2$, means that the cost parameters C_1 and C_2 of the SVM are chosen such that the ratio in Equation 8.13 is obeyed [Mor99].

$$\frac{C_1}{C_2} = \frac{\text{Number of observations that belong to class 2}}{\text{Number of observations that belong to class 1}} \tag{8.13}$$

A small value for the penalty parameter C leads to an increase in the number of training errors, while a large value for C C lead to a behaviour similar to that of a hard-margin SVM. There exist various approaches and optimisation algorithms dedicated to finding the optimal value for the penalty parameter C [Hsu03] [Lon06] [Has01]. However, in this implementation the value for the penalty parameter C was determined by experimenting with several values and choosing the one that yielded the best classification performance for the training set.

8.2 Tree-based classifier

8.2.1 Introduction

Tree-based methods partition the feature space into a set of rectangles, and then models each region by a constant outcome. In this section a popular tree-based method called classification and regression tree (CART) by Breiman et al. [Bre83] is described.

Assume the outcome is $y \in \{1, 2, ..., K\}$. A classification tree repeatedly partitions the feature space into a set of rectangles by recursive binary splitting. First, the original feature space is split into two regions and the response is modelled by the majority vote of y in each region. Subsequently, one or both of these regions are split into two more regions. This process is continued until some stopping criteria is reached. At each step, the variable and split-point that achieves the best fit need to be determined. The aforementioned process is illustrated by the following example: four splits $x_1 = t_1, x_2 = t_2, x_1 = t_3, x_2 = t_4$ to partition the features space into five regions $Region_1, Region_2, Region_3, Region_4, Region_5$ shown in Figure 8.2a.

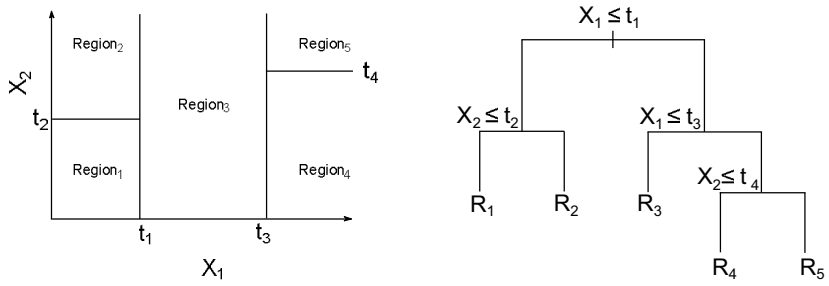

(a) An example partitioning of a two-dimensional feature space by recursive binary splitting.

(b) The tree corresponding to the two-dimensional partitioning.

Figure 8.2: Illustration of a feature space partitioned by a single tree.

The full dataset sits at the top node of the tree. Observations satisfying the conditions at each junction are assigned to the left branch, and the others to the right branch. The terminal nodes of the tree correspond to the regions $Region_1, Region_2, Region_3, Region_4, Region_5$ (see Fig. 8.2b).

A key advantage of the recursive binary tree is its interpretability. The feature space partition is fully described by a single tree as seen in Figure 8.2b.

8.2.2 Mathematical description

We define a tree T as a collection of nodes (t) and splits (s). Let $|T|$ denote the number of terminal nodes in T. In what follows, we denote the N observations as

$$Set = \{(\mathbf{x}_1, y_1 = f(\mathbf{x}_1)), (\mathbf{x}_2, y_2 = f(\mathbf{x}_2)), ..., (\mathbf{x}_N, y_N = f(\mathbf{x}_N))\}, \tag{8.14}$$

where $\mathbf{x}_i \in \mathbb{R}^p$ denotes the $p-$dim feature vector and $y_i \in \{1, 2, ..., K\}$ denotes the class number.

The tree-based algorithm needs to automatically decide on the splitting variables and split points, and also what topology the tree should have. Three processes are necessary to grow a tree, namely a splitting, a partitioning, and a pruning process.

The split process involves choosing split variables and split points and then applying the goodness of split criterion $\vartheta(s,t)$ to evaluate any split s of any node t. Each split depends on the values of only one *unique* variable x_u. For the splitting variable u and split point s, define the pair of half-planes

$$Region_1(u,s) = \{\mathbf{x}|x_u \leqslant s\}, \text{ and } \quad Region_2(u,s) = \{\mathbf{x}|x_u > s\}. \tag{8.15}$$

Each split produces two sub-nodes. The tree-based algorithm scans through all the inputs and all the possible splits to determine the best pair (u,s) yielding the most "pure" nodes, i.e., finding the splitting variable u and split point s that solve

$$\min_{u,s}[\vartheta_{Region_1} + \vartheta_{Region_2}], \tag{8.16}$$

where ϑ_{Region_m} is some purity measure of node $Region_m$ for $m = 1, 2$. A node is more pure if one class dominates the node than if multiple classes equally present in the node.

In a node m, representing a region $Region_m$ with N_m observations, let

$$\hat{p}_{mk} = \Pr(k|m) = \frac{1}{N_m} \sum_{\mathbf{x}_i \in Region_m} I(y_i = k), \tag{8.17}$$

which is the proportion of class k observations in node m. An observation in node m is assigned to class

$$k(m) = \arg\max_k \hat{p}_{mk}, \tag{8.18}$$

by the majority class in node m. Different measures $\vartheta_m(T)$ of node impurity include the follow-

ing:

$$\text{Misclassification error:} \quad \vartheta = \frac{1}{N_m} \sum_{i \in Region_m} I(y_i \neq k(m)), = 1 - \hat{p}_{mk(m)}. \tag{8.19}$$

$$\text{Gini index:} \quad \vartheta = \sum_{k=1}^{K} \hat{p}_{mk}(1 - \hat{p}_{mk}). \tag{8.20}$$

$$\text{Cross - entropy:} \quad \vartheta = -\sum_{k=1}^{K} \hat{p}_{mk} \log \hat{p}_{mk}. \tag{8.21}$$

All three impurity measures are similar, but cross-entropy and the Gini index are differentiable, and hence more amenable to numerical optimization.

The binary partitioning process of the feature space is recursively repeated until the tree is large enough. A very large tree might overfit the data and a small tree might not capture the important structure. Hence, the optimal tree size should be adaptively chosen from the data. The preferred approach is to grow a large tree T_0, stopping the splitting process only when some minimum node size (say 5) is reached.

The *weakest link pruning* procedure successively collapse the internal node that produces the smallest per-node increase in $\sum_m N_m \vartheta_m(T)$, and continue until a single node tree is produced. This gives a finite sequence of sub-trees. The *cost-complexity* for each sub-tree T is measured by

$$CC_\alpha(T) = \sum_{m=1}^{|T|} N_m \vartheta_m + \alpha |T|, \tag{8.22}$$

where m's run over all the terminal nodes in T, and α governs a trade-off between the tree size $|T|$ and its goodness of fit to the data. A large α results in smaller trees; a small α results in large trees. Breiman et al. ([Bre]) have shown that for each α, there is a unique smallest sub-tree T_α that minimizes $CC_\alpha(T)$. Furthermore, the sequence of sub-trees obtained by pruning under the *weakest link pruning* procedure, must contain T_α. Though, in practice five- to ten-fold cross validation is used to estimate α.

CART classification uses the *Gini index* as node impurity criterion. Instead of employing stopping rules, CART generates a sequence of sub-trees by growing a large tree and pruning it back until only the root node is left. Then it uses cross-validation to estimate the misclassification cost of each sub-tree and chooses the one with the lowest estimated cost.

8.2.3 Software implementation

The tree-based classifier was trained by means of the *Classregtree* function in the Statistics Toolbox of Matlab. The *Classregtree* function was configured as follow:

- Number of features per split: all features
- Pruning: "on" (default)
- Node impurity criteria for choosing split: Gini index

8.3 Random forests

8.3.1 Introduction

The random forest (RF) algorithm was introduced by Breinman ([Bre01]) as a modification of bagging that builds a large ensemble of de-correlated trees, and then classifies using a majority vote. RF are very popular, because they can cope with high-dimensional data, their performance on a variety of problems are better than boosting, they are simple to train, and requires very little tuning [Has01] [Has01]. Furthermore, RFs can cope with complex interaction structures as well as highly correlated variables [Bou12]. The aforementioned properties make RFs an ideal choice as a classifier in this thesis.

This section briefly describes the basic functioning of RF. Theoretical details and reviews covering other aspects of RFs can be found in [Bre01], [Has01],[Dud12],[Bou12].

8.3.2 Mathematical description of random forests

The general functioning of the RF algorithm is depicted in Figure 8.3. In RFs, each CART tree in the ensemble is built from a sample drawn with replacement (i.e., a bootstrap sample) from the original data set. In addition, when splitting a node during the construction of the tree, the split that is chosen is no longer the best split among all features. Instead, at each tree split a random sample of q features is drawn and only those q features are considered for splitting. Typically $q = \sqrt{p}$ or $\log_2 p$, where p is the number of features [Has01]. The predictions of all trees are finally aggregated through majority voting.

The random sampling of the features usually leads to an increase in the bias of the forest with respect to the bias of a single non-random tree. However, due to the averaging of the predictions,

the RF's variance decreases. Thus, the decrease in the variance compensates for the increase in bias, hence yielding an overall better model.

An important feature of a RF is its out-of-bag (OOB) error. For each tree grown on a bootstrap sample, the error rate for observations left out of the bootstrap sample is monitored. This is called the OOB error rate. An OOB error estimate is almost identical to that obtained by N-fold cross validation. Through this internal validation, the error estimation is less optimistic and usually considered as a good estimator of the error expected for independent data. Once the OOB error stabilises, the training can be terminated [Has01].

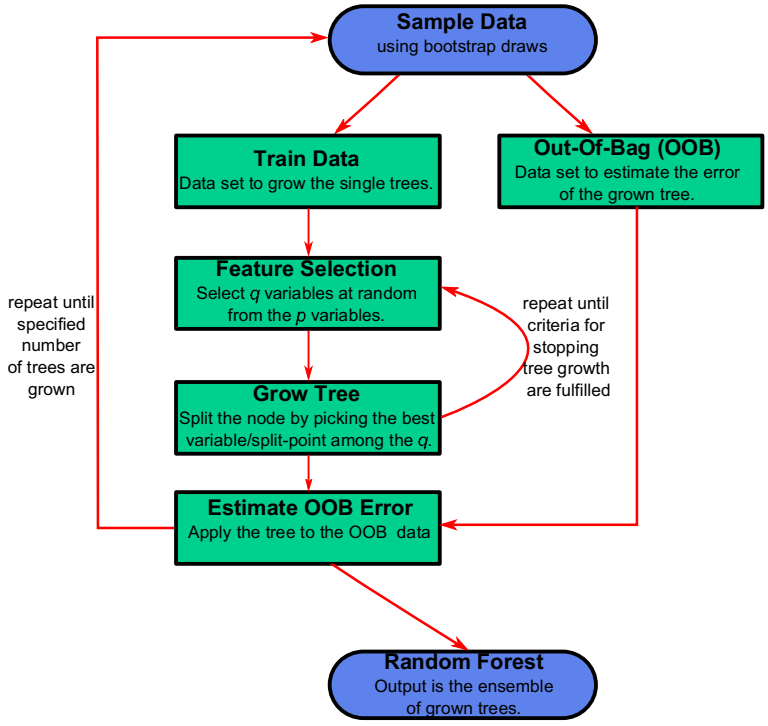

Figure 8.3: Random forest algorithm

8.3.3 Software implementation

The RF classifier was trained by means of the *Treebagger* function in the Statistics Toolbox of Matlab. The *Treebagger* function was configured as follows:

- Number of Trees: 80
- Number of features per split: $\sqrt{number\ of\ features}$
- Pruning: "on" (default)
- Node impurity criteria for choosing split: Gini index

The OOB classification error versus the number of trees in the RF is illustrated in Figure 8.4. The larger the number of trees in the RF, the smaller the OOB classification error. However, to grow a large number of trees is computationally expensive. Thus, the number of trees grown for each RF classifier were chosen to be 80, this is the number of trees that yield acceptable classification performance while limiting the time necessary to train the RF.

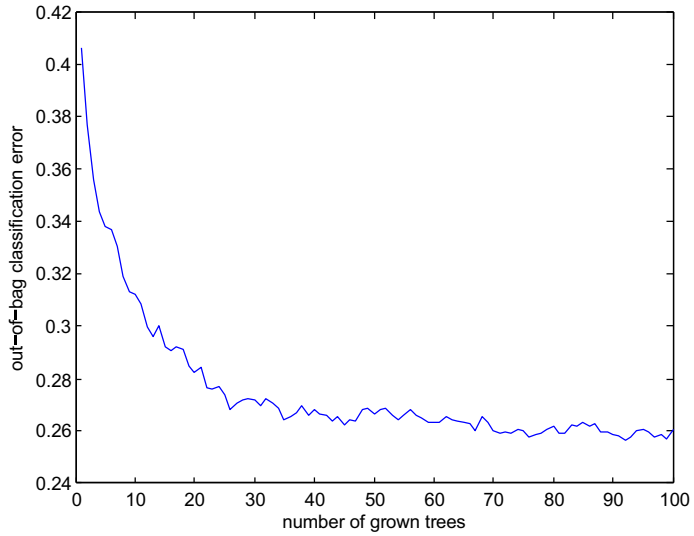

Figure 8.4: OOB classification error curve used to determine the appropriate number of trees to be grown in the RF.

Chapter 9

Results Of The Study

9.1 Introduction

In this chapter the classification rate, under practical conditions, of the cell viability determination method is presented. Only one micrograph was used for the training of the classifiers. The remaining six micrographs were used for testing the cell viability determination method. Hence, 7-fold cross-validation was used to produce the results for this thesis (see Appendix B for details).

The tree-based classifier produced inferior classification rates compared to both the SVM classifiers and the RF classifier. Therefore, the classification rate tabulated in the subsequent sections for each feature set was obtained by calculating the average classification rate for the SVM with a linear kernel, the SVM with a radial basis function kernel and the RF classifier.

9.2 Method for keypoint detection and labelling

The steps followed for detecting and labelling keypoints associated with the cells in the acquired micrographs are summarised as follows:

- Step 1: The cells in the acquired micrographs were manually detected and labelled as viable-adherent, viable-suspended, or non-viable as illustrated in Figure 9.1. Multiple points within each cell were manually selected, in order to ensure that every manually labelled cell has a keypoint associated with it. The number of manually selected points for each cell class in the seven micrographs are summarised in Table 9.1.

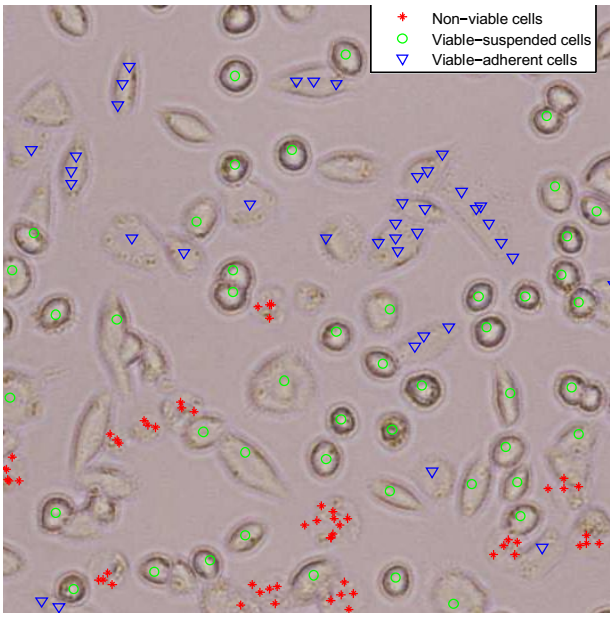

Figure 9.1: Manual selection of multiple points within the cells in a bright-field micrograph.

- Step 2: The SIFT algorithm was used to detect points-of-interest in the micrographs as shown in Figure 9.2. These points-of-interest are referred to as SIFT keypoints.

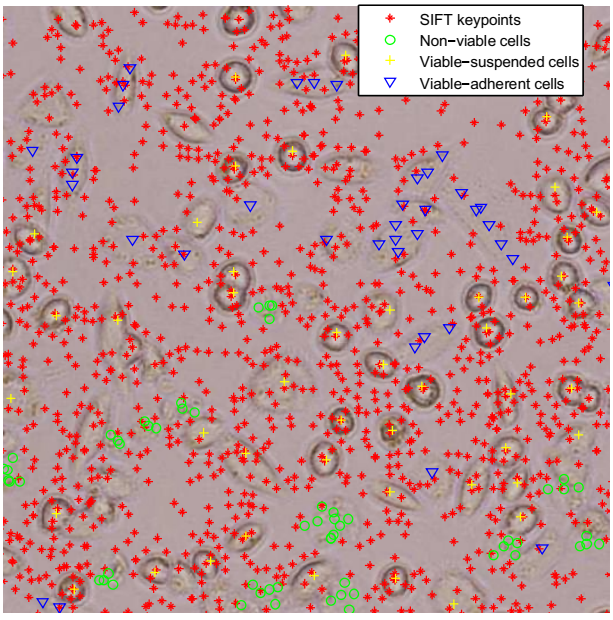

Figure 9.2: Calculated SIFT keypoints for a bright-field micrograph.

- Step 3: Only the SIFT keypoints that occur in a 11×11 neighbourhood of a manually selected point are kept. The label of the manually selected point is then assigned to the

keypoints that fall within the 11×11 neighbourhood. The size of the neighbourhood was chosen by visual inspection of the micrographs to make sure that the keypoints fell either within a cell or on the border of the cell thus preventing the inclusion of keypoints associated with the background. The number of keypoints for each microscope modality in each of the seven micrographs are summarised in Table 9.2, 9.3, 9.4 and 9.5.

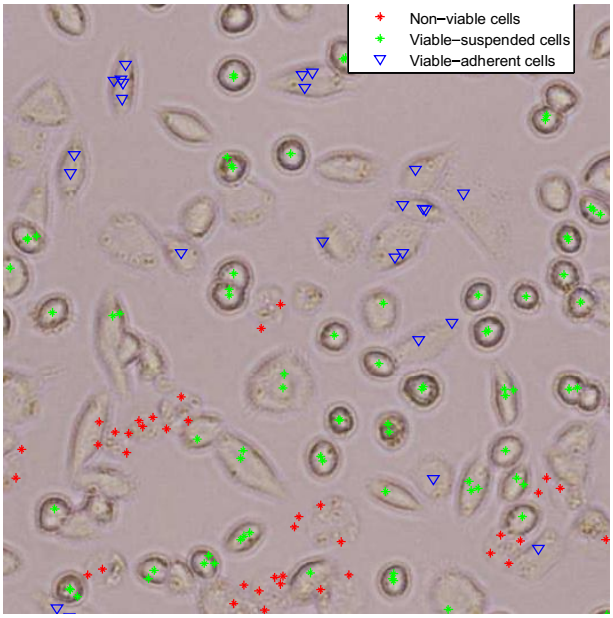

Figure 9.3: Illustration of the labelled cell keypoints after consolidating the manually selected points and the SIFT keypoints.

	Non-viable	Viable suspension	Viable adherent
Micrograph 1	887	844	757
Micrograph 2	466	449	524
Micrograph 3	496	417	585
Micrograph 4	786	563	450
Micrograph 5	531	516	576
Micrograph 6	435	340	523
Micrograph 7	498	418	574

Table 9.1: The number of manually selected cell in each micrograph.

	Non-viable	Viable suspension	Viable adherent
Bright-field 1	786	1200	521
Bright-field 2	517	554	500
Bright-field 3	581	598	519
Bright-field 4	774	848	264
Bright-field 5	820	771	625
Bright-field 6	687	538	660
Bright-field 7	549	594	471

Table 9.2: The number of keypoints per cell type in each bright-field micrograph.

	Non-viable	Viable suspension	Viable adherent
Phase contrast 1	1492	1202	854
Phase contrast 2	731	817	497
Phase contrast 3	1026	881	834
Phase contrast 4	2021	891	536
Phase contrast 5	1517	788	664
Phase contrast 6	1167	585	527
Phase contrast 7	1344	577	638

Table 9.3: The number of keypoints per cell type in each phase contrast micrograph.

	Non-viable	Viable suspension	Viable adherent
Negative-focused bright-field 1	1028	1077	581
Negative-focused bright-field 2	820	745	603
Negative-focused bright-field 3	682	612	460
Negative-focused bright-field 4	1018	732	469
Negative-focused bright-field 5	892	725	507
Negative-focused bright-field 6	946	589	645
Negative-focused bright-field 7	712	607	500

Table 9.4: The number of keypoints per cell type in each negatively-defocused bright-field micrograph.

	Non-viable	Viable suspension	Viable adherent
Positive-focused bright-field 1	632	1388	624
Positive-focused bright-field 2	344	677	267
Positive-focused bright-field 3	407	762	516
Positive-focused bright-field 4	1103	1053	530
Positive-focused bright-field 5	616	944	481
Positive-focused bright-field 6	453	561	301
Positive-focused bright-field 7	461	773	559

Table 9.5: The number of keypoints per cell type in each positively-defocused bright-field micrograph.

9.3 Feature visualisation by means of MDS

The two dimensional projection of the features extracted from a bright-field micrograph are displayed in Table 9.6. The first hundred samples from each class were used for the projection and visualisation of the extracted features.

The SIFT descriptors are distributed across 2D plane and the different cell classes do overlap. It is particularly evident that the SIFT features are not able to discriminate well between non-viable and viable-adherent cells. The phenomenon of the two global clusters that are visible in the image was investigated and it turns out that the two global clusters are associated with keypoints that are either located in an area with generally high intensity values or in an area where the average intensity values are low.

From the projected images it is clear that the ray features, the variance map and the DOG as well as PCR features do not offer any discriminative information that might aid in cell viability determination. All the samples from the three different classes are projected on top of each other.

The static pixel patch and the intensity stencil do provide discriminative information for distinguishing between viable-suspended and both non-viable and viable-adherent. However, both sets of features has a hard time in separating the non-viable class from the viable-adherent class.

The projections of the grey-scale texture features all look alike. Once more these features have a hard time in separating the non-viable cell class from the viable-adherent cell class. However, it can be noted that a lower number of quantisation levels actually have more discriminative power than grey-scale texture features calculated from a co-occurrence matrix that was constructed using the same number of quantisation bits as the image itself.

Lastly, the features that are best able to separate the three classes of cells are the colour texture features. From their projection images it is evident that these features are able to distinguish between non-viable, viable-suspended and viable-adherent. Once again, the lower the number of quantisation levels the more separable the cells classes appear in the projection images.

Based on this preliminary screening of the features, it can be predicted that the highest classification rate will be achieved by the colour texture features.

Features	MDS 2D-projection
SIFT	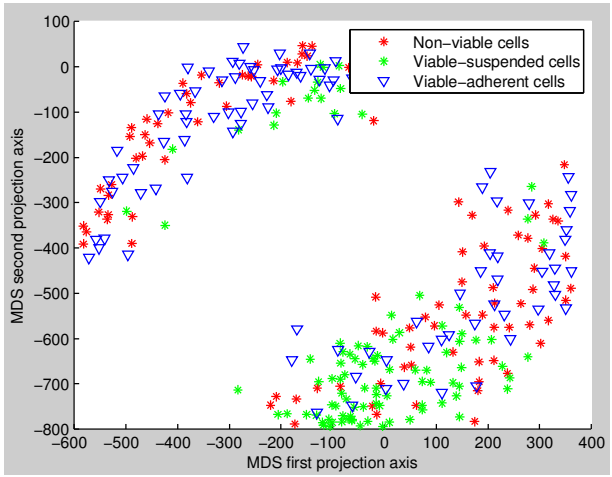
Ray	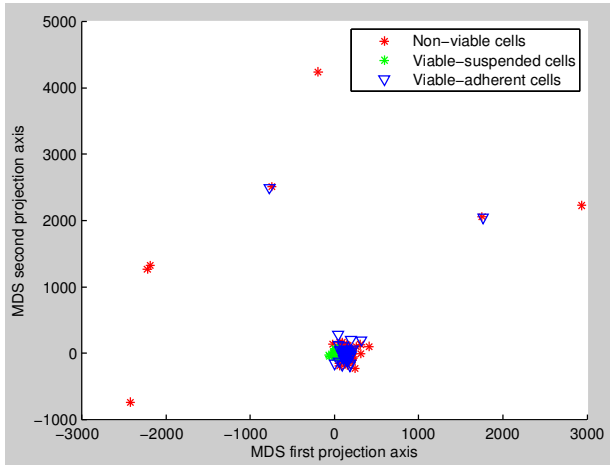
Stencil	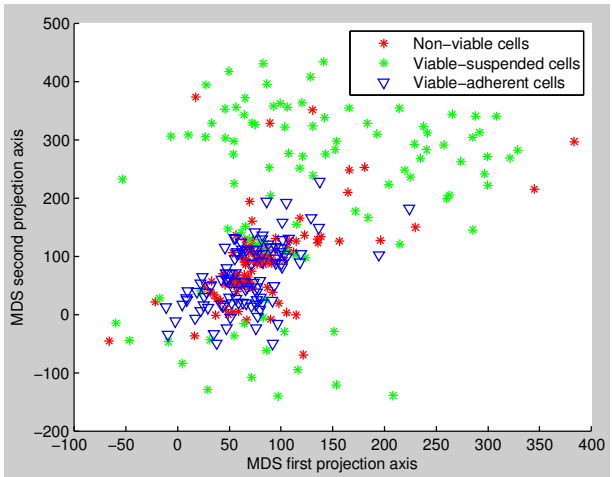

Features	MDS 2D-projection
Vmap	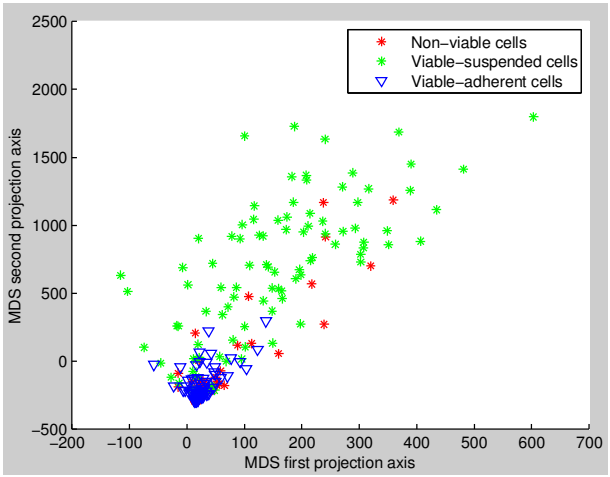
DOG and PCR	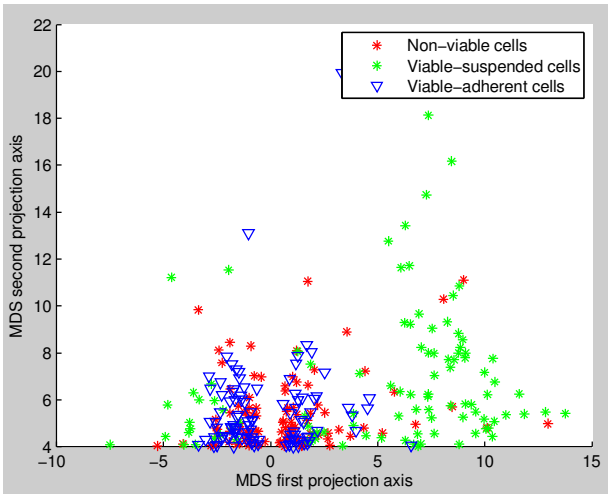
Pixel patch	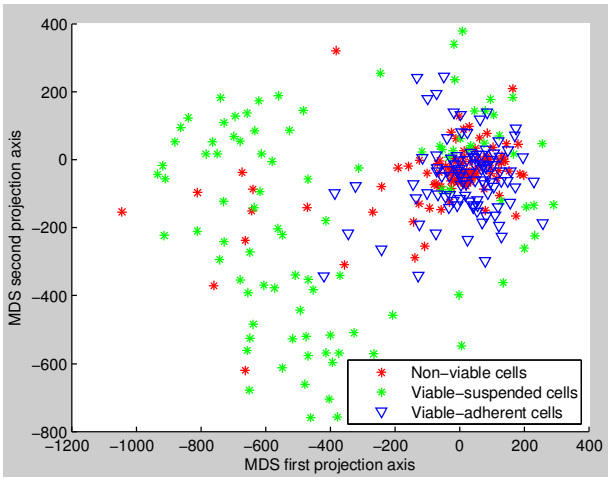

Features	MDS 2D-projection
GTex16	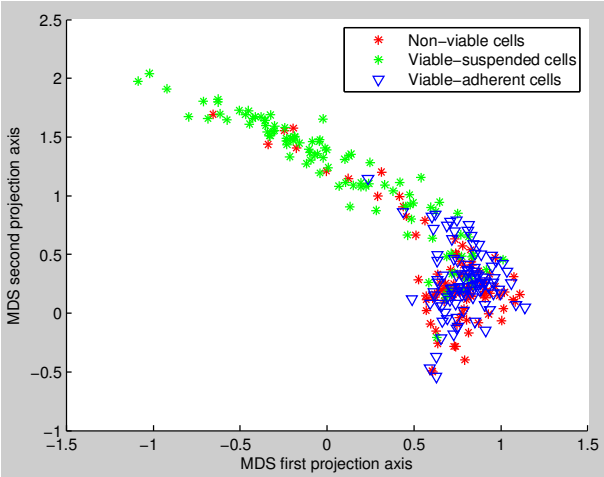
GTex32	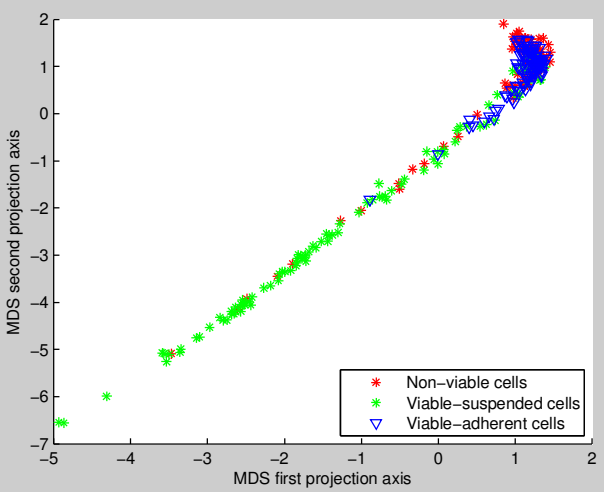
GTex64	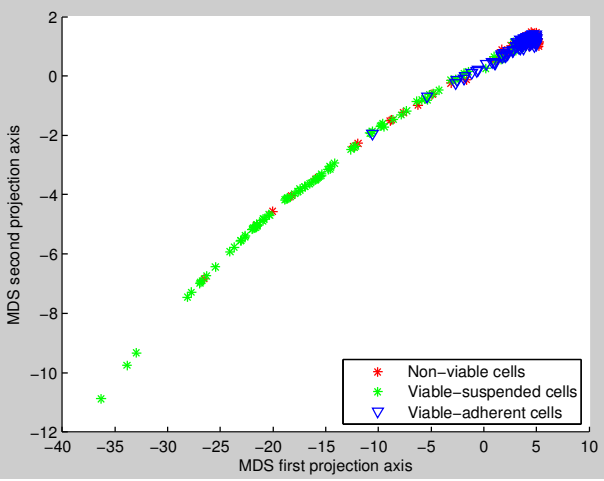

Features	MDS 2D-projection
GTex128	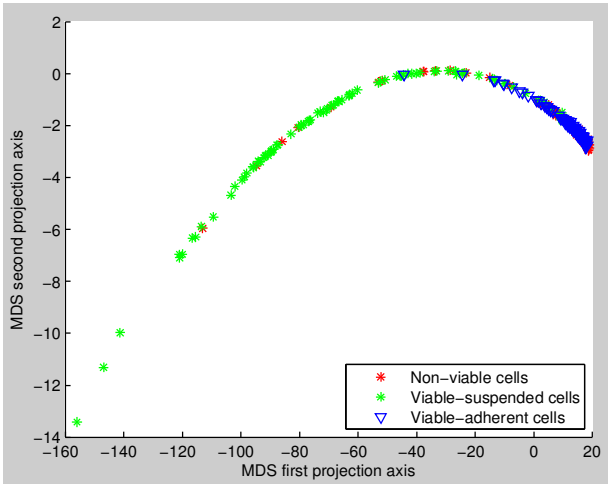
GTex256	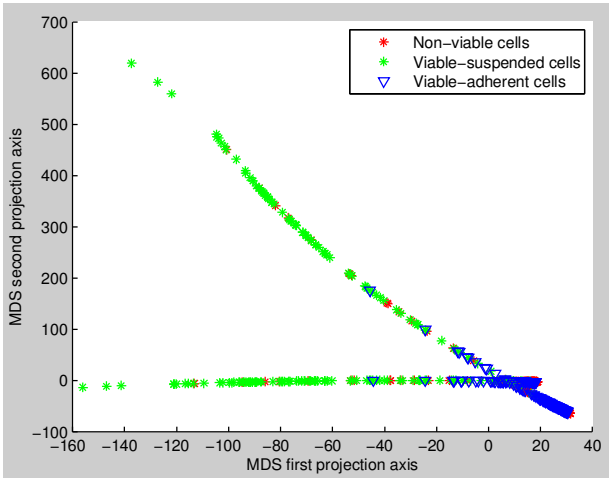
CTex16	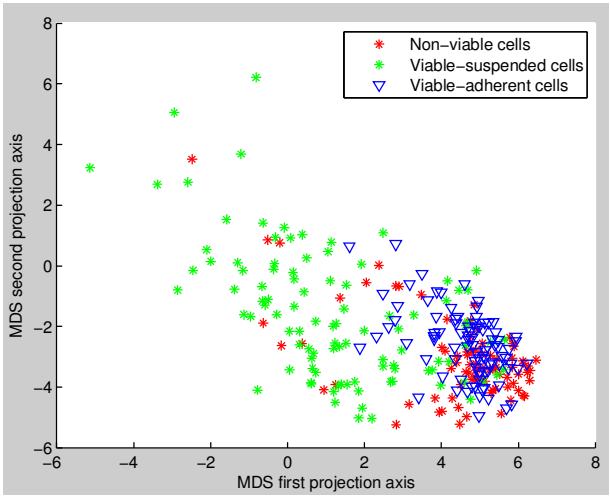

Features	MDS 2D-projection
CTex32	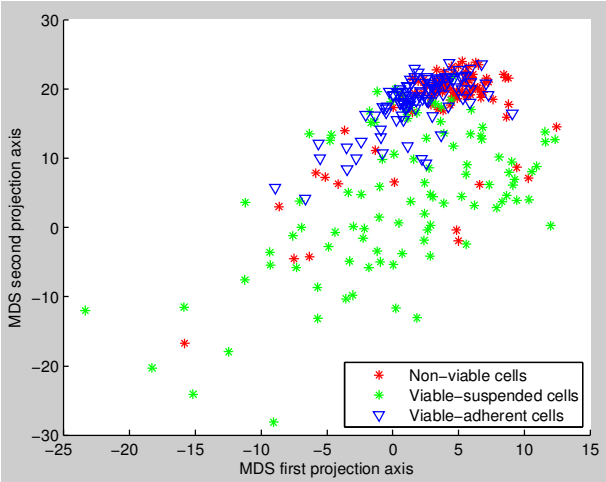
CTex64	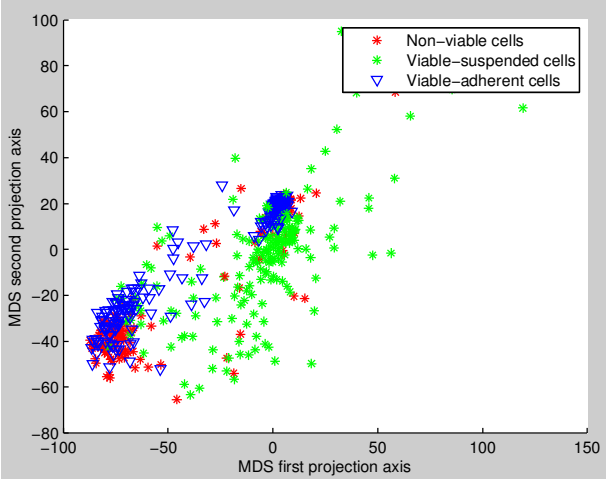
CTex128	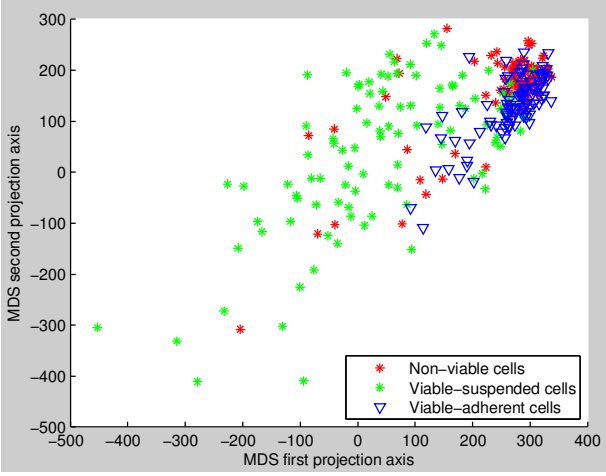

Features	MDS 2D-projection
CTex256	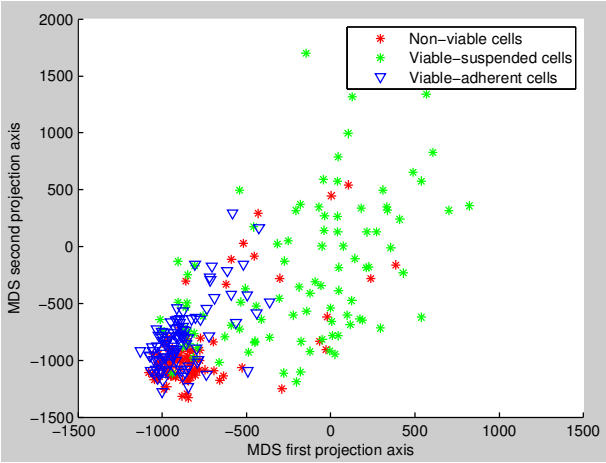

Table 9.6: The 2D visualisation of the extracted features after MDS was applied.

9.4 Feature ranking according to classification rate

The features that had the highest classification rate are ranked for each microscope modality in Table 9.7, Table 9.8,Table 9.9, Table 9.10.

From the investigation it is evident that in general the features which ranked most frequently in the top 5 were calculated from a patch with a dynamically changing size. The most discriminative features are the intensity stencil, the variance map, the colour texture features quantised with 32 levels, the static pixel patch and the SIFT descriptors.

This section can be concluded by stating that there is no one feature that is superior in distinguishing non-viable from either viable-suspended or viable-adherent cells. Even more so, there is no guarantee that the features ranked here are able to perform cell viability determination when different cell-line/toxin combinations are considered. It might happen that a completely different set of features rank in the top 5 for discrimination power.

	Non-viable vs. viable-suspended		Non-viable vs. viable-adherent	
Rank	Classification rate (%)	Feature	Classification rate (%)	Feature
1	$86,82 \pm 2,52$	Dynamic Stencil	$66,30 \pm 0,87$	Static CTex32
2	$85,35 \pm 1,45$	Dynamic Vmap	$66,22 \pm 1,51$	Static CTex16
3	$83,51 \pm 1,41$	Dynamic CTex32	$65,38 \pm 0,75$	Dynamic CTex32
4	$82,99 \pm 2,86$	Dynamic CTex64	$65,17 \pm 1,24$	Dynamic SIFT
5	$82,92 \pm 1,92$	Static Pixel patch	$64,04 \pm 1,94$	Static CTex64

Table 9.7: Ranked features according to classification rate for viability determination in bright-field micrographs.

	Non-viable vs. viable-suspended		Non-viable vs. viable-adherent	
Rank	Classification rate (%)	Feature	Classification rate (%)	Feature
1	$85,53 \pm 1,56$	Static CTex32	$66,81 \pm 3,06$	Dynamic SIFT
2	$84,75 \pm 0,25$	Static CTex16	$65,29 \pm 4,44$	Dynamic Stencil
3	$84,30 \pm 1,25$	Dynamic CTex32	$62,15 \pm 1,40$	Dynamic Vmap
4	$84,08 \pm 2,30$	Static Pixel patch	$61,20 \pm 7,37$	Dynamic CTex128
5	$82,80 \pm 0,51$	Dynamic CTex16	$60,94 \pm 4,17$	Static CTex32

Table 9.8: Ranked features according to classification rate for viability determination in phase contrast micrographs.

	Non-viable vs. viable-suspended		Non-viable vs. viable-adherent	
Rank	Classification rate (%)	Feature	Classification rate (%)	Feature
1	$87,07 \pm 2,11$	Dynamic Stencil	$66,73 \pm 2,75$	Dynamic SIFT
2	$84,77 \pm 1,25$	Dynamic Vmap	$64,78 \pm 1,84$	Dynamic CTex32
3	$84,21 \pm 1,24$	Dynamic CTex32	$64,67 \pm 2,16$	Static CTex32
4	$83,12 \pm 3,72$	Dynamic CTex64	$63,84 \pm 1,96$	Static CTex16
5	$82,58 \pm 1,22$	Dynamic SIFT descriptors	$63,78 \pm 2,94$	Static CTex128

Table 9.9: Ranked features according to classification rate for viability determination in negatively-defocused bright-field micrographs.

	Non-viable vs. viable-suspended		Non-viable vs. viable-adherent	
Rank	Classification rate (%)	Feature	Classification rate (%)	Feature
1	$87,06 \pm 1,48$	Dynamic Stencil	$66,87 \pm 1,18$	Static CTex32
2	$85,52 \pm 0,25$	Dynamic Vmap	$65,23 \pm 1,59$	Static CTex16
3	$81,27 \pm 0,79$	Dynamic SIFT descriptors	$65,18 \pm 3,41$	Static CTex64
4	$79,56 \pm 0,58$	Dynamic CTex32	$64,80 \pm 0,66$	Dynamic CTex32
5	$79,07 \pm 1,46$	Dynamic CTex16	$64,23 \pm 1,20$	Dynamic CTex16

Table 9.10: Ranked features according to classification rate for viability determination in positively-defocused bright-field micrographs.

9.5 Classification rate comparison between microscope modalities for dynamic and static sized patches

The best average classification rate achieved for each modality in this 7-fold cross-validation experiment is summarised in Table 9.11. Thus, the classification rates listed may be associated with different features.

From Table 9.11 it is evident that there is no microscope modality that is superior across all of the categories. For each category there is a different modality that yields the highest classification rate. Another observation that can be made from Table 9.11 is that phase contrast and defocused bright-field micrographs do not offer more discriminative power than standard bright-field micrographs. Thus contradicting the claims made by biologists and bioprocess engineers that these latter modalities are better suitable for unstained cell viability determination.

The classification rate for the four microscope modalities are almost identical for the case where a dynamic sized patch was used for calculating the features. However, the classification rate varies significantly across the modalities for the case where a static sized patch was used for calculating the features. Therefore, a dynamic patch yield more stable classification rates.

It can be concluded from Table 9.11 that a dynamically changing patch offer a bit more discriminative power than a static patch. However, the computational cost and time associated with using a dynamically changing patch size relative to the increase in classification rate, suggests that it might be more sensible to just use a static patch instead.

Modality	Dynamic Patch Size		Static Patch Size	
	Non-viable vs. viable-suspended	Non-viable vs. viable-adherent	Non-viable vs. viable-suspended	Non-viable vs. viable-adherent
	Classification rate (%)	Classification rate (%)	Classification rate (%)	Classification rate (%)
BF	$86,82 \pm 2,52$	$65,38 \pm 0,75$	$82,92 \pm 1,92$	$66,30 \pm 0,87$
PC	$84,30 \pm 1,25$	$66,81 \pm 3,06$	$85,53 \pm 1,56$	$61,13 \pm 6,04$
BFN	$87,07 \pm 2,11$	$66,73 \pm 2,75$	$79,56 \pm 0,54$	$64,67 \pm 2,16$
BFP	$87,06 \pm 1,48$	$64,80 \pm 0,66$	$78,27 \pm 0,43$	$66,87 \pm 1,18$

Table 9.11: A summary of the classification rates achieved by using different microscope modalities for dynamic and static sized patches.

9.6 Classification rate comparison between grey and colour features

Grey-scale texture features as well as colour texture features were calculated for each keypoint. The classification rate associated with the two feature sets for 5 different quantisation levels are summarised in Table 9.12.

The results in Table 9.12 confirms that there is definitely discriminative information embedded across the red, the green and the blue channel in colour micrographs. The colour texture features had on average a 5% higher classification rate than the grey-scale texture features.

Malpica et al. [Mal03] claim that texture features have shown to be reasonably invariant to grey-level quantisation. From the results in Table 9.12 the claim made by Malpica et al. is contradicted. Moreover, it is evident that both the grey-scale as well as the colour texture features are extremely sensitive to the number of quantisation levels. The colour texture features across all the quantisation levels outperform the grey-scale texture features based on classification rate when a static patch size is used. However, for the quantisation levels 128 and 256 in the dynamic patch size case, the grey-scale texture features actually yield better classification rates when distinguishing between non-viable and viable-suspended cells.

Texture feature	Dynamic Patch Size		Static Patch Size	
	Non-viable vs. viable-suspended	Non-viable vs. viable-adherent	Non-viable vs. viable-suspended	Non-viable vs. viable-adherent
	Classification rate (%)	Classification rate (%)	Classification rate (%)	Classification rate (%)
GTex16	$73,13\pm4,95$	$55,57\pm2,17$	$63,30\pm1,57$	$54,32\pm2,05$
CTex16	$81,26\pm1,68$	$62,68\pm2,34$	$80,22\pm3,12$	$63,86\pm2,67$
GTex32	$74,83\pm5,45$	$56,79\pm3,14$	$64,89\pm1,88$	$55,24\pm2,35$
CTex32	$82,90\pm2,25$	$63,88\pm2,23$	$81,19\pm3,17$	$64,70\pm2,67$
GTex64	$75,02\pm5,79$	$57,81\pm2,43$	$64,72\pm1,74$	$55,71\pm2,16$
CTex64	$81,56\pm2,37$	$62,65\pm2,59$	$79,48\pm2,79$	$63,33\pm2,09$
GTex128	$74,08\pm5,90$	$57,42\pm2,23$	$63,56\pm1,30$	$55,11\pm2,07$
CTex128	$74,85\pm2,40$	$62,18\pm1,38$	$73,81\pm1,70$	$62,65\pm1,30$
GTex256	$72,63\pm5,92$	$56,59\pm2,12$	$62,83\pm2,62$	$55,16\pm1,57$
CTex256	$70,47\pm2,20$	$59,32\pm1,40$	$67,78\pm2,00$	$60,40\pm0,85$

Table 9.12: A summary of the classification rates achieved for different quantisation levels of grey-scale and colour texture features.

9.7 Summary

The best feature/classifier combination for each modality and the associated classification rate is summarised in Table 9.13 for a dynamically changing patch and in Table 9.14 for a static patch. Thus, the classification rates listed are the true values achieved for each modality after 7-fold cross-validation.

For a dynamic patch size the intensity stencil feature set/SVM:RBF classifier combination resulted on average in the highest classification rate for distinguishing non-viable from viable-suspended cells. The fact that the SVM with a RBF kernel performed so well is an indication that the cell classes are well separable for the intensity stencil feature set in the suspended case. The SIFT descriptors/RF classifier combination proved on average superior for distinguishing non-viable from viable-adherent cells. The fact that the RF classifier yielded the best results is an indication that the cell classes defined by the SIFT descriptors are not well separated for the adherent case.

The static pixel patch feature set proved to be highly successful at distinguishing between

non-viable and viable-suspended cells. Moreover, the fact that SVM classifiers achieved on average the best classification rates confirm the discriminative power of pixel patches. Colour texture features calculated from a static sized patch was the dominating feature set able to distinguishing between non-viable and viable-adherent cells. Once again the SVM classifiers produced the highest classification rates in the latter case.

Concluding, there is no feature/classifier combination that dominates across all the scenarios. However, the intensity stencil and the static pixel patch feature sets are the two most suitable features to distinguish between non-viable and viable-suspended cells. The SIFT and the colour texture feature sets are best able to discriminate between non-viable and viable-adherent cells.

Dynamic Patch Size						
	Non-viable and Viable Suspension			Non-viable and Viable Adherent		
	Classification rate (%)	Feature	Classifier type	Classification rate (%)	Feature	Classifier type
BF	$88,28 \pm 1.34$	Stencil	SVM: RBF	$67,68 \pm 2,37$	CTex128	SVM: Linear
PC	$85,77 \pm 1,68$	CTex128	RF	$70,33 \pm 1,29$	SIFT	RF
BFN	$88,40 \pm 0,65$	Stencil	SVM: RBF	$69,90 \pm 1,07$	SIFT	RF
BFP	$88,11 \pm 0,40$	Stencil	SVM: RBF	$65,21 \pm 2,62$	CTex128	RF

Table 9.13: A summary of the feature/classifier combinations for a dynamic patch size that resulted in the best classification rate for viability determination in the different micrographs.

Static Patch Size						
	Non-viable and Viable Suspension			Non-viable and Viable Adherent		
	Classification rate (%)	Feature	Classifier type	Classification rate (%)	Feature	Classifier type
BF	$84,86 \pm 5.97$	Patch	SVM: RBF	$67,94 \pm 2,44$	CTex16	SVM: RBF
PC	$86,48 \pm 1,47$	CTex32	SVM: Linear	$66,22 \pm 1,28$	CTex256	SVM: RBF
BFN	$84,03 \pm 3,02$	Patch	SVM: RBF	$67,55 \pm 1,98$	CTex64	RF
BFP	$79,82 \pm 4,74$	Patch	RF	$67,80 \pm 2,42$	CTex64	SVM: Linear

Table 9.14: A summary of the feature/classifier combinations for a static patch size that resulted in the best classification rate for viability determination in the different micrographs.

Chapter 10

Summary And Outlook

10.1 Summary

A method for the automatic detection of unstained cells in light microscopy images has been described. The evaluation of the viability determination method is based on micrographs acquired from four different microscope settings. This evaluation enables the comparison between the modalities to determine which one of them is best suited for viability determination without viability stains.

According to the investigation, both viable-adherent and viable-suspended cells exhibit great morphological details and are intra-cellularly well organised. Furthermore, viable-adherent cells in culture exhibit a great diversity of shape and size, whereas viable-suspended cells appear smaller in size and more round in shape. In contrast, non-viable cells are not intra-cellularly organised and almost no morphological details can be observed in these cells. Furthermore, non-viable cells are round in appearance, barely visible in standard bright-field micrographs and display more homogeneous values throughout the cells. The fact that non-viable cells are barely visible in bright-field micrographs makes it very difficult to distinguish them from viable-adherent cells.

In this thesis various features were extracted to distinguish between viable and non-viable cells. The features that offered the most discriminative power were the intensity stencil, the SIFT descriptors, the static pixel patch and the colour texture features. Sadly, there was not feature set that was able to distinguish between non-viable and viable cells across all the scenarios investigated.

Focusing and micrograph acquisition were performed manually in the present study. Positively-defocused and negatively-defocused bright-field micrographs were acquired to study the influ-

ence of defocusing on the discriminative power of the keypoint-based cell viability determination method. The investigation found that the defocused micrographs on average do not offer more discriminative power than focused bright-field micrographs. The latter result is also true for phase contrast micrographs.

The discriminative power of grey-scale and colour texture features for cell viability determination were also investigated. The colour texture features proved to be the most successful of all the features at distinguishing non-viable from viable-adherent cells across all the microscope modalities. Thus, it can be concluded that there is indeed discriminative information embedded in colour micrographs. Additionally, the effect of using different quantisation levels for calculating the texture features were also investigated. The investigation found that the classification performance is indeed sensitive to the number of quantisation levels used for calculating the texture feature. However, there is no one quantisation level that proved superior amongst all the possible quantisation levels.

In this thesis two pixel patches with different patch sizes were extracted from each keypoint. The one pixel patch had a size equal to the average keypoint scale in the micrograph and the other patch had a size equal to the keypoint scale of that particular keypoint. The effect of a dynamic patch size as opposed to a static patch size on the discriminative power of the features extracted for cell viability determination was investigated. The investigation found that using the average keypoint scale as pixel patch size actually yields classification rates similar to dynamic patches and is computationally less expensive.

To conclude, an effective method for cell viability determination has been proposed and successfully applied to identify unstained viable and non-viable cells in bright-field micrographs of CHO cell cultures in which cell death was induced by the toxin sodium azide.

10.2 Outlook

In the developed keypoint-based cell viability determination framework the discriminative power of the individual features were explored. However, a benchmark for the classification rate was not established. Therefore, all the features should be used simultaneously in the keypoint-based cell viability framework to establish the best possible classification rate achievable. Henceforth, the discriminative power of all the features can be compared against this benchmark classification rate.

The cell viability determination method has proven successful for keypoint-based cell detection. However, the SIFT algorithm is patented. Therefore, the method should be adapted to a

cell-based viability determination method. Thus, classifying a cell based on one hit-point in the cell and not multiple SIFT keypoints.

Biological cells exhibit different morphological changes when exposed to different toxins. Therefore, the developed viability determination method could be used to investigate which features are best suited to distinguish between viable and non-viable cells for different cell-line/toxin combinations.

Cell sizes and appearances may differ significantly over the course of a cell culture's evolution. The changes in appearance over time prompt the development of a method that is able to successfully detect, monitor and quantify non-viable cells in culture from a time-series of micrographs. Thus, it should be investigated if the features that are able to distinguish between viable and non-viable cells at an early stage of the cell culture's evolution have the same discriminative power at a later stage of the cell culture's evolution.

Colour texture features have proven to be the most successful, compared to the other features extracted, at distinguishing between non-viable and viable-adherent cells. It would be worthwhile to investigate what effect it would have on their discriminative power if the co-occurrence matrix were to be calculated in a different manner. Thus, not only considering the occurrence of pixel values that are separated by one pixel, but by two, three or even more pixels.

Another possibility emanating form this study, is the development of a method that is able to distinguish between viable, non-viable and apoptotic cells. Thus, a method that is able to detect and classify healthy, dying and dead cells in a cell culture.

10.3 Acknowledgements

I would like to thank Björn Sommerfeldt and Hannes Engelhardt from the Institute of Bioprocess Engineering at the University Erlangen-Nuremberg. They unselfishly prepared the cell cultures that were used in this thesis. The micrographs obtained from these cell cultures made the quantitative evaluation of the cell viability determination method possible.

I want to extend my greatest appreciation for the support and guidance that I received from my supervisors Firas Mualla and Simon Schöll. They were patient when I was unsure, they were calm when I panicked and they were always willing to listen even at the most unreasonable of times. Thanks guys for a memorable journey.

I would like to thank the Erasmus Mundus COSSE consortium for giving me the opportunity to pursue my post-graduate studies in Europe and for supporting me financially. Without their generous support I would not have been able to partake in this amazing programme.

Last by certainly not least, I would like to thank my parents for their enduring love and continuing support. Mom and dad thank you for encouraging me to follow my dreams and for inspiring me to be a better person.

Appendix A

Patent Documents

The patents pertaining to viable cell counting are summarised in Table A.1 and the original patent documents are attached below.

	Publication number	Publication date	Inventors
1	US 7,958,063 B2	7 June 2011	Xi Long W. Louis Cleveland Y. Lawrence Yao
2	US 7,582,415 B2	1 September 2009	Don Straus
3	JPS5978681 (A)	7 May 1984	Kawahara Haruyuki Imai Kouichi

Table A.1: Summary of patents pertaining to the topic of viable cell counting in cultivation.

(12) **United States Patent**
Long et al.

(10) **Patent No.: US 7,958,063 B2**
(45) **Date of Patent: Jun. 7, 2011**

(54) **METHODS AND SYSTEMS FOR IDENTIFYING AND LOCALIZING OBJECTS BASED ON FEATURES OF THE OBJECTS THAT ARE MAPPED TO A VECTOR**

(75) Inventors: **Xi Long**, Seattle, WA (US); **W. Louis Cleveland**, New York, NY (US); **Y. Lawrence Yao**, New York, NY (US)

(73) Assignee: **Trustees of Columbia University in the City of New York**, New York, NY (US)

(*) Notice: Subject to any disclaimer, the term of this patent is extended or adjusted under 35 U.S.C. 154(b) by 796 days.

(21) Appl. No.: **11/789,571**

(22) Filed: **Apr. 25, 2007**

(65) **Prior Publication Data**

US 2008/0082468 A1 Apr. 3, 2008

Related U.S. Application Data

(63) Continuation of application No. PCT/US2005/040905, filed on Nov. 10, 2005.

(60) Provisional application No. 60/795,210, filed on Apr. 25, 2006, provisional application No. 60/627,465, filed on Nov. 11, 2004.

(51) **Int. Cl.**
G06N 5/00 (2006.01)

(52) **U.S. Cl.** **706/12**; 706/45

(58) **Field of Classification Search** 706/12, 706/45

See application file for complete search history.

(56) **References Cited**

U.S. PATENT DOCUMENTS

4,349,435	A	9/1982	Ochiai
4,421,716	A	12/1983	Hench et al.
6,253,607	B1	7/2001	Dau
2002/0165837	A1	11/2002	Zhang et al.

FOREIGN PATENT DOCUMENTS

WO	WO-99/08091	A1	2/1999

OTHER PUBLICATIONS

Long, et al, Effective Automatic Recognition of Cultured Cells in Bright Field Images Using Fisher's Linear Discriminant Preprocessing, Image and Vision Computing 23 (2005), pp. 1203-1213.*

(Continued)

Primary Examiner — Wilbert L Starks, Jr.

(74) *Attorney, Agent, or Firm* Wilmer Cutler Pickering Hale and Dorr LLP

(57) **ABSTRACT**

A method of identifying and localizing objects belonging to one of three or more classes, includes deriving vectors, each being mapped to one of the objects, where each of the vectors is an element of an N-dimensional space. The method includes training an ensemble of binary classifiers with a CISS technique, using an ECOC technique. For each object corresponding to a class, the method includes calculating a probability that the associated vector belongs to a particular class, using an ECOC probability estimation technique. In another embodiment, increased detection accuracy is achieved by using images obtained with different contrast methods. A nonlinear dimensional reduction technique, Kernel PCA, was employed to extract features from the multi-contrast composite image. The Kernel PCA preprocessing shows improvements over traditional linear PCA preprocessing possibly due to its ability to capture high-order, nonlinear correlations in the high dimensional image space.

40 Claims, 37 Drawing Sheets

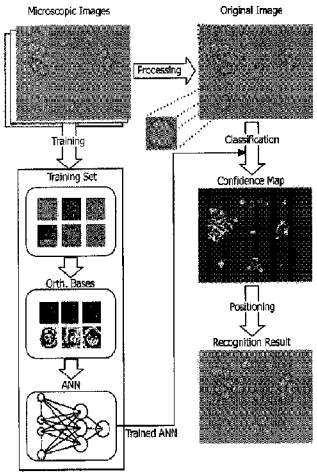

(12) **United States Patent**
Straus

(10) **Patent No.: US 7,582,415 B2**
(45) **Date of Patent: Sep. 1, 2009**

(54) **RAPID DETECTION OF REPLICATING CELLS**

(76) Inventor: **Don Straus**, 19 Buckingham St., Cambridge, MA (US) 02138

(*) Notice: Subject to any disclaimer, the term of this patent is extended or adjusted under 35 U.S.C. 154(b) by 410 days.

(21) Appl. No.: **10/236,107**

(22) Filed: **Sep. 6, 2002**

(65) **Prior Publication Data**

US 2003/0082516 A1 May 1, 2003

Related U.S. Application Data

(60) Provisional application No. 60/317,658, filed on Sep. 6, 2001.

(51) **Int. Cl.**

C12Q 1/00	(2006.01)
C12Q 1/04	(2006.01)
C12M 1/34	(2006.01)
G01N 33/53	(2006.01)
G01N 33/567	(2006.01)
G01N 33/554	(2006.01)
G01N 33/569	(2006.01)

(52) **U.S. Cl.** **435/4**; 435/34; 435/7.2; 435/7.22; 435/7.31; 435/7.32; 435/7.33; 435/7.34; 435/7.35; 435/7.37; 435/36; 435/37; 435/38; 435/39; 435/287.1

(58) **Field of Classification Search** 422/55, 422/82.11; 435/6, 7.2, 7.32, 7.72, 34, 808, 435/810, 4, 7.22, 7.31, 7.33, 7.34, 7.35, 7.37, 435/36, 37, 38, 39, 287.1

See application file for complete search history.

(56) **References Cited**

U.S. PATENT DOCUMENTS

3,694,317	A *	9/1972	Scher	435/39
4,587,213	A *	5/1986	Malecki	435/39
4,959,301	A *	9/1990	Weaver et al.	435/5
5,190,666	A	3/1993	Bisconte	
5,292,644	A	3/1994	Berg	
5,306,420	A	4/1994	Bisconte	
5,321,545	A	6/1994	Bisconte	
5,366,867	A	11/1994	Kawakami et al.	
5,474,910	A	12/1995	Alfano	
5,510,246	A	4/1996	Morgan	
5,552,272	A *	9/1996	Bogart	435/6
5,604,351	A	2/1997	Bisconte	
5,663,057	A	9/1997	Drocourt et al.	
5,792,617	A *	8/1998	Rotman	435/7.23
5,821,066	A *	10/1998	Pyle et al.	435/7.2
5,828,716	A	10/1998	Bisconte de Saint Julien	
5,861,270	A	1/1999	Nelis	
5,968,766	A	10/1999	Powers	
5,976,892	A	11/1999	Bisconte	
5,981,180	A	11/1999	Chandler et al.	
6,122,396	A	9/2000	King et al.	
6,268,222	B1	7/2001	Chandler et al.	
6,472,166	B1	10/2002	Wardlaw et al.	
6,664,528	B1	12/2003	Cartlidge et al.	
6,710,879	B1	3/2004	Hansen et al.	
6,919,960	B2	7/2005	Hansen et al.	
7,068,365	B2	6/2006	Hansen et al.	
2003/0143580	A1	7/2003	Straus	
2003/0170613	A1	9/2003	Straus	
2004/0246483	A1	12/2004	Hansen et al.	
2005/0148085	A1	7/2005	Larsen	
2005/0225766	A1	10/2005	Hansen et al.	
2006/0256340	A1	11/2006	Hansen et al.	

FOREIGN PATENT DOCUMENTS

JP	H11-346795	12/1999
WO	WO 99/58948	11/1999

OTHER PUBLICATIONS

Anonymous, The Brain, Enchanted Learning.com, http://www.enchantedlearning.com/subjects/anatomy/brain, neuron.shtml, Copyright 2001-2007, Printed Nov. 4, 2007. pp. 1-4.*

Wolniak, S.M. 2004. BSCI 427 Principles of Microscopy Fall 2004 Syllabus. 8 Pages http://www.life.umd.edu/cbmg/faculty/wolniak/wolniac/micro.html. Printed Nov. 8, 2007.*

Colony Counter (http://www.topac.com/acolyte.html).

Colony Counter Models and Specifications (http://www.biologics-inc.com/cc-models.htm).

Corkidi et al., "COVASIAM: An Image Analysis Method That Allows Detection of Confluent Microbial Colonies and Colonies of Various Sizes for Automated Counting," *Appl. Environ. Microbiol.* 64:1400-1404 (1998).

Digital Multi-Purpose High-Resolution Colony and Plaque Counter (http://www.loats.com/mla.html)

Esteban et al., "Improved Direct Epifluorescent Filter Technique for Rapid Bioburden Control in Intravenous Solutions," *J. Parenter. Sci. Technol.* 46:146-149 (1992).

Loats et al., "I.AI High-Resolution Automated Colony Counting System Mouse Lymphoma Assay: Performance Analysis," (http://www.loats.com/docs/IIRCCval/IIRCCval.htm).

System Specifications (http//www.loats.com/order_info.html) (1999).

Wilson, "Use of the IUL Countermat Automatic Colony Counter for Spiral Plated Total Viable Counts," *Appl. Environ. Microbiol.* 61:3158-3160 (1995).

Yasui et al., "Imaging of *Lactobacillus brevis* Single Cells and Microcolonies without a Microscope by an Ultrasensitive Chemiluminescent Enzyme Immunoassay with a Photon-Counting Television Camera," *Appl. Environ. Microbiol.* 63:4528-4533 (1997).

* cited by examiner

Primary Examiner—Jon Weber
Assistant Examiner—Kailash C Srivastava
(74) *Attorney, Agent, or Firm* Clark & Elbing LLP

(57) **ABSTRACT**

The invention enables efficient, rapid, and sensitive enumeration of living cells by detecting microscopic colonies derived from in situ cell division using large area imaging. Microbial enumeration tests based on the invention address an important problem in clinical and industrial microbiology the long time needed for detection in traditional tests—while retaining key advantages of the traditional methods based on microbial culture. Embodiments of the invention include non-destructive aseptic methods for detecting cellular microcolonies without labeling reagents. These methods allow for the generation of pure cultures which can be used for microbial identification and determination of antimicrobial resistance.

99 Claims, 22 Drawing Sheets

Bibliographic data: JPS5978681 (A) — 1984-05-07

AUTOMATIC CALCULATOR OF VIABLE CELL COUNT IN CULTIVATION

Page bookmark	JPS5978681 (A) - AUTOMATIC CALCULATOR OF VIABLE CELL COUNT IN CULTIVATION
Inventor(s):	KAWAHARA HARUYUKI; IMAI KOUICHI +
Applicant(s):	KAWAHARA HARUYUKI +
Classification:	- **international:** ***C12M1/34;*** (IPC1-7): C12M1/34
	- **cooperative:**
Application number:	JP19820188340 19821026
Priority number(s):	JP19820188340 19821026
Also published as:	→JPS629311 (B2)

Abstract of JPS5978681 (A)

PURPOSE:To simplify an experiment system and to calculate quickly a viable cell count, by taking a photograph of viable cell specimen through a inverted phase contrast microscope by a TV camera, scanning the image signal, calculating a viable cell count by an image analyzer, treating the information.
CONSTITUTION:The viable cell specimen 1 of cultivation is prepared, the photograph of it is taken by the inverted phase contrast microscope 2, the image of the viable specimen is magnified by 4 times by the TV camera 3, the photograph of it is taken, the cell is read and the cell count is calculated while the image signal is scanned by the image analyzer 4.; The analyzed signal is inputted through the AD converter 5 to the computer 6, treated, shown by CRT, subjected to quantity conversion, displayed by a graph, the image data of the viable cell are stored in the memory means 9, the data and various kinds of analyzed date are culculated to effect many displays. The image of the viable cell is with a magnifaction of X120 shown by the TV moniters 7 and 8, respectively. Consequently, simplification of expeiment system, speediness of calculation, elimination of factitious error, needlessness of specific skill, etc. are achieved.

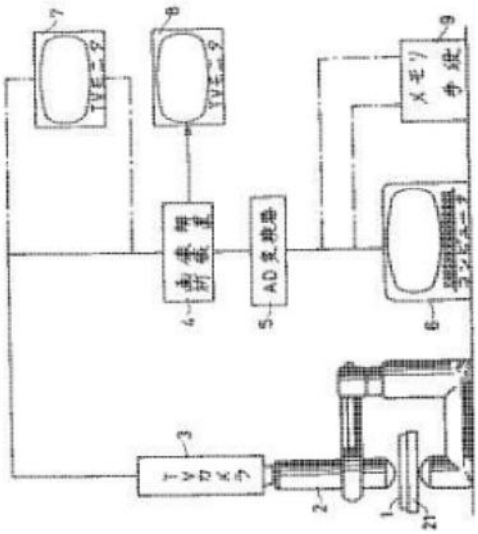

Appendix B

Viability results

B.1 Viability determination in bright-field micrographs

B.1.1 Dynamic patch size

Non-viable versus viable-suspension

Classifier	SIFT	Ray	Stencil	Vmap	Val and Score
SVM: Linear	$83,06 \pm 1,32$	$77,45 \pm 3,32$	$83,91 \pm 1,61$	$85,95 \pm 1,95$	$76,97 \pm 1,40$
SVM: RBF	$81,94 \pm 1,87$	$77,89 \pm 2,13$	$88,28 \pm 1,34$	$86,41 \pm 1,24$	$80,99 \pm 1,34$
RF	$83,25 \pm 1,98$	$78,17 \pm 5,28$	$88,26 \pm 0,93$	$83,69 \pm 2,21$	$77,14 \pm 2,80$
Tree	$75,90 \pm 2,48$	$70,98 \pm 3,13$	$82,52 \pm 1,65$	$80,38 \pm 4,08$	$75,58 \pm 4,67$
Classifier	GTex16	GTex32	GTex64	GTex128	GTex256
SVM: Linear	$73,88 \pm 2,32$	$76,64 \pm 1,60$	$77,67 \pm 1,72$	$77,09 \pm 1,87$	$75,49 \pm 4,45$
SVM: RBF	$75,01 \pm 1,60$	$76,20 \pm 1,90$	$76,60 \pm 1,80$	$74,66 \pm 1,89$	$71,86 \pm 1,04$
RF	$71,80 \pm 1,60$	$74,84 \pm 2,00$	$76,12 \pm 1,97$	$76,38 \pm 1,94$	$77,33 \pm 1,98$
Tree	$68,09 \pm 2,03$	$70,71 \pm 2,4$	$71,59 \pm 2,24$	$71,52 \pm 2,85$	$73,44 \pm 2,26$
Classifier	CTex16	CTex32	CTex64	CTex128	CTex256
SVM: Linear	$80,50 \pm 2,07$	$84,85 \pm 1,74$	$84,75 \pm 1,46$	$82,99 \pm 2,90$	$75,68 \pm 10,42$
SVM: RBF	$81,73 \pm 2,34$	$82,05 \pm 1,99$	$79,69 \pm 1,53$	$66,63 \pm 5,91$	$51,50 \pm 2,83$
RF	$80,36 \pm 2,93$	$83,63 \pm 2,55$	$84,52 \pm 2,59$	$84,43 \pm 2,94$	$84,44 \pm 2,95$
Tree	$73,83 \pm 3,34$	$76,75 \pm 2,82$	$80,05 \pm 2,61$	$78,77 \pm 2,63$	$78,63 \pm 3,52$

Non-viable versus viable-adherent

Classifier	SIFT	Ray	Stencil	Vmap	Value and Score
SVM: Linear	$63,98 \pm 1,25$	$53,73 \pm 0,75$	$53,90 \pm 1,93$	$49,12 \pm 2,57$	$51,4 \pm 3,73$
SVM: RBF	$65,08 \pm 1,46$	$53,36 \pm 1,05$	$54,41 \pm 2,52$	$50,01 \pm 1,04$	$49,78 \pm 4,51$
RF	$66,45 \pm 1,66$	$57,82 \pm 1,37$	$61,55 \pm 1,23$	$55,01 \pm 2,1$	$51,91 \pm 3,13$
Tree	$59,58 \pm 1,20$	$53,66 \pm 1,65$	$55,13 \pm 1,43$	$53,78 \pm 2,23$	$51,09 \pm 3,73$
Classifier	GTex16	GTex32	GTex64	GTex128	GTex256
SVM: Linear	$52,39 \pm 2,89$	$53,66 \pm 2,63$	$55,32 \pm 2,08$	$54,55 \pm 3,02$	$55,75 \pm 3,18$
SVM: RBF	$53,36 \pm 2,42$	$54,39 \pm 1,46$	$56,34 \pm 2,35$	$55,71 \pm 1,75$	$54,51 \pm 1,88$
RF	$53,53 \pm 1,87$	$55,03 \pm 1,43$	$55,8 \pm 2,31$	$56,04 \pm 2,32$	$56,24 \pm 1,86$
Tree	$52,69 \pm 1,47$	$53,84 \pm 1,06$	$53,78 \pm 1,30$	$54,35 \pm 1,75$	$54,3 \pm 1,14$
Classifier	CTex16	CTex32	CTex64	CTex128	CTex256
SVM: Linear	$63,74 \pm 3,09$	$66,14 \pm 2,74$	$65,91 \pm 5,68$	$67,68 \pm 2,37$	$59,86 \pm 8,58$
SVM: RBF	$65,31 \pm 3,37$	$65,37 \pm 2,80$	$63,21 \pm 2,93$	$60,24 \pm 2,14$	$54,9 \pm 5,50$
RF	$64,37 \pm 2,96$	$64,64 \pm 3,76$	$65,23 \pm 4,14$	$64,2 \pm 3,98$	$64,23 \pm 3,9$
Tree	$59,26 \pm 2,21$	$58,98 \pm 2,32$	$60,08 \pm 3,39$	$59,39 \pm 3,24$	$58,6 \pm 3,13$

B.1.2 Static patch size

Non-viable versus viable-suspension

Classifier	GTex16	GTex32	GTex64	GTex128	GTex256
SVM: Linear	$64,27 \pm 4,20$	$65,61 \pm 4,35$	$66,14 \pm 4,54$	$65,12 \pm 4,78$	$66,01 \pm 3,01$
SVM: RBF	$63,82 \pm 5,93$	$65,54 \pm 3,78$	$65,22 \pm 4,48$	$64,01 \pm 4,26$	$62,78 \pm 2,54$
RF	$62,49 \pm 4,49$	$64,79 \pm 3,59$	$65,28 \pm 3,95$	$65,2 \pm 4,34$	$71,13 \pm 7,52$
Tree	$60,12 \pm 3,59$	$61,53 \pm 2,88$	$62,38 \pm 3,48$	$61,76 \pm 4,40$	$61,6 \pm 3,80$
Classifier	CTex16	CTex32	CTex64	CTex128	CTex256
SVM: Linear	$79,14 \pm 2,05$	$82,14 \pm 2,32$	$82,01 \pm 1,83$	$80,2 \pm 4,31$	$74,24 \pm 6,88$
SVM: RBF	$80,78 \pm 2,15$	$80,2 \pm 3,01$	$76,93 \pm 2,43$	$65,77 \pm 5,35$	$51,13 \pm 2,5$
RF	$79,5 \pm 2,71$	$81,8 \pm 3,23$	$82,37 \pm 3,06$	$82,22 \pm 3,54$	$82,36 \pm 3,15$
Tree	$72,51 \pm 4,23$	$76,39 \pm 2,62$	$78,09 \pm 2,14$	$75,5 \pm 4,76$	$77,05 \pm 3,22$
Classifier	Patch				
SVM: Linear	$82,86 \pm 3,20$				
SVM: RBF	$84,86 \pm 5,97$				
RF	$81,03 \pm 9,16$				
Tree	$75,46 \pm 7,00$				

Non-viable versus viable-adherent

Classifier	GTex16	GTex32	GTex64	GTex128	GTex256
SVM: Linear	51, 64±3, 03	52, 54±2, 58	53, 32±1, 6	53, 49±1, 92	53, 67±2, 74
SVM: RBF	51, 61±2, 52	52, 64±1, 9	54, 07±2, 12	53, 64±1, 77	53, 21±1, 63
RF	53, 28±1, 26	53, 77±0, 73	55, 27±1, 52	54, 55±1, 15	54, 60±1, 43
Tree	52, 37±1, 32	53, 32±0, 57	53, 78±1, 64	54, 00±1, 13	53, 61±1, 23
Classifier	CTex16	CTex32	CTex64	CTex128	CTex256
SVM: Linear	65, 13±3, 65	66, 62±4, 36	63, 06±5, 87	63, 93±8, 25	63, 39±10, 25
SVM: RBF	67, 94±2, 44	66, 98±3, 97	64, 56±3, 04	60, 68±2, 25	54, 85±5, 62
RF	65, 59±3, 42	65, 32±3, 97	66, 9±3, 89	66, 44±3, 64	66, 11±3, 84
Tree	60, 18±2, 30	60, 84±2, 7	60, 86±1, 90	61, 54±1, 40	60, 78±2, 48
Classifier	Patch				
SVM: Linear	63, 29±9, 20				
SVM: RBF	62, 22±8, 10				
RF	60, 55±5, 71				
Tree	55, 14±2, 83				

B.2 Viability determination in phase contrast micrographs

B.2.1 Dynamic patch size

Non-viable versus viable-suspension

Classifier	SIFT	Ray	Stencil	Vmap	Value and Score
SVM: Linear	74, 71±1, 23	64, 34±3, 11	69, 62±3, 84	68, 68±1, 97	55, 49±6, 91
SVM: RBF	75, 28±1, 48	61, 81±2, 58	76, 26±1, 13	68, 04±1, 35	68, 76±2, 05
RF	77, 16±0, 88	69, 99±1, 55	75, 93±1, 45	64, 84±1, 97	60, 28±3, 84
Tree	70, 74±1, 66	61, 77±1, 76	68, 48±1, 77	61, 04±1, 64	58, 74±1, 67
Classifier	GTex16	GTex32	GTex64	GTex128	GTex256
SVM: Linear	68, 74±1, 72	69, 27±2, 42	69, 00±2, 49	67, 66±2, 51	63, 43±9, 26
SVM: RBF	70, 5±1, 68	70, 58±2, 28	69, 75±2, 23	67, 51±2, 47	65, 52±2, 57
RF	67, 44±3, 03	69, 77±2, 53	70, 05±2, 39	70, 36±2, 46	70, 44±2, 51
Tree	64, 34±2, 65	65, 97±2, 30	65, 87±2, 23	66, 38±2, 09	66, 64±1, 99
Classifier	CTex16	CTex32	CTex64	CTex128	CTex256
SVM: Linear	82, 21±0, 90	84, 88±0, 96	83, 54±3, 11	72, 42±9, 04	69, 59±10, 15
SVM: RBF	83, 14±1, 14	82, 87±1, 84	77, 09±3, 71	58, 63±5, 06	57, 34±9, 16
RF	83, 04±1, 83	85, 16±1, 93	85, 53±1, 84	85, 77±1, 86	85, 73±1, 87
Tree	76, 95±2, 04	79, 27±1, 81	79, 06±1, 36	79, 54±1, 71	79, 42±1, 15

Non-viable versus viable-adherent

Classifier	SIFT	Ray	Stencil	Vmap	Value and Score
SVM: Linear	64, 79±1, 20	53, 28±2, 35	61, 29±2, 42	63, 77±4, 53	55, 09±2, 53
SVM: RBF	65, 31±1, 87	53, 87±1, 58	64, 53±3, 51	61, 41±7, 57	58, 78±5, 66
RF	70, 33±1, 29	65, 05±2, 10	70, 06±2, 57	61, 27±2, 89	59, 09±2, 71
Tree	62, 98±1, 31	56, 60±2, 49	60, 91±1, 58	58, 07±1, 72	57, 96±3, 47
Classifier	GTex16	GTex32	GTex64	GTex128	GTex256
SVM: Linear	53, 96±3, 36	53, 76±4, 65	53, 9±4, 74	53, 44±4, 58	53, 33±5, 83
SVM: RBF	56, 43±7, 62	58, 47±5, 01	58, 24±4, 65	55, 80±3, 6	53, 87±2, 06
RF	60, 48±3, 3	62, 27±3, 05	63, 05±2, 39	63, 5±2, 22	63, 77±2, 46
Tree	57, 32±2, 76	57, 55±2, 57	58, 10±2, 31	58, 33±2, 24	58, 52±2, 31
Classifier	CTex16	CTex32	CTex64	CTex128	CTex256
SVM: Linear	55, 76±4, 48	56, 92±3, 93	51, 39±7, 36	52, 73±7, 58	49, 73±9, 98
SVM: RBF	57, 79±4, 30	59, 13±2, 78	59, 42±2, 3	64, 7±1, 07	66, 23±1, 30
RF	64, 62±3, 17	65, 66±2, 49	65, 80±2, 49	66, 18±2, 38	66, 28±2, 29
Tree	58, 21±3, 07	58, 39±2, 04	59, 33±1, 78	59, 50±1, 96	59, 40±1, 94

B.2.2 Static patch size

Non-viable versus viable-suspension

Classifier	GTex16	GTex32	GTex64	GTex128	GTex256
SVM: Linear	62, 74±1, 39	63, 04±2, 05	62, 99±2, 85	62, 85±3, 66	63, 63±3, 70
SVM: RBF	63, 00±2, 38	63, 45±2, 44	62, 92±2, 48	61, 14±1, 99	59, 49±1, 67
RF	62, 54±1, 87	63, 48±2, 38	63, 18±2, 08	63, 29±1, 81	61, 37±2, 57
Tree	59, 32±1, 39	60, 05±1, 84	60, 18±1, 65	58, 43±2, 09	58, 33±2, 40
Classifier	CTex16	CTex32	CTex64	CTex128	CTex256
SVM: Linear	84, 69±1, 32	86, 48±1, 47	84, 97±4, 85	78, 29±6, 82	66, 37±15, 21
SVM: RBF	85, 02±1, 69	83, 73±2, 11	76, 13±5, 44	58, 27±5, 49	57, 34±9, 17
RF	84, 54±1, 56	86, 37±1, 58	86, 23±1, 71	86, 04±1, 15	85, 57±1, 68
Tree	77, 31±1, 49	79, 42±2, 43	79, 59±1, 65	76, 57±0, 8	76, 28±2, 34
Classifier	Patch				
SVM: Linear	81, 65±4, 55				
SVM: RBF	84, 37±3, 86				
RF	86, 23±2, 34				
Tree	77, 6±3, 07				

Non-viable versus viable-adherent

Classifier	GTex16	GTex32	GTex64	GTex128	GTex256
SVM: Linear	$52,86\pm5,57$	$51,71\pm4,97$	$50,45\pm7,94$	$50,55\pm6,55$	$54,11\pm5,46$
SVM: RBF	$52,64\pm6,35$	$52,33\pm3,35$	$54,19\pm4,38$	$53,89\pm3,13$	$52,55\pm1,74$
RF	$60,72\pm2,83$	$61,35\pm2,67$	$60,81\pm3,78$	$60,64\pm3,21$	$60,16\pm2,92$
Tree	$57,04\pm2,21$	$56,61\pm2,00$	$56,86\pm2,63$	$56,66\pm2,17$	$55,89\pm2$
Classifier	CTex16	CTex32	CTex64	CTex128	CTex256
SVM: Linear	$56,77\pm4,67$	$58,32\pm4,22$	$56,58\pm5,9$	$54,19\pm7,8$	$51,65\pm8,79$
SVM: RBF	$58,56\pm4,41$	$58,75\pm3,31$	$59,90\pm2,42$	$65,13\pm0,97$	$66,22\pm1,28$
RF	$65,05\pm2,46$	$65,75\pm1,77$	$65,67\pm1,94$	$64,08\pm2,18$	$64,31\pm1,33$
Tree	$57,90\pm1,79$	$59,15\pm1,72$	$58,13\pm2,72$	$57,72\pm3,15$	$58,03\pm2,10$
Classifier	Patch				
SVM: Linear	$50,49\pm7,34$				
SVM: RBF	$55,13\pm7,47$				
RF	$63,46\pm3,54$				
Tree	$57,20\pm2,14$				

B.3 Viability determination in negatively-defocused bright-field micrographs

B.3.1 Dynamic patch size

Non-viable versus viable-suspension

Classifier	SIFT	Ray	Stencil	Vmap	Value and Score
SVM: Linear	$81,90\pm0,83$	$75,23\pm4,89$	$84,63\pm1,02$	$85,31\pm1,95$	$77,82\pm1,62$
SVM: RBF	$81,85\pm1,36$	$69,97\pm3,16$	$88,40\pm0,65$	$85,65\pm1,46$	$79,98\pm0,60$
RF	$83,98\pm1,56$	$77,01\pm3,27$	$88,18\pm1,14$	$83,34\pm2,25$	$74,72\pm3,53$
Tree	$76,05\pm0,98$	$68,32\pm3,21$	$81,83\pm1,41$	$79,35\pm2,23$	$72,66\pm3,97$
Classifier	GTex16	GTex32	GTex64	GTex128	GTex256
SVM: Linear	$80,78\pm1,13$	$82,88\pm0,8$	$83,56\pm0,96$	$82,81\pm1,27$	$80,77\pm1,90$
SVM: RBF	$80,70\pm1,22$	$82,42\pm1,17$	$82,43\pm1,13$	$80,00\pm1,23$	$76,19\pm0,82$
RF	$78,35\pm0,80$	$80,88\pm1,09$	$81,12\pm1,13$	$81,69\pm0,83$	$82,41\pm0,85$
Tree	$73,91\pm1,58$	$75,85\pm1,34$	$76,89\pm0,86$	$77,48\pm1,50$	$78,93\pm1,31$
Classifier	CTex16	CTex32	CTex64	CTex128	CTex256
SVM: Linear	$81,52\pm0,85$	$85,09\pm0,80$	$85,37\pm0,48$	$77,51\pm7,41$	$79,79\pm3,11$
SVM: RBF	$82,94\pm0,83$	$82,8\pm0,89$	$78,83\pm1,40$	$62,32\pm4,55$	$53,47\pm2,99$
RF	$82,48\pm1,14$	$84,75\pm1,2$	$85,17\pm1,01$	$85,24\pm0,99$	$85,41\pm0,86$
Tree	$75,06\pm2,14$	$79,08\pm2,36$	$79,88\pm1,63$	$79,96\pm1,31$	$80,09\pm1,39$

Non-viable versus viable-adherent

Classifier	SIFT	Ray	Stencil	Vmap	Value and Score
SVM: Linear	$64,96 \pm 2,41$	$55,12 \pm 1,53$	$58,88 \pm 2,32$	$49,00 \pm 4,13$	$51,09 \pm 5,36$
SVM: RBF	$65,34 \pm 2,32$	$54,82 \pm 1,44$	$59,66 \pm 3,75$	$47,72 \pm 4,35$	$47,97 \pm 4,52$
RF	$69,90 \pm 1,07$	$63,09 \pm 3,38$	$65,2 \pm 1,65$	$56,2 \pm 1,28$	$54,77 \pm 3,92$
Tree	$61,80 \pm 1,04$	$55,64 \pm 2,52$	$58,09 \pm 2,20$	$53,7 \pm 1,48$	$53,64 \pm 2,25$
Classifier	GTex16	GTex32	GTex64	GTex128	GTex256
SVM: Linear	$56,72 \pm 3,49$	$60,24 \pm 1,36$	$60,85 \pm 1,24$	$62,21 \pm 1,54$	$60,63 \pm 3,80$
SVM: RBF	$58,10 \pm 2,65$	$61,38 \pm 2,08$	$60,93 \pm 3,66$	$58,27 \pm 1,31$	$56,49 \pm 1,61$
RF	$58,46 \pm 1,44$	$60,12 \pm 1,07$	$61,25 \pm 1,47$	$60,94 \pm 1,31$	$61,10 \pm 1,56$
Tree	$55,79 \pm 1,43$	$56,31 \pm 0,92$	$57,47 \pm 1,94$	$56,11 \pm 1,43$	$55,94 \pm 1,75$
Classifier	CTex16	CTex32	CTex64	CTex128	CTex256
SVM: Linear	$60,41 \pm 3,06$	$62,94 \pm 3,21$	$63,15 \pm 4,58$	$59,09 \pm 6,17$	$50,73 \pm 5,59$
SVM: RBF	$63,29 \pm 3,68$	$64,79 \pm 2,97$	$61,16 \pm 2,08$	$61,97 \pm 1,11$	$61,60 \pm 0,67$
RF	$64,13 \pm 2,94$	$66,62 \pm 1,92$	$66,48 \pm 2,46$	$66,09 \pm 2,33$	$66,11 \pm 2,08$
Tree	$58,11 \pm 2,70$	$58,93 \pm 1,53$	$59,32 \pm 2,58$	$59,1 \pm 2,53$	$59,96 \pm 2,81$

B.3.2 Static patch size

Non-viable versus viable-suspension

Classifier	GTex16	GTex32	GTex64	GTex128	GTex256
SVM: Linear	$60,81 \pm 1,67$	$62,42 \pm 2,52$	$62,45 \pm 3,22$	$60,93 \pm 4,14$	$58,35 \pm 6,74$
SVM: RBF	$61,51 \pm 1,52$	$63,85 \pm 1,40$	$63,83 \pm 1,37$	$61,98 \pm 1,77$	$60,17 \pm 1,59$
RF	$62,42 \pm 0,63$	$64,42 \pm 0,83$	$64,36 \pm 1,10$	$64,45 \pm 1,11$	$63,87 \pm 1,44$
Tree	$59,78 \pm 0,91$	$61,18 \pm 1,38$	$60,82 \pm 2,06$	$60,7 \pm 1,8$	$60,93 \pm 2,01$
Classifier	CTex16	CTex32	CTex64	CTex128	CTex256
SVM: Linear	$77,55 \pm 1,69$	$79,76 \pm 2,42$	$79,78 \pm 2,38$	$75,84 \pm 4,71$	$64,42 \pm 9,53$
SVM: RBF	$78,78 \pm 1,57$	$78,96 \pm 2,92$	$77,21 \pm 2,73$	$61,72 \pm 4,21$	$53,44 \pm 3,15$
RF	$78,79 \pm 1,20$	$79,98 \pm 3,87$	$80,72 \pm 3,72$	$80,10 \pm 4,30$	$79,78 \pm 5,12$
Tree	$72,40 \pm 3,56$	$74,24 \pm 4,97$	$74,24 \pm 4,47$	$75,31 \pm 1,80$	$73,07 \pm 5,02$
Classifier	Patch				
SVM: Linear	$75,60 \pm 3,60$				
SVM: RBF	$84,03 \pm 3,02$				
RF	$80,86 \pm 6,37$				
Tree	$74,24 \pm 5,02$				

Non-viable versus viable-adherent

Classifier	GTex16	GTex32	GTex64	GTex128	GTex256
SVM: Linear	$50,65\pm4,35$	$51,71\pm3,86$	$51,63\pm4,11$	$51,03\pm4,07$	$53,64\pm4,08$
SVM: RBF	$52,18\pm2,89$	$53,96\pm2,58$	$54,47\pm2,37$	$52,32\pm2,27$	$52,46\pm1,58$
RF	$56,37\pm1,19$	$57,33\pm1,47$	$57,57\pm1,03$	$57,09\pm1,07$	$56,62\pm1,21$
Tree	$54,59\pm1,07$	$54,81\pm1,45$	$54,73\pm0,78$	$55,05\pm0,99$	$54,68\pm1,38$
Classifier	CTex16	CTex32	CTex64	CTex128	CTex256
SVM: Linear	$61,60\pm3,54$	$62,26\pm5,22$	$57,38\pm6,34$	$61,31\pm6,12$	$50,61\pm8,21$
SVM: RBF	$64,69\pm2,94$	$65,31\pm2,52$	$62,77\pm2,19$	$63,00\pm0,74$	$61,59\pm0,65$
RF	$65,24\pm2,34$	$66,44\pm2,40$	$67,55\pm1,98$	$67,04\pm2,33$	$66,87\pm2,02$
Tree	$58,93\pm1,30$	$59,75\pm1,85$	$60,24\pm2,79$	$60,65\pm2,28$	$59,81\pm1,67$
Classifier	Patch				
SVM: Linear	$63,39\pm1,96$				
SVM: RBF	$62,71\pm7,06$				
RF	$63,68\pm5,52$				
Tree	$54,80\pm3,61$				

B.4 Viability determination in positively-defocused bright-field micrographs

B.4.1 Dynamic patch size

Non-viable versus viable-suspension

Classifier	SIFT	Ray	Stencil	Vmap	Value and Score
SVM: Linear	$80,59\pm1,65$	$73,52\pm2,24$	$85,37\pm0,94$	$85,46\pm2,49$	$67,74\pm4,43$
SVM: RBF	$81,08\pm1,92$	$74,87\pm0,83$	$88,11\pm0,49$	$85,80\pm2,16$	$75,61\pm0,81$
RF	$82,14\pm1,17$	$75,91\pm2,47$	$87,70\pm2,75$	$85,31\pm1,35$	$74,22\pm2,71$
Tree	$74,53\pm1,71$	$67,83\pm1,81$	$81,50\pm2,40$	$82,13\pm2,23$	$73,22\pm2,75$
Classifier	GTex16	GTex32	GTex64	GTex128	GTex256
SVM: Linear	$70,21\pm1,55$	$71,32\pm1,50$	$71,45\pm2,18$	$69,55\pm1,59$	$70,42\pm2,55$
SVM: RBF	$70,60\pm1,45$	$72,52\pm1,70$	$71,31\pm1,94$	$69,93\pm1,65$	$66,62\pm1,93$
RF	$69,55\pm1,64$	$70,63\pm2,47$	$71,13\pm1,84$	$71,31\pm2,16$	$71,09\pm2,15$
Tree	$65,68\pm2,03$	$66,40\pm2,48$	$67,29\pm2,43$	$67,78\pm1,63$	$68,21\pm1,57$
Classifier	CTex16	CTex32	CTex64	CTex128	CTex256
SVM: Linear	$78,28\pm1,62$	$80,23\pm1,65$	$79,66\pm2,73$	$73,36\pm6,54$	$65,48\pm11,29$
SVM: RBF	$80,76\pm1,61$	$79,26\pm2,49$	$74,77\pm2,80$	$69,34\pm4,27$	$57,55\pm9,12$
RF	$78,17\pm2,49$	$79,19\pm3,04$	$79,77\pm2,58$	$79,63\pm2,97$	$79,65\pm2,72$
Tree	$72,79\pm2,37$	$72,95\pm4,23$	$75,01\pm1,45$	$73,66\pm3,48$	$73,13\pm4,38$

Non-viable versus viable-adherent

Classifier	SIFT	Ray	Stencil	Vmap	Value and Score
SVM: Linear	$61,53 \pm 1,40$	$52,12 \pm 1,06$	$51,71 \pm 1,20$	$51,58 \pm 1,21$	$49,71 \pm 1,66$
SVM: RBF	$62,57 \pm 1,89$	$51,66 \pm 1,22$	$53,57 \pm 0,78$	$50,88 \pm 1,80$	$50,29 \pm 1,85$
RF	$62,26 \pm 1,90$	$57,81 \pm 1,39$	$62,23 \pm 3,13$	$54,43 \pm 1,15$	$54,88 \pm 3,08$
Tree	$57,25 \pm 1,56$	$54,03 \pm 0,94$	$56,20 \pm 2,18$	$53,28 \pm 1,89$	$52,60 \pm 3,21$
Classifier	GTex16	GTex32	GTex64	GTex128	GTex256
SVM: Linear	$53,99 \pm 1,92$	$53,50 \pm 1,46$	$55,49 \pm 1,36$	$57,55 \pm 2,58$	$53,32 \pm 3,70$
SVM: RBF	$54,78 \pm 1,46$	$54,57 \pm 2,24$	$56,71 \pm 1,89$	$54,79 \pm 1,27$	$54,56 \pm 1,11$
RF	$54,63 \pm 1,10$	$54,09 \pm 1,62$	$55,87 \pm 1,11$	$56,25 \pm 0,83$	$56,36 \pm 1,16$
Tree	$53,34 \pm 1,05$	$52,44 \pm 0,79$	$53,03 \pm 0,54$	$53,91 \pm 0,90$	$54,27 \pm 1,50$
Classifier	CTex16	CTex32	CTex64	CTex128	CTex256
SVM: Linear	$63,79 \pm 2,21$	$65,14 \pm 2,00$	$65,73 \pm 3,80$	$63,64 \pm 4,88$	$56,36 \pm 5,44$
SVM: RBF	$65,58 \pm 1,23$	$65,22 \pm 1,98$	$59,20 \pm 3,10$	$54,37 \pm 3,68$	$51,02 \pm 4,40$
RF	$63,30 \pm 2,21$	$64,03 \pm 2,79$	$65,07 \pm 3,25$	$65,21 \pm 2,62$	$64,82 \pm 2,72$
Tree	$58,36 \pm 0,78$	$58,15 \pm 2,52$	$59,31 \pm 1,72$	$59,16 \pm 1,27$	$58,54 \pm 2,03$

B.4.2 Static patch size

Non-viable versus viable-suspension

Classifier	GTex16	GTex32	GTex64	GTex128	GTex256
SVM: Linear	$64,75 \pm 3,95$	$67,51 \pm 2,81$	$67,33 \pm 3,24$	$63,21 \pm 3,25$	$59,61 \pm 5,99$
SVM: RBF	$65,78 \pm 3,19$	$67,84 \pm 2,91$	$66,37 \pm 3,13$	$65,22 \pm 2,66$	$62,16 \pm 2,04$
RF	$65,46 \pm 1,48$	$66,79 \pm 2,12$	$66,58 \pm 1,93$	$65,35 \pm 2,82$	$65,40 \pm 3,27$
Tree	$61,57 \pm 1,25$	$62,02 \pm 2,20$	$62,67 \pm 1,57$	$60,78 \pm 2,36$	$61,63 \pm 1,82$
Classifier	CTex16	CTex32	CTex64	CTex128	CTex256
SVM: Linear	$77,86 \pm 1,72$	$78,66 \pm 3,71$	$75,63 \pm 5,15$	$72,02 \pm 4,57$	$65,66 \pm 8,70$
SVM: RBF	$78,83 \pm 2,60$	$78,33 \pm 2,83$	$74,28 \pm 3,56$	$69,29 \pm 4,24$	$57,57 \pm 9,14$
RF	$77,19 \pm 2,46$	$77,81 \pm 3,11$	$77,48 \pm 3,25$	$75,99 \pm 4,16$	$75,49 \pm 4,34$
Tree	$69,58 \pm 4,48$	$71,23 \pm 4,16$	$71,96 \pm 2,85$	$69,27 \pm 4,08$	$68,77 \pm 4,39$
Classifier	Patch				
SVM: Linear	$73,31 \pm 3,58$				
SVM: RBF	$77,38 \pm 3,55$				
RF	$79,82 \pm 4,74$				
Tree	$71,21 \pm 5,34$				

Non-viable versus viable-adherent

Classifier	GTex16	GTex32	GTex64	GTex128	GTex256
SVM: Linear	$56,43\pm2,40$	$58,75\pm2,18$	$59,46\pm2,60$	$59,59\pm2,29$	$58,62\pm3,76$
SVM: RBF	$57,58\pm1,55$	$59,54\pm1,55$	$59,59\pm1,72$	$57,45\pm2,26$	$55,87\pm1,47$
RF	$55,86\pm1,93$	$57,21\pm2,25$	$57,66\pm2,37$	$57,11\pm3,53$	$57,00\pm3,00$
Tree	$54,71\pm1,45$	$54,88\pm2,43$	$54,63\pm1,85$	$55,32\pm2,3$	$56,14\pm0,83$
Classifier	CTex16	CTex32	CTex64	CTex128	CTex256
SVM: Linear	$65,01\pm2,71$	$68,18\pm1,88$	$67,80\pm2,42$	$65,79\pm4,15$	$62,19\pm5,58$
SVM: RBF	$66,92\pm2,26$	$66,50\pm1,96$	$61,32\pm2,42$	$53,97\pm2,73$	$51,03\pm4,37$
RF	$63,75\pm2,93$	$65,92\pm2,09$	$66,41\pm2,88$	$66,26\pm2,62$	$66,00\pm2,62$
Tree	$57,50\pm2,75$	$58,40\pm2,06$	$59,25\pm1,39$	$58,42\pm1,73$	$57,52\pm2,69$
Classifier	Patch				
SVM: Linear	$63,47\pm4,74$				
SVM: RBF	$66,06\pm1,44$				
RF	$60,54\pm4,77$				
Tree	$55,71\pm2,47$				

List of Figures

List of Tables

Bibliography

[AB02] Lewis J et al Alberts B, Johnson A. *Molecular Biology of the Cell*. New York: Garland Science, 4th edition, 2002.

[Arv04] Vincent Arvis, Christophe Debain, Michel Berducat, and Albert Benassi. Generalization of the cooccurrence matrix for colour images: application to colour texture classification. *Image Analysis and Stereology*, 23(1):63–72, 2004.

[Bak94] C Jacyn Baker and Norton M Mock. An improved method for monitoring cell death in cell suspension and leaf disc assays using evans blue. *Plant Cell, Tissue and Organ Culture*, 39(1):7–12, 1994.

[Bei95] Michael Beil, Theano Irinopoulou, Jany Vassy, and Günter Wolf. A dual approach to structural texture analysis in microscopic cell images. *Computer methods and programs in biomedicine*, 48(3):211–219, 1995.

[Ber07] Michael R. Berthold, Nicolas Cebron, Fabian Dill, Thomas R. Gabriel, Tobias Kötter, Thorsten Meinl, Peter Ohl, Christoph Sieb, Kilian Thiel, and Bernd Wiswedel. KNIME: The Konstanz Information Miner. In *Studies in Classification, Data Analysis, and Knowledge Organization (GfKL 2007)*. Springer, 2007.

[Bla11] Francis G Blankenberg and Joseph F Norfray. Multimodality molecular imaging of apoptosis in oncology. *American Journal of Roentgenology*, 197(2):308–317, 2011.

[Bla12] Francis G Blankenberg and H William Strauss. Recent advances in the molecular imaging of programmed cell death: part i-pathophysiology and radiotracers. *Journal of Nuclear Medicine*, 53(11):1659–1662, 2012.

[Bor05] Ingwer Borg. *Modern multidimensional scaling: Theory and applications*. Springer, 2005.

[Bou12] Anne-Laure Boulesteix, Silke Janitza, Jochen Kruppa, and Inke R König. Overview of random forest methodology and practical guidance with emphasis on computational biology and bioinformatics. *Wiley Interdisciplinary Reviews: Data Mining and Knowledge Discovery*, 2(6):493–507, 2012.

[Bre] L Breiman. F riedman, jh, olshen, ra, & stone, cj (1984). *Classification and regression trees*.

[Bre83] Leo Breiman, Jerome Friedman, Richard Olshen, Charles Stone, D Steinberg, and P Colla. Cart: Classification and regression trees. *Wadsworth: Belmont, CA*, 156, 1983.

[Bre01] Leo Breiman. Random forests. *Machine learning*, 45(1):5–32, 2001.

[Can86] John Canny. A computational approach to edge detection. *Pattern Analysis and Machine Intelligence, IEEE Transactions on*, (6):679–698, 1986.

[Cha11] Chih-Chung Chang and Chih-Jen Lin. LIBSVM: A library for support vector machines. *ACM Transactions on Intelligent Systems and Technology*, 2:27:1–27:27, 2011. Software available at `http://www.csie.ntu.edu.tw/~cjlin/libsvm`.

[Cod01] David M Coder. Assessment of cell viability. *Current protocols in cytometry*, pages 9–2, 2001.

[Con80] Richard W Conners and Charles A Harlow. A theoretical comparison of texture algorithms. *Pattern Analysis and Machine Intelligence, IEEE Transactions on*, (3):204–222, 1980.

[Dud12] Richard O Duda, Peter E Hart, and David G Stork. *Pattern classification*. John Wiley & Sons, 2012.

[DW00] Van De Wouwer, Van Marck, Van Dyck, et al. Wavelets as chromatin texture descriptors for the automated identification of neoplastic nuclei. *Journal of microscopy*, 197(1):25–35, 2000.

[Euk] Eukaryote. `http://en.wikipedia.org/wiki/File:Animal_cell_structure_en.svg`. Accessed: 2013-03-05.

[Fin05] Susan L Fink and Brad T Cookson. Apoptosis, pyroptosis, and necrosis: mechanistic description of dead and dying eukaryotic cells. *Infection and immunity*, 73(4):1907–1916, 2005.

[Fog71] Jørgen Fogh, Nelda B Holmgren, and Peter P Ludovici. A review of cell culture contaminations. *In vitro*, 7(1):26–41, 1971.

[Ful10] Simone Fulda, Adrienne M Gorman, Osamu Hori, and Afshin Samali. Cellular stress responses: cell survival and cell death. *International journal of cell biology*, 2010, 2010.

[Har73] Robert M Haralick, Karthikeyan Shanmugam, and Its' Hak Dinstein. Textural features for image classification. *Systems, Man and Cybernetics, IEEE Transactions on*, (6):610–621, 1973.

[Har79] Robert M Haralick. Statistical and structural approaches to texture. *Proceedings of the IEEE*, 67(5):786–804, 1979.

[Has01] Trevor. Hastie, Robert. Tibshirani, and J Jerome H Friedman. *The elements of statistical learning*, volume 1. Springer New York, 2001.

[HB07] Mryka Hall-Beyer. Glcm texture: a tutorial. `http://www.fp.ucalgary.ca/mhallbey/tutorial.htm`, February 2007. [Online; accessed 20-May-2013].

[Hic95] Cleveland P Hickman, 1935 Roberts, Larry S., and Allan Larson. *Integrated principles of zoology / Cleveland P. Hickman, Jr., Larry S. Roberts, Allan Larson ; original artwork by William C. Ober and Claire Garrison*. Dubuque, Iowa : Wm. C. Brown Publishers, 9th ed., updated version edition, 1995. Includes bibliographical references and index.

[Hsu03] Chih-Wei Hsu, Chih-Chung Chang, Chih-Jen Lin, et al. A practical guide to support vector classification, 2003.

[Hua03] Kai Huang, Meel Velliste, and Robert F. Murphy. Feature reduction for improved recognition of subcellular location patterns in fluorescence microscope images. pages 307–318, 2003.

[Jur10] Elizabeth Jurrus, Antonio RC Paiva, Shigeki Watanabe, James R Anderson, Bryan W Jones, Ross T Whitaker, Erik M Jorgensen, Robert E Marc, and Tolga Tasdizen. Detection of neuron membranes in electron microscopy images using a serial neural network architecture. *Medical Image Analysis*, 14(6):770–783, 2010.

[Kas98] Samuel Kaski. Dimensionality reduction by random mapping: Fast similarity computation for clustering. In *Neural Networks Proceedings, 1998. IEEE World Congress on Computational Intelligence. The 1998 IEEE International Joint Conference on*, volume 1, pages 413–418. IEEE, 1998.

[Ker72] John FR Kerr, Andrew H Wyllie, and Alastair R Currie. Apoptosis: a basic biological phenomenon with wide-ranging implications in tissue kinetics. *British journal of cancer*, 26(4):239, 1972.

[Kru64] Joseph B Kruskal. Nonmetric multidimensional scaling: a numerical method. *Psychometrika*, 29(2):115–129, 1964.

[Lep03] Jeffrey Leppo. Imaging cell injury and death. *Current cardiology reports*, 5(1):40–44, 2003.

[Lev08] Beth Levine and Guido Kroemer. Autophagy in the pathogenesis of disease. *Cell*, 132(1):27–42, 2008.

[Lin98] Tony Lindeberg. Feature detection with automatic scale selection. *International journal of computer vision*, 30(2):79–116, 1998.

[Lon06] Xi Long, Louis Cleveland, and Y Lawrence Yao. Automatic detection of unstained viable cells in bright field images using a support vector machine with an improved training procedure. *Computers in Biology and Medicine*, 36(4):339–362, 2006.

[Lon10] Xi Long, W Louis Cleveland, and Y Lawrence Yao. Multiclass detection of cells in multicontrast composite images. *Computers in biology and medicine*, 40(2):168–178, 2010.

[Low99] David G Lowe. Object recognition from local scale-invariant features. In *Computer vision, 1999. The proceedings of the seventh IEEE international conference on*, volume 2, pages 1150–1157. Ieee, 1999.

[Lup08] G Lupica, NM Allinson, and SW Botchway. Hybrid image processing technique for the robust identification of unstained cells in bright-field microscope images. In *Computational Intelligence for Modelling Control & Automation, 2008 International Conference on*, pages 1053–1058. IEEE, 2008.

[Maj95] Guido Majno and Isabelle Joris. Apoptosis, oncosis, and necrosis: an overview of cell death. *The American journal of pathology*, 146(1):3, 1995.

[Mal03] N Malpica, A Santos, A Tejedor, A Torres, M Castilla, P García-Barreno, and M Desco. Automatic quantification of viability in epithelial cell cultures by texture analysis. *Journal of Microscopy*, 209(1):34–40, 2003.

[MAT10] MATLAB. *version 7.11.0.584 (R2010b)*. The MathWorks Inc., Natick, Massachusetts, 2010.

[May10] Olivia May. Determining cell vitality. `https://www.caymanchem.com/app/template/Article.vm/article/2157`, June 2010. [Online; accessed 20-February-2013].

[Maz11] NM Mazure, MC Brahimi-Horn, J Pouyssegur, et al. Hypoxic mitochondria: accomplices in resistance. *Bull Cancer*, 98:40–46, 2011.

[Mit10] Sushil Mittal, Yefeng Zheng, Bogdan Georgescu, Fernando Vega-Higuera, Shaohua Kevin Zhou, Peter Meer, and Dorin Comaniciu. Fast automatic detection of calcified coronary lesions in 3d cardiac ct images. In *Machine Learning in Medical Imaging*, pages 1–9. Springer, 2010.

[Mor99] Katharina Morik, Peter Brockhausen, and Thorsten Joachims. Combining statistical learning with a knowledge-based approach-a case study in intensive care monitoring. In *ICML*, volume 99, pages 268–277, 1999.

[Mua13] Firas Mualla, Simon Schöll, Björn Sommerfeldt, and Joachim Hornegger. Automatic cell detection in bright-field microscope images using sift, random forests, and hierarchical clustering. *IEEE Transactions on Medical Imaging*, 2013.

[Pal78] Jiwan P Palta, Jacob Levitt, and Eduard J Stadelmann. Plant viability assay. *Cryobiology*, 15(2):249–255, 1978.

[Pro] Prokaryote. `http://hyperphysics.phy-astr.gsu.edu/hbase/biology/prokar.html#c2`. Accessed: 2013-03-05.

[Ros80] Azriel Rosenfeld, Cheng-Ye Wang, and Angela Y d. Multispectral texture. Technical report, DTIC Document, 1980.

[Row00] Sam T Roweis and Lawrence K Saul. Nonlinear dimensionality reduction by locally linear embedding. *Science*, 290(5500):2323–2326, 2000.

[Sha05] Howard M Shapiro. *Practical flow cytometry*. Wiley. com, 2005.

[Smi09] Kevin Smith, Alan Carleton, and Vincent Lepetit. Fast ray features for learning irregular shapes. In *Computer Vision, 2009 IEEE 12th International Conference on*, pages 397–404. IEEE, 2009.

[Tai08] Jonathan F Tait. Imaging of apoptosis. *Journal of Nuclear Medicine*, 49(10):1573–1576, 2008.

[Tec] Life Technologies. Fluorescence spectraviewer. `http://de-de.invitrogen.com/site/de/de/home/Products-and-Services/Applications/Cell-Analysis/Labeling-Chemistry/Fluorescence-SpectraViewer.html`. [Online; accessed 23-June-2013].

[Ten00] Joshua B Tenenbaum, Vin De Silva, and John C Langford. A global geometric framework for nonlinear dimensionality reduction. *Science*, 290(5500):2319–2323, 2000.

[Tsc08] Marko Tscherepanow, Frank Zöllner, Matthias Hillebrand, and Franz Kummert. Automatic segmentation of unstained living cells in bright-field microscope images. In *Advances in Mass Data Analysis of Images and Signals in Medicine, Biotechnology, Chemistry and Food Industry*, pages 158–172. Springer, 2008.

[Vap98] V Vapnik. Statistical learning theory. 1998, 1998.

[Ver00] I Vermes, C Haanen, and C Reutelingsperger. Flow cytometry of apoptotic cell death. *Journal of Immunological Methodse*, 243(1-2):167–190, 2000.

[vO94] WY van Opstal, C Ranger, O Lejeune, P Forgez, H Boudin, JC Bisconte, and W Rostene. Automated image analyzing system for the quantitative study of living cells in culture. *Microscopy research and technique*, 28(5):440–447, 1994.

[Wei07] Ning Wei, Jia You, Karl Friehs, Erwin Flaschel, and Tim Wilhelm Nattkemper. An in situ probe for on-line monitoring of cell density and viability on the basis of dark field

microscopy in conjunction with image processing and supervised machine learning. *Biotechnology and bioengineering*, 97(6):1489–1500, 2007.

[Wei08] Ning Wei, Erwin Flaschel, Karl Friehs, and Tim W Nattkemper. A machine vision system for automated non-invasive assessment of cell viability via dark field microscopy, wavelet feature selection and classification. *BMC bioinformatics*, 9(1):449, 2008.

[Wey98] Barbara Weyn, Gert van de Wouwer, André van Daele, Paul Scheunders, Dirk van Dyck, Eric van Marck, and Willem Jacob. Automated breast tumor diagnosis and grading based on wavelet chromatin texture description. *Cytometry*, 33(1):32–40, 1998.

[Wu95] Kenong Wu, David Gauthier, and Martin D Levine. Live cell image segmentation. *Biomedical Engineering, IEEE Transactions on*, 42(1):1–12, 1995.

[Yog96] K Yogesan, T Jørgensen, F Albregtsen, KJ Tveter, and HE Danielsen. Entropy-based texture analysis of chromatin structure in advanced prostate cancer. *Cytometry*, 24(3):268–276, 1996.